Gas analysis in harsh environments by coherent anti-Stokes Raman scattering

DISSERTATION

zur Erlangung des akademischen Grades
doctor rerum naturalium (Dr. rer. nat.)

vorgelegt dem Rat der Physikalisch-Astronomischen Fakultät
der Friedrich-Schiller-Universität Jena

von M.Sc. Xiaodong Zhao
geboren am 5. Februar 1988 in Hebei, China

Gutachter:

1. Prof. Dr. Stefan Nolte, Friedrich-Schiller-Universität Jena
2. Prof. Dr. Michael Schmitt, Friedrich-Schiller-Universität Jena
3. Prof. Dr. Robert P. Lucht, Purdue University, USA

Tage der Disputation: 10.12.2024

Dedication

To my dear wife, my lovely children and my parents. You mean everything to me.

Contents

Contents ii

List of Figures v

List of Tables vii

1 Introduction 1

2 State of the art 5

2.1 Current state of the art and challenges 5

3 Fundamentals 15

3.1 Fundamentals of molecular physics 15

3.2 Fundamentals of CARS 22

3.3 Nonlinear optical effects 36

3.4 Filamentation physics 38

4 CARS based on a reliable ps-laser system with OPA 49

4.1 Overview 49

4.2 Optical parametric amplifier OPA system 50

4.3 The ps-CARS setup 56
4.4 N_2 and CO_2 thermometry 58
4.5 Conclusion 67

5 CARS based on ps filamentation **69**
5.1 Overview 69
5.2 Experimental setup 69
5.3 Spectral properties during filamentation 72
5.4 CARS signals and concentration determination 78
5.5 Conclusion 86

6 Remote CARS based on fs filamentation **87**
6.1 Overview 87
6.2 Experimental setup 88
6.3 Fs filamentation enabling remote CARS 91
6.4 Conclusion 96

7 Summary and outlook **97**

Bibliography **101**

Zusammenfassung **119**

Erklärung **121**

List of publications and conference contributions **122**

Acknowledgment **124**

List of Figures

2.1 Sketch of resonant CARS process energy diagram. 6

3.1 Potential curves for harmonic and anharmonic oscillators. 19

3.2 Illustration for rotation of diatomic molecules. 20

3.3 CARS approaches for phase matching. 24

3.4 Raman excitation of N_2 for the fundamental and the first hot band transitions with different laser sources. 25

3.5 Sketch of nonresonant FWM process. 26

3.6 Illustration of self-phase modulation. 38

3.7 Illustration of self-focusing of a slice with Gaussian distribution across the transverse plane. 42

3.8 Scheme of the evolution of filamentation propagating in an optical medium. 44

4.1 Scheme of the optical parametric amplifier system. 51

4.2 Spectra before and after the long-pass edge filter. 53

4.3 The collimated OPA output beam profiles. 53

4.4 Autocorrelation measurement of the OPA output and the thin-disk pump laser. 54

4.5 Spectral width of the OPA output at 900 nm and the initial laser spectrum. 55

4.6 Spectral width of the signal output of the OPA over the tuning range . . . 55

4.7 Signal output power of OPA over the entire tuning range from 700 nm to 950 nm. 56

4.8 Sketch of collinear CARS setup. 57

4.9 The Raman spectrum of N_2 fundamental peak at room temperature. . . . 59

4.10 The CARS signal of the first hot band of N_2 at a temperature of 600 °C at a pressure of 5 bar. 60

4.11 The vibrational Raman spectrum of N_2 at various temperatures. 60

4.12 The initial dephasing rate of N_2 at a Raman shift of 2330 cm^{-1} at various temperatures with the best fitting curves. 63

4.13 Experimental and the best-fit time-resolved CARS signals of the first hot band at various temperatures. 64

4.14 Sketch of CARS process for the fundamental and first hot band transitions of CO_2. 65

4.15 CARS signals of CO_2 with a pressure of 3 bar at different temperatures. . 66

5.1 Scheme of the setup to measure the broadened spectra after a focusing lens. 70

5.2 Scheme of the setup to measure the number of filaments with a CCD camera. 71

5.3 Optical layout of filament-based CARS. 72

5.4 Initial spectra of the pump and probe pulses. 73

5.5 Filament-induced spectra with an f = 3 m focusing lens for different pulse energies. 74

5.6 Broadened spectra for f = 4 m focusing lens at different pulse energies. . 75

5.7 Most broadened spectra for f = 2 m, 3 m, 4 m. 75

5.8 Images of single shot filaments on a metal plate at various energies using different focal lengths. 77

5.9 Fluctuation of the broadened spectra at a pulse energy of 60 mJ. 78

5.10 CARS spectrum in air for different pulse energies with an f = 3 m focusing lens. 79

5.11 Simulated CARS spectra and the delay scan of N_2 and O_2 signals. 81

5.12 Simulated peak ratio of N_2 and O_2 CARS signals at different probe delay time. 81

5.13 The experimental average peak ratio of N_2 and O_2. 82

5.14 CARS signal of CH_4 at a pulse energy of 34 mJ. 84

5.15 Dispersion effects from optical windows. 86

6.1 Potential curves of N_2 and N_2^+. 89

6.2 Scheme of generation of CARS signal of CO_2 with lasing emission at $\sim$391 nm as a probe. 90

6.3 Scheme of the experimental setup for remote CARS. 90

6.4 Lasing emission of N_2^+ at different focusing conditions. 91

6.5 CARS signal of N_2 and the lasing emission of N_2^+. 92

6.6 CARS spectrum of N_2, O_2, and CO_2 and lasing emission of N_2^+. 93

6.7 CARS signal of CH_4. 94

List of Tables

3.1 Rotational (B), centrifugal (D) and vibrational ($\tilde{\nu}$) constants for molecules of interest in this thesis. 22

3.2 Raman shifts for the fundamental and first hot band of relevant combustion gases. 23

3.3 Raman tensor invariants for N_2 and O_2. 33

3.4 Molecular parameters for HW factor determination. 34

6.1 Comparison of measured and theoretical data. 95

Chapter 1

Introduction

With the background of climate change and global energy crisis, energy consumption has fundamentally changed our daily life. The main human activity emitting the major greenhouse gas CO_2 is the combustion of fossil fuels. In recent years due to the energy crisis, the use of coal in energy production has increased worldwide. In order to reduce gas emission and make the conversion process efficient in large scale industrial processes e.g. combustion and gasification, a non-intrusive and indispensible method is needed to monitor the local temperature and concentration of various gases. Recent advances in laser technology allow one to accurately and non-intrusively measure temperatures and concentrations in combustion devices.

Coherent anti-Stokes Raman spectroscopy (CARS) has been proven to be robust for in-situ combustion diagnostics [1, 2]. For a specific Raman resonance, the CARS signal is proportional to the square of number density difference between the two levels involved. Therefore, the generated CARS signal spectrum contains the information of population distribution among different ro-vibrational states. Since the population of states follows the temperature dependent Boltzmann distribution, the CARS signal carries an intrinsic temperature dependence as well. This temperature dependence makes CARS a popular technique for monitoring the in-situ concentration and temperature in combustion and flames.

Typically, CARS is used with nanosecond (ns) lasers and requires three beams: pump, Stokes and probe beams with at least two different wavelengths. The nonlinear interaction of ns laser beams generates a non-resonant four-wave-mixing (FWM) signal along with the resonant CARS signal. The interference between the resonant and non-resonant signals complicates the analysis. In addition, by operating in nanosecond regime, the CARS signals are influenced by molecular collision effects, which makes it more difficult to analyze the gas temperature and concentration. Furthermore, the ns-CARS measurements are normally performed at low repetition rates (10 - 20 Hz), which leads to a low temporal resolution for in-situ measurements. Thus, the use of ultrashort pulses in femtosecond or picosecond regime has significant advantages, especially for applications at high pressures and temperatures. The fs-CARS signal is free from distortions from molecular collisions and non-resonant contributions, if the excited Raman level is probed within a few ps [3]. Yet, it also has considerable drawbacks. Most of the fs-CARS studies relied on Ti:sapphire based laser systems. Normally the Ti:sapphire based laser systems provide an initial pulse duration of $\sim$ 100 fs, which undergoes dispersion effects when propagating through thick optical windows. One approach is to use an additional, external compressor to compensate the required pre-chirp, which complicates the experimental setup [4]. In addition, too short pulses ($\sim$100 - 500 fs) result in poor spectral resolution [5]. Moreover, Ti:sapphire lasers are typically sensitive to ambient conditions.

The aim of this thesis is to investigate different concepts for ultrashort pulse CARS spectroscopy for gas analysis in harsh environments to overcome these drawbacks.

- **CARS based on a reliable ps-laser system with OPA**
- **CARS based on ps-filamentation**
- **Remote CARS based on fs-filamentation**

The first two concepts are based on a stable and reliable thin-disk laser systems providing $\sim$ 1 ps pulses. During propagation with $\sim$ 1 ps pulses, one can ignore the chirp from

optical windows comparing with fs laser pulses. Hybrid fs/ps-CARS [6–8] uses a spectrally narrowed probe pulse (picosecond pulse duration) to provide sufficient spectral resolution. Thus, pulse durations around 1 ps are very promising. Furthermore, thin-disk laser systems can generate more scalable pulse energy up to hundreds of mJ after amplification [9]. In the first approach, a customized ps-OPA will be used to provide a tunable source in a typical three beams ps-CARS setup. The second approach will focus on the ps-filamentation for ps-CARS to simultaneously detect various gases and its potential industrial applications. However, in harsh environments e.g. in hazardous areas or in a combustion device, it is difficult to achieve a defined overlap for pump and probe pulses at long distances especially when one has limited access in the large-scale experiments. Therefore, in the third approach, remote sensing with CARS will be introduced. Here, a Ti:sapphire chirped pulse amplifier with a pulse duration of 35 fs is used to generate fs-filamentation. During the fs-filamentation, lasing action from $N_2{}^+$ at 391 nm is investigated for CARS experiments in different gases. With the air lasing pulse as probe in CARS, remote CARS is promising for remote sensing applications in harsh environments.

Structure of this thesis

This thesis is divided into seven chapters, starting with the first chapter introduction. Chapter 2 ("State of the art") covers an overview of the current state for different CARS techniques and the aim of this thesis will be given. Subsequently, Chapter 3 ("Fundamentals") demonstrates the basic concepts in molecular Raman spectroscopy including Raman scattering, rotational and vibrational transitions. Additionally, the fundamentals of the main technique CARS are introduced including the theory of phase matching conditions and the dephasing of initial Raman coherence. Furthermore, a brief summary of the physics of filamentation, spectral broadening and generation of lasing during filamentation is given. Chapter 4 ("CARS based on a reliable ps-laser system with OPA") introduces a high resolution ps-CARS system for high temperature gas-phase analysis. Chapter 5 ("CARS based on ps filamentation") describes the characterization of the broadened spectra under different focusing conditions and detection of CARS signals in air for concentration

analysis. In Chapter 6 ("Remote CARS based on fs filamentation"), the lasing signal at $\sim$ 391 nm induced in fs-filamentation was detected under different focusing conditions. Implementing the lasing signal as a probe, the CARS signals of various gases were observed, which enables the remote CARS by employing a single laser pulse. Finally, Chapter 7 concludes the work and gives an outlook beyond this work.

Chapter 2

State of the art

2.1 Current state of the art and challenges

CARS spectroscopy is widely used for in-situ temperature and species concentration measurements in harsh environments (e.g. combustion diagnostics). This chapter briefly reviews the current development and applications of CARS spectroscopy applied with different types of laser systems for gas phase temperature and concentration diagnostics.

2.1.1 Nanosecond laser based CARS

Originally, the CARS technique was used with nanosecond (ns) lasers for nitrogen and hydrogen temperature and concentration measurements [10–12]. In traditional ns laser based gas phase CARS spectroscopy, it needs three laser beams [13]: pump (ω_P), Stokes (ω_S) and probe (ω_{Pr}) beams with at least two different wavelengths as shown in Fig. 2.1. The pump and Stokes pulses with frequencies ω_P and ω_S coherently excite ro-vibrational molecular levels, when the energy difference between ω_P and ω_S matches the Raman shift of the molecule. Then, the excited molecules at the excited state are probed by the probe pulse with frequency ω_{Pr} to generate the CARS signal at frequency of $\omega_{CARS} = \omega_P - \omega_S + \omega_{Pr}$.

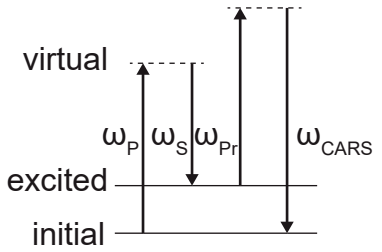


Figure 2.1: Sketch of resonant CARS process energy diagram.

- **Broadband multiplex CARS**

  In most conditions the pump beam has a very narrow spectral bandwidth and the Stokes beam has a rather broad spectral bandwidth for simultaneous excitation of different rovibrational Raman transitions of a molecule as shown in Fig. 3.4. In this method the wavelengths of the pump and probe beams are identical. One of the major advantages in this broadband approach is to enable the acquisition of various rovibrational Raman transitions in a single-shot measurement [14, 15], avoiding the wavelength scanning in the case of three narrow bandwidth laser beams.

  Based on this technique, gas phase temperature and concentration of a single gas species could be extracted simultaneously. Hancock et al. [16] compared the N_2 and H_2 thermometry in hydrogen/air flames using a Hencken burner. The N_2 CARS temperature measurements fit well with the calculation, while the H_2 CARS temperature measurements are on average $\sim 3\%$ higher than the temperature calculated or extracted from the N_2 CARS spectrum. The Stark broadening effects may contribute to the discrepancy with H_2 CARS measurements. However, Woodmansee et al. [17] only observed the influential effects when the intensity of the pump laser beam exceeds 185 GW/cm^2. The high deviation of temperature and concentration is caused by the spectral line broadening and reduced transition strength with increased laser intensity.

  In this broadband laser system it is easy to generate the spectral noise. Therefore, in

the high resolution measurement, it is important to take into account any systematic effects which can lead to spectral line shift and broadening. Any spectral line fluctuations will affect the precision of the measurement. Kaminski et al. [18] showed a standard deviation of $\sim 7\%$ for high precision temperature determination using a modeless dye laser as the Stokes source.

- **Dual-broadband CARS**

  Due to the simultaneous detection requirement for multiple species, dual-broadband CARS was introduced by Eckbreth and Anderson [14]. In this method, two broad laser pulses with spectral widths of ~ 200 cm^{-1} are utilized as pump and Stokes beams for exciting multiple rovibrational Raman transitions [19] or for simultaneous excitation of pure rotational transitions in the vibrational state [14]. More investigations on the N_2 and O_2 CARS have been performed to improve the temperature accuracy of $\sim 3\ \%$ [1]. In this technique, simultaneous excitation of multiple rotational and rovibrational transitions enables more precise temperature measurements.

  Moreover, dual-broadband CARS has also been used to determine the concentration of multiple species. Vestin et al. [20] demonstrated a species-specific weighting procedure with pure rotational CARS to evaluate the relative concentrations of O_2 in mixtures with N_2 with high accuracy. The accuracy of the dual-broadband pure rotational CARS has been evaluated with six techniques including the constant, the inverse and the inverse squared weighted least squares fit of the spectral contour, two varieties of the time- and storage-efficient Fourier analysis and the cross-correlation techniques [21]. Furthermore, most of the rotational CARS studies have not been confined to N_2-O_2 mixtures. CO_2 thermometry using pure rotational CARS has also been investigated for acquiring temperature information [22].

- **Dual-pump ns-CARS**

  Dual-pump ns-CARS originally used two pump beams at fixed frequencies to excite rovibrational transitions of two specific molecules, which also limits the capability of this technique. So Lucht [13] further developed this approach with a narrowband

tunable dye-laser source as one of the CARS pump beams. In comparison with dual broadband CARS, three laser CARS may be more accurate in temperature and concentration measurements. The advantage of using a tunable laser source is that the frequency resolution and separation of the two CARS spectra can be adjusted to optimize temperature and concentration measurement accuracy. Due to the tunable laser source, the dual-pump CARS approach has been widely used for simultaneous excitation of two molecule pairs (e.g. N_2-O_2 [13], N_2-H_2 [23] and N_2-CO_2 [24]). Moreover, using a tunable laser source offers the capability of measuring more than two species simultaneously, as has been demonstrated with dual broadband CARS.

For the determination of gas phase temperature and relative concentration with ns laser based CARS it is important to separate the prominent nonresonant FWM from the resonant CARS signal. The nonresonant FWM distorts and broadens the measured CARS spectrum, which complicates the temperature and concentration measurements. In this regard, suppressing the nonresonant FWM improves the accuracy and detection limit of ns-CARS at higher pressures. Various techniques e.g. pulse shaping [25, 26], polarization sensitive [27], are devised to suppress the CARS nonresonant background.

2.1.2 Picosecond laser based CARS

In the ps laser based CARS the probe beam can be delayed temporally with respect to the pump and Stokes beams to suppress the nonresonant FWM. As mentioned above, the contribution of nonresonant FWM to the signal is only prominent when the pump, Stokes and probe beams overlap temporally.

The first experimental investigation on the nonresonant background suppression in ps CARS is reported by Kamga and Sceats [28]. They demonstrated a two orders of magnitude reduction of the nonresonant FWM in a 10 $\%$ mixture of CS_2 in toluene at a probe delay of ~ 20 ps. The use of short pulse lasers in rich hydrocarbon flame to minimize nonresonant background contributions is investigated by Meyer et al. [29]. Using 135 ps

pump beam, 106 ps Stokes beam and 135 ps probe beam delayed by 165 ps, they detected the nonresonant background-free rovibrational CARS signal of N_2. A three orders of magnitude reduction in nonresonant background is achieved while preserving 60 % - 80 % of the CARS signal.

Seeger et al. [30] investigated the time resolved ps rotational CARS of N_2 for thermometry. In order to suppress the nonresonat background a probe delay of $\sim$ 150 - 500 ps is used. At this interval between pump and probe pulses, molecular collisions can significantly distort the recorded CARS spectrum, which is important for the temperature determination. Thus, molecular collision is a crucial drawback for the ps CARS technique.

2.1.3 Femtosecond laser based CARS

The development of laser systems with ultrashort pulses in fs time domain has opened the possibility to investigate the combustion reactions in real time. In fs-CARS, the nonresonant FWM signal can also be suppressed by controlling the time delay between the laser pulses, as has been demonstrated in ps laser based CARS. In addition, fs-CARS generally shows several advantages: (1) High repetition rates pave the way for much faster detection rate (e.g. 1 kHz [1, 31]) compared to ns-lasers. Fs laser based CARS has the potential to temporally resolve turbulent reacting flows. (2) On the fs time scale molecular collisions can be neglected. Thus, there is no need for a collisional modeling for a high pressure combustion process, which reduces the cost of computation [3]. (3) A single pulse can provide pump and Stokes pulse contributions, simplifying the CARS setup with two-beams or even single-beam configurations [32, 33].

Here, I introduce the three main techniques in fs-CARS to determine temperature and concentration measurements.

- **Time resolved fs CARS**

  Gas phase temperature measurement employing fs-CARS was first conducted by Lang et al. [34]. They demonstrated that the temperature can be extracted from the

beat structures between the populated ground state rotational levels. Using time resolved fs-CARS, Knopp et al. [35] investigated the collision induced rotational energy transfer of N_2 at various pressures. They found out that in the first few ps after the initial Raman excitation, the generated CARS signal is nearly collision-free. Then Beaud et al. [36] demonstrated the use of time resolved fs-CARS for N_2 thermometry in a flame. This technique was further developed by Lucht et al. [3] to determine the temperature and relative concentration of N_2 in Ar from the dephasing rate. The inference beatings between different vibrational bands of N_2 leads to the oscillation in the dephasing rate. This phenomenon was also observed in the gas mixture of N_2-CO [37] and CO_2-O_2 [38]. In some cases, a significant change of the CARS signal decay rate can occur [39], which results in large errors. In 2008 Roy et al. [40] extended the technique to extract the temperature from H_2/air flame within the first few ps after the impulsive excitation.

- **Hybrid fs/ps CARS**

  In hybrid fs/ps CARS, fs laser pulses provide the frequency difference of the pump and Stokes beams to coherently match the rovibrational energy levels of the target molecules. The time delayed ps probe pulses scatter off the excited Raman coherence and generate the CARS signal. Delaying the probe pulses, the decay of the generated CARS signals of the excited rovibrational modes depends on the lifetime of the Raman transitions and their decay rates. When extracting the temperature and concentration information, collisional energy transfer in the time domain or the Raman linewidth in the frequency domain are necessary to be included in the decay rates [41]. Miller et al. [42] demonstrated hybrid fs/ps CARS for vibrational N_2 thermometry in flames. Using a frequency narrowed 2.5 ps pulse as probe, the nonresonant background signal is suppressed by 2 order of magnitude. They also investigated the N_2 rotational CARS with a $\sim$ 8.4 ps probe pulse for temperature measurements with $\sim 1\ \%$ accuracy [43]. In a recent study, Steinmetz et al. [44] investigated the detection limits of the hybrid fs/ps CARS for various gases (N_2, H_2

and CO) on the order of 10^{15} molecules/cm^3. To resolve the Q-branch rovibrational transitions of N_2, Scherman et al. [45] used a volume Bragg grating to obtain a narrowband (0.7 cm^{-1}) probe pulse for high resolution fs/ps CARS.

- **Filamentation based CARS**

  Filamentation based CARS is a specific technique that utilizes laser filamentation for CARS spectroscopy. Filamentation is generally interpreted as the dynamic balance between self-focusing effect, diffraction and defocusing effect by the self-generated plasma. The filamentation of the fs laser provides an option for ultrabroadband excitation due to the spectral broadening of the initial spectrum accompanied with the filamentation. Using broadened spectra generated after filamentation with 45 fs pulses acting as pump and Stokes beams, and the second harmonic at $\sim$ 400 nm as the probe beam, Odhner et al. [46] detected the vibrational CARS signals of various gases up to Raman shifts of $\sim$ 4150 cm^{-1} for H_2. They extracted the temperature information from the wave-packet dynamics in a methane flame. In a recent study, Mazza et al. [47] performed the temperature and relative concentration of CO_2 and O_2 in a flame with filamentation based vibrational coherent Stokes Raman scattering. The broadened spectral width after filamentaion with fs laser is enough to excite Raman transitions up to 1600 cm^{-1}. Furthermore, Tian et al. [48] generated the bandwidth from filamentation up to $\sim$ 3000 cm^{-1} for N_2 vibrational thermometry.

  So far, all of these studies relied on Ti:sapphire based laser systems. These laser systems typically provide pulse durations of $\sim$ 100 fs with energy of multi-mJ at a central wavelength of 800 nm. One of the major advantages is the short pulse duration, which makes it easier to generate additional spectral broadening for ultrabroadband CARS. In addition, air lasing (wavelength of 391 nm) can also be generated during fs-filamentation. This self-generated narrow band lasing beam can be used as probe beam, avoiding the spatial alignment in CARS [49]. However, there are also considerable drawbacks in these laser systems. In combustion or gasification diagnostics, the reaction typically occurs in a sealed reacting device such as a reactor

or an oven. Due to the short pulse durations, the laser pulses are easily subject to dispersion effects from the optical windows. In a recent study, Mazza et al. [4] used an addtional, external compressor to compensate for this with the required pre-chirp. Furthermore, Ti:sapphire laser systems are sensitive to ambient conditions.

In this thesis we used a thin-disk based laser system with pulse durations of ~ 1 ps at a central wavelength of 1 μm for the first two approaches ps-CARS. These laser systems are typically based on reliable fiber oscillators and provide mouch more scalable pulse energy. A recent study reports it can generate hundreds of mJ after amplification [9]. Moreover, recent studies indeed have shown evidence of filamentation in air at ~ 1 ps and at 1 μm [50, 51]. The long initial pulse duration of ~ 1 ps on one hand is advantageous for propagating in dispersive optical windows without chirp. On the other hand, one expects less efficient spectral broadening with this pulse duration, which is challenging for ultrabroadband excitation of multiple species, especially for large Raman shifts (e.g. H_2 with $\sim 4150\,\mathrm{cm}^{-1}$). The first results of Houard et al. [50] showed spectral spanning of ~ 40 nm after filamentation, in contrast to a few hundreds of nm for filamentation of fs pulses at 800 nm [52, 53]. In the so-called "lightning project" [54, 55] filamentation with blue shifted spectrum was observed. However, the broadening of the spectrum after filamentaion was not reported.

Summarizing this brief overview, the main focus of ns laser based CARS has been the simultaneous measurement of temperature and multiple-species concentration on a single shot basis and suppress the collisional and Doppler effects in turbulent reacting flows. Ps- and fs-CARS techniques have been developed and demonstrated to address the limitations encountered by ns-CARS measurements especially for diagnosis of reacting flows. However, ps-CARS has still the same limitations relative to data acquisition and collisional dependence as ns-CARS. Even though fs-CARS has the potential to overcome most of the challenges associated with ns- and ps-CARS: collisional effects and non-resonant background, there are numerous new challenges associated with the propagation of fs-laser

pulses through thick optical windows, stable measurements and remote sensing in harsh environments. Most of the fs-CARS studies relied on Ti:sapphire based laser systems. Normally these laser systems undergo dispersion effects when propagating through thick optical windows. In a recent study, Mazza et al. [4] used an additional, external compressor to compensate the required pre-chirp, which makes the experimental setup complicated. In air fed reacting environment, there are also contributions from other species to the CARS signal e.g. N_2-CO, O_2-CO_2. The effects of polarization interference on the coherence dephasing signal have been investigated [37, 38]. The polarization beating pattern complicates the evaluation of the temperature measurements. Therefore, in this case, a stable and narrow spectral bandwidth (pulse duration of $\sim$ 1 ps) is beneficial for the high spectral resolution measurements. When performing fs-CARS measurements in large scale industrial applications or in hazardous areas, one has limit access to the setup. Therefore, it is difficult to achieve a defined spatial and temporal overlap for the pump and probe pulses.

The aim of this work is to investigate and extend the capability of the CARS technique for gas analysis in harsh environments. In the following chapters we will focus on three approaches: CARS based on a reliable ps-laser system with OPA, CARS based on ps-filamentation and remote CARS based on fs-filamentation.

Chapter 3

Fundamentals

The aim of this chapter is to provide the theoretical background for this thesis. It starts with the basic principles and physical concepts in Raman spectroscopy. Based on these fundamental knowledge, the focus then will be directed into the main technique coherent anti-Stokes Raman scattering (CARS). Finally, a discussion of the physics and potential applications of filamentation in air is presented.

The following fundamentals of Raman spectroscopy and filamentation are based on the books by Peter Atkins [56], See Leang Chin [57] and Y. R. Shen [58].

3.1 Fundamentals of molecular physics

Molecular physics is a branch of physics that deals with the study of the physical properties of molecules, including their structure, dynamics and interactions with electromagnetic radiation. Molecular spectroscopy involves the use of various techniques to investigate the absorption, emission, or sattering of electromagnetic radiation by molecules. These techniques provide valuable information about the electronic, vibrational and rotational structure of molecules, as well as their chemical and physical properties.

There are several types of molecular spectroscopy techniques including:

- **Ultraviolet-visible spectroscopy:** This technique uses ultraviolet or visible light to study the electronic structure of molecules.

- **Infrared spectroscopy:** This technique uses infrared radiation to measure the vibrational modes of molecules.

- **Raman spectroscopy:** This technique uses laser light to study the vibrational and rotational modes of molecules.

- **Nuclear magnetic resonance spectroscopy:** This technique uses magnetic fields to study the electronic and nuclear properties of molecules.

- **Mass spectroscopy:** This technique uses ionization to study the mass to charge ratio of molecules.

Infrared spectroscopy is a type of absorption spectroscopy, which measures the absorption of infrared radiation by molecules. This technique is based on the principle that molecules absorb light at specific frequencies, which are determined by the chemical bonds and the molecular structure. By measuring the frequencies of the absorbed light, infrared spectroscopy can provide information about the types of chemical bonds and functional groups present in a molecule, as well as the molecular structure and composition. However, absorption or emission spectroscopy for homonuclear molecules can be challenging due to the lack of a permanent dipole moment in these molecules (e.g. N_2, O_2 and H_2). Absorption spectroscopy is often used for electronic structure analysis and concentration measurements, while Raman spectroscopy is a valuable technique for studying molecular properties and microscopic analysis.

Raman spectroscopy involves the inelastic scattering of light. When light interacts with a sample, some of the scattered light undergoes a change in energy due to vibrational transitions within the molecules. The energy shifts provide information about the vibrational modes of the molecules. During the scattering event, this process involves a change in the induced dipole moment. Even though molecules like N_2 and CO_2 have no dipole moment, Raman scattering is more likely to occur when there is a change in the molecular polarizability during vibration. The intensity of Raman scattering is generally very small compared to the elastically scattered Rayleigh light. For Raman spectroscopy, only a single laser is needed to interact with the molecules. CARS is a nonlinear optical spectroscopy technique that builds upon Raman scattering. It involves three laser beams as described in the previous section: a pump beam, a Stokes beam, and a probe beam. CARS provides a stronger signal compared to Raman spectroscopy, making it suitable for fast imaging and detection of weak signals.

3.1.1 Vibrational and rotational transitions in molecules

To simplify the explanation of the molecular structures, the following consideration will be based on diatomic molecules. Diatomic molecules consist of two nuclei and electrons around the nuclei. The two nuclei reside in a molecular potential.

- **Vibrational transitions**

  A typical potential energy curve of a diatomic molecule is shown in Fig. 3.1. Near the bottom of the well in Fig. 3.1 (a), the potential energy curve can be approximated by a parabola [56]. The parabolic potential leads to a harmonic oscillation. For the pure vibrational motion, the potential curve is then given by:

$$V = \frac{1}{2}kx^2 \, . \tag{3.1}$$

$$x = R - R_\mathrm{e} \, . \tag{3.2}$$

where k is the force constant of the bond, R is the internuclear distance and R_{e} is the well-defined equilibrium internuclear separation. By solving the Schrödinger equation for the relative motion of two atoms with masses m_1 and m_2 in this parabolic potential curve, one can obtain the permitted vibrational energy levels [56]:

$$E_v = (v + \frac{1}{2})\hbar\omega \quad v = 0, 1, 2... \tag{3.3}$$

$$\omega = \left(\frac{k}{m_{\mathrm{eff}}}\right)^{1/2} \tag{3.4}$$

$$m_{\mathrm{eff}} = \frac{m_1 m_2}{m_1 + m_2} \tag{3.5}$$

Where v is the vibrational quantum number, m_{eff} is the effective mass or reduced mass, and ω is the angular frequency. Normally the energies of vibrational states are described in wavenumbers cm^{-1}, denoted by $G(v)$ [56]:

$$G(v) = \left(v + \frac{1}{2}\right)\tilde{\nu} \tag{3.6}$$

$$\tilde{\nu} = \frac{1}{2\pi c}\left(\frac{k}{m_{\mathrm{eff}}}\right)^{1/2} \tag{3.7}$$

where $\tilde{\nu}$ is the wavelength in cm^{-1}.

In reality, a parabola does not allow a bond to dissociate. Thus, for a more precise description, the potential curve should be replaced by the anharmonic oscillator model. The vibrational energy levels become less widely spaced at high excitations. In Fig. 3.1 (b) the shape of the potential energy curve can be reproduced by the so-called Morse potential curve. Solving the Schrödinger equation for the Morse potential, one can get the permitted energy levels in cm^{-1}:

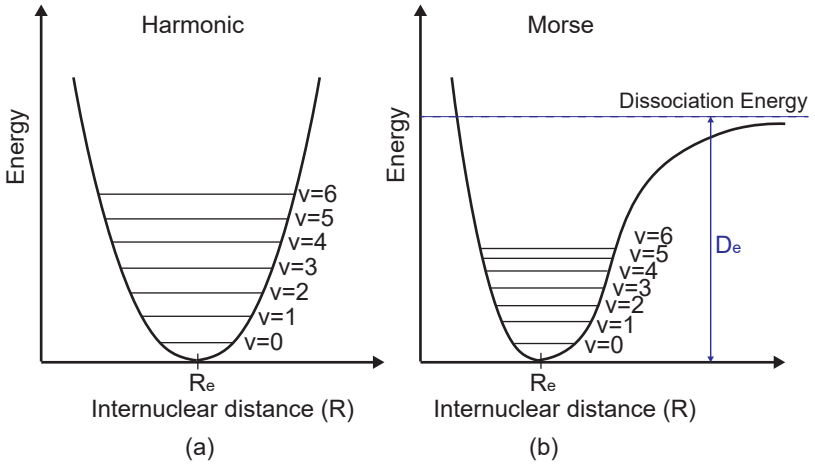


Figure 3.1: Potential curves for harmonic and anharmonic oscillators. (a) Harmonic oscillator: Energy levels are evenly spaced in the harmonic oscillator. (b) Anharmonic oscillator: The energy values are obtained by solving the Schrödinger equation. D_e is the dissociation energy level where the potential curve converges.

$$G(v) = \left(v + \frac{1}{2}\right)\tilde{\nu} - \left(v + \frac{1}{2}\right)^2 \chi_e \tilde{\nu} + ... \tag{3.8}$$

where χ_e is the anhamonicity constant. For higher accuracy more correction terms need to be considered.

- **Rotational transitions**

  In Figure 3.2 the molecule can rotate and vibrate with regard to the effective center of mass like a harmonic oscillator. The way to describe the rotational states is similar to vibrational states. In the linear rigid rotor model, one can predict the rotational energy levels of a diatomic molecule dpending on the moment of inertia of the system I, which is given by:

$$I = m_{\text{eff}} R^2 \tag{3.9}$$

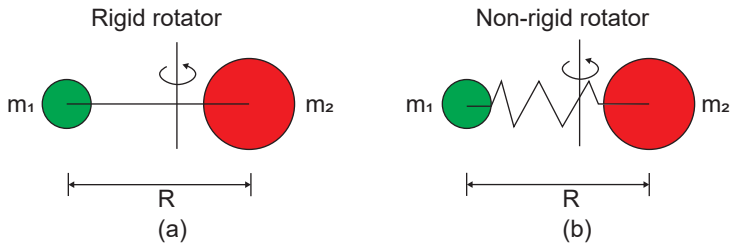


Figure 3.2: Illustration for rotation of diatomic molecules. R is the internuclear distance. (a) Model of a rigid rotator. In a rigid rotator the distance between atoms is fixed. (b) Model of a non-rigid rotator. The fixed rigid connection is replaced by a flexible spring with a constant k.

where m_{eff} is the reduced mass of the molecule and R is the distance between the two atoms.

At the equilibrium position the energy levels of a system can be determined by solving the Schrödinger equation. The quantized energy levels in cm^{-1} are given as [56, 59]:

$$E_{\mathrm{J}} = BJ(J+1) \quad J = 0, 1... \tag{3.10}$$

where J is the rotational quantum number, and $B = \frac{h}{8\pi^2 cI}$ is the molecular rotational constant, which is inversely proportional to the moment of inertia I in equation 3.9.

Since the interatomic distance R between the atoms in the rotating molecule is centrifugally stretched, a stretching centrifugal constant, D, is added to the quantized energy levels. The modified energy levels in cm^{-1} are given by:

$$E_{\mathrm{J}} = BJ(J+1) - DJ^2(J+1)^2 + ... \tag{3.11}$$

For higher accuracy, more correction terms need to be considered.

- **Ro-vibrational states**

  In the previous sections pure vibrational and rotational transitions are considered. However, due to the interactions between molecular vibrations and rotations one generally deals with the combination of both excitations. As Figure 3.2 (b) shows one molecule can vibrate and rotate simultaneously in the model of non-rigid rotator. The anharmonicity of the Morse potential gives rise to an increase of the mean internuclear distance, especially for high vibrational quantum numbers as shown in Fig. 3.1 (b). A larger internuclear distance often corresponds to a weaker bond between atoms, which in turn leads to a shift of the energy levels to lower values. This will lead to a modification of the rotational and centrifugal constants.

$$B \rightarrow B_v = B - \alpha(v + \frac{1}{2}) \tag{3.12}$$

$$D \rightarrow D_v = D - \beta(v + \frac{1}{2}) \tag{3.13}$$

where α and β are the correction constants.

Considering the Equations 3.8, 3.11, 3.12 and 3.13, the rotational-vibrational energy levels are presented in cm^{-1} by the following term [56, 60]:

$$\begin{aligned} S(v, J) &= G(v) + E(J) \\ &= \left(v + \frac{1}{2}\right)\tilde{\nu} - \left(v + \frac{1}{2}\right)^2 \chi_e\tilde{\nu} + B_v J(J+1) - D_v J^2(J+1)^2 \end{aligned} \tag{3.14}$$

In Raman spectroscopy, when photons from the incident light interact with the molecules in the sample, most of the scattered light has the same energy (frequency) as the incident light (Rayleigh scattering). However, a small fraction of the scattered

Table 3.1: Rotational constants (B), centrifugal constants (D) and vibrational constants ($\tilde{\nu}$) for selected molecules in this thesis. All numbers have units of cm^{-1}. The constants for N_2 and O_2 taken from [a]Laher and Gimore [60], for CO_2 [b]Rothman et al. [61], and for CH_4 [c]Richet et al. [62].

Molecules	B	D	$\tilde{\nu}$
[a]N_2	2.0	5.8×10^{-6}	2358.6
[a]O_2	1.5	5.0×10^{-6}	1580.4
[b]CO_2	0.4	1.4×10^{-7}	1341.5
[c]CH_4	5.3	1.2×10^{-4}	3143.0

light undergoes inelastic scattering, resulting in a change in energy (frequency). The inelastic scattering in Raman is associated with changes in molecular vibrational states. In Raman scattering, the interaction of light with molecules leads to a shift in the energy of the scattered photons, which correspond to the energy difference between the initial and final vibrational states. Based on the equation 3.14, each Raman shift can be determined by the energy differences between the corresponding rovibrational energy levels. In this thesis, the combustion gases of interest are N_2, O_2, CO_2 and CH_4. As an example, the typical values of vibrational constant ($\tilde{\nu}$), centrifugal constant (D) and rotational constant (B) are shown in Table 3.1. For the calculation, the Raman shifts of the relevant gases listed in Table 3.2.

3.2 Fundamentals of CARS

This section introduces the CARS process, which is a coherent Raman process. Originally, CARS is used with ns-lasers and normally requires three beams: the pump, Stokes and probe beams, which is typically a three-color process. The pump and Stokes beams with

Table 3.2: Raman shifts for the fundamental and first hot band of relevant combustion gases. Raman shifts of the fundamental and first hot band of N_2 [63], Raman shift of O_2 [64], Raman shifts of CO_2 [65], Raman shift of CH_4 [66].

Molecules	Raman shift (cm^{-1})
N_2	$2330, 2300$
O_2	1556
CO_2	$1388, 1409$
CH_4	2917

frequencies ω_P and ω_S coherently excite ro-vibrational molecular levels, when the energy difference between ω_P and ω_S matches the resonance frequencies of the molecule. Then, the probe pulse at frequency ω_{Pr} gives rise to the CARS signal at frequency $\omega_{CARS} = \omega_P - \omega_S + \omega_{Pr}$.

The CARS process involves a third-order nonlinear interaction between light and matter. In order to generate CARS radiation, the incident beams must be aligned to fulfill the phase matching condition. The phase matching condition ($\overrightarrow{k_{CARS}} = \overrightarrow{k_P}$ - $\overrightarrow{k_S}$ + $\overrightarrow{k_{Pr}}$, where $\overrightarrow{k_P}$, $\overrightarrow{k_S}$, $\overrightarrow{k_{Pr}}$ and $\overrightarrow{k_{CARS}}$ are the wave vectors at frequency of ω_P, ω_S, ω_{Pr} and ω_{CARS}, respectively.) is an essential component for the CARS process. For CARS the maximum of the signal intensity occurs if the phase matching condition has been satisfied. A typical CARS phase-matching process is shown in Fig. 3.3 (a). The simplest way of achieving phase matching in CARS is by collinear configuration as shown in Fig. 3.3 (b). In particular, the collinear setup is easier to implement, however, its realizibility depends on the dispersion of the medium. If phase matching can not be achieved in a collinear configuration, phase matching can be achieved in the "BOXCARS" configuration [67, 68] as shown in Fig. 3.3 (c). The appropriate phase matching angles for the non-degenerate case are related from simple geometric considerations given by [68]:

$$n_P\omega_P \cos\alpha + n_{Pr}\omega_{Pr} \cos\delta = n_S\omega_S \cos\beta + n_{CARS}\omega_{CARS} \cos\gamma \tag{3.15}$$

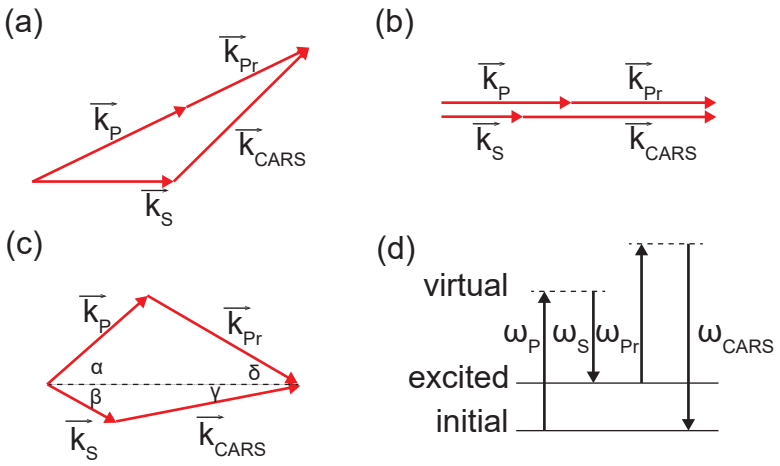


Figure 3.3: CARS approaches for phase matching. (a) General phase matching approach. (b) Collinear. (c) Planar or folded BOXCARS. (d) Sketch of resonant CARS process energy diagram. $\overrightarrow{k_P}$, $\overrightarrow{k_S}$, $\overrightarrow{k_{Pr}}$ and $\overrightarrow{k_{CARS}}$ are the wave vectors at frequency of ω_P, ω_S, ω_{Pr} and ω_{CARS}, respectively.

Figure 3.3 (d) shows the resonant CARS process. The molecules located at the initial state are first excited to the virtual state by a pump beam at frequency of ω_P and achieve temporal and spatial overlap with a Stokes beam ω_S at the excited state. The energy difference between ω_P and ω_S matches the resonance frequencies of the molecule. A further probe beam, with or without delay, interacts with the in phase excited molecule generating a CARS signal at frequency $\omega_{CARS} = \omega_P - \omega_S + \omega_{Pr}$. In traditional ns laser based CARS spectroscopy, each pair of pump and Stokes frequency difference matches only one Raman transition. For nitrogen ns-CARS, the excitation process matches the main two vibrational Raman frequencies (2330 cm^{-1} and 2300 cm^{-1}) as shown in Fig. 3.4 (a). However, in fs CARS, Figure 3.4 (b) shows multiple pump-Stokes pairs contributing the same excitation process, which in turn enhances the generated CARS signal. In fs CARS a pulse with a broadband width (up to 4000 cm^{-1}) can be used for pump and Stokes pulses simultaneously. Combining a narrowband (ps) shaped probe pulse, it generates a Raman coherence in an ensemble of vibrational levels simultaneously. The equations for the nonresonant background in ns- and fs-CARS are similar, but the impact of the background

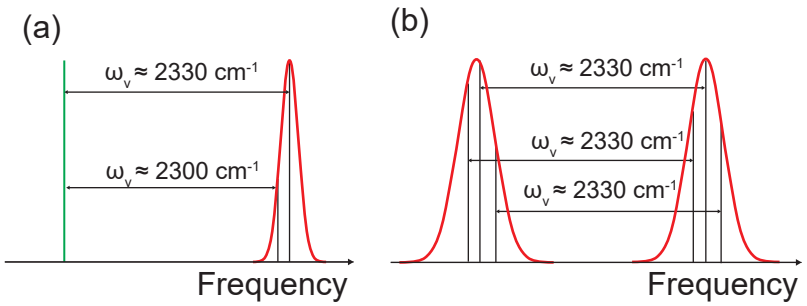


Figure 3.4: Raman excitation of N_2 for the fundamental and the first hot band transitions in ns and fs regime. (a) ns based laser beams as pump and Stokes. (b) fs based laser beams as pump and Stokes.

differs due to the pulse duration and temporal overlap of the laser beams. Due to the longer pulse duration in ns-CARS, the nonresonant background tends to be more pronouced compared to fs-CARS. In general, the overall measured signal combines resonant CARS signal and the non-resonant FWM. Therefore, it is necessary to extract pure resonant CARS signal from the overall measured signal with non-resonant background. The generated CARS signal including the resonant CARS and nonresonant FWM is proportional to [69]

$$\begin{aligned} I_{CARS}(\omega) \propto & |\chi^3(\omega)|^2 \\ &= |\chi^3_{\mathrm{R}}(\omega) + \chi^3_{\mathrm{NR}}(\omega)|^2 \\ &= |\chi^3_{\mathrm{R}}(\omega)|^2 + |\chi^3_{\mathrm{NR}}(\omega)|^2 + 2\Re(\chi^3_{\mathrm{R}}(\omega))\chi^3_{\mathrm{NR}}(\omega) \end{aligned} \tag{3.16}$$

where $\chi^3_{\mathrm{R}}(\omega)$ is the complex vibrational susceptibility.

Due to the distortion of the electronic obits induced by the incident laser fields, nonresonant FWM process (Fig. 3.5) accompanies the resonant CARS signal as described in Equation 3.16. FWM is the third order nonlinear non-resonant process nothing related to the molecular vibrations. In CARS process, pump, Stokes and probe beams are spatially and temporally overlapping, instantaneously leading to nonresonant FWM. Non-resonant FWM mixes with the resonant signal resulting in a rather complicated CARS signal. Several techniques (time-resolved CARS [3, 40] and Fourier transform CARS [70, 71]) have been

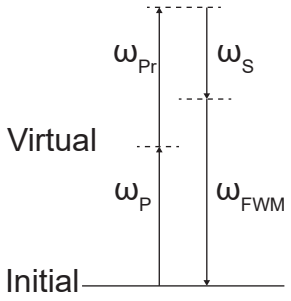


Figure 3.5: Sketch of nonresonant FWM process. In nonresonant FWM process, pump, Stokes and probe beams are spatially and temporally overlapping, instantaneously leading to nonresonant FWM. It is a third order nonlinear non-resonant process not related to molecular Raman vibrations.

used to suppress the non-resonant signal.

3.2.1 CARS intensity

CARS is a third order nonlinear process. To describe the nonlinear optical phenomena the most common way is to use the polarization $\tilde{P}(t)$ in terms of the applied electric field $\tilde{E}(t)$. In this section we derive the intensity of CARS signals from the wave equation and assume the applied optical field with a time dependence [67, 72]:

$$\tilde{E}(t) = E_0 \exp(i\omega t). \tag{3.17}$$

From Maxwell's equations, the well-known wave equation of the CARS signal at frequency ω_{CARS} is thus given by:

$$((\overrightarrow{\nabla})^2 + \frac{\omega_{\mathrm{CARS}}^2}{c^2})E(\omega_{CARS}, \overrightarrow{r}) = -\mu_0 \omega_{\mathrm{CARS}}^2 P(\omega_{CARS}, \overrightarrow{r}) \tag{3.18}$$

where c is the speed of light. μ_0 is the constant of vacuum permeability. $P(\omega_{CARS}, \overrightarrow{r})$ is the induced polarization in the gas.

The left side of the wave equation 3.18 is the electric field of electromagnetic wave going through the gas medium. The right side describes the corresponding polarization of the gas

medium. Depending on the material, the polarization consists of nonlinear components due to the characteristic nonlinear susceptibility χ. Thus, the nonlinear polarization is the source of the CARS signal. In general, the response of the polarization to the electric field can be described by a Taylor expansion. Then the nonlinear susceptibility χ^n with $n \geqslant 2$ is given by:

$$P_{NL}(t) = \sum_n P_{NL}^{(n)} = \sum_n \varepsilon_0 \chi^{(n)} E^n(t) \tag{3.19}$$

Depending on the symmetry of the gas medium, different types of nonlinear effects can occur. For an isotropic gas medium, the induced polarization $P(\omega_{CARS}, \overrightarrow{r})$ is normally given by the linear and third order nonlinear contributions:

$$\begin{aligned} P(\omega_{CARS}, \overrightarrow{r}) &= P^{(1)}(\omega_{CARS}, \overrightarrow{r}) + P^{(3)}(\omega_{CARS}, \overrightarrow{r}) \\ &= \varepsilon_0 \chi^{(1)} E(\omega_{CARS}, \overrightarrow{r}) + P^{(3)}(\omega_{CARS}, \overrightarrow{r}) \end{aligned} \tag{3.20}$$

where the permittivity of free space ε_0 and linear susceptibility $\chi^{(1)}$ have the form:

$$\frac{\varepsilon}{\varepsilon_0} = 1 + \chi^{(1)} \tag{3.21}$$

The third order nonlinear polarization oscillating at frequency ω_{CARS} can be defined by the relation:

$$P^{(3)}(\omega_{CARS}, \overrightarrow{r}) = \varepsilon_0 \chi^{(3)}(\omega_{CARS}, \omega_P, \omega_S, \omega_{Pr}) E_P(\omega_P, \overrightarrow{r}) E_S(\omega_S, \overrightarrow{r}) E_{Pr}(\omega_{Pr}, \overrightarrow{r}) \tag{3.22}$$

where χ^3 is the third order susceptibility of the molecule. This expression for $P(\omega_{CARS}, \overrightarrow{r})$ is now substituted into Equation 3.18, which is thus given by:

$$\begin{aligned} &((\overrightarrow{\nabla})^2 + \frac{\omega_{\mathrm{CARS}}^2}{c^2} \frac{\varepsilon}{\varepsilon_0}) E(\omega_{CARS}, \overrightarrow{r}) \\ &= -\frac{\omega_{\mathrm{CARS}}^2}{c^2} \chi^{(3)} E(\omega_P) E^*(\omega_S) E(\omega_{Pr}) \exp[i(\overrightarrow{k_P} - \overrightarrow{k_S} + \overrightarrow{k_{Pr}}) \cdot \overrightarrow{r}] \end{aligned} \tag{3.23}$$

To solve equation 3.23, one can determine the maximum response only if the phase matching condition ($\overrightarrow{k_{CARS}} = \overrightarrow{k_P}$ - $\overrightarrow{k_S}$ + $\overrightarrow{k_{Pr}}$) is fulfilled as shown in Section 3.2.

In the assumption of slowly varying wave envelope approximation, integrating the propagation distance along z axis from 0 to l, the Equation 3.23 thus can be simplified to:

$$E(\omega_{CARS}, l) = \frac{\omega_{CARS}}{2nc}\chi^{(3)}_{\mathrm{ijkl}}E(\omega_P)E^*(\omega_S)E(\omega_{Pr})\frac{\exp(i\Delta kl)-1}{i\Delta k} \tag{3.24}$$

The intensity is related to the electrical field by:

$$I_{CARS} = \frac{nc\varepsilon_0}{2}|E|^2 \tag{3.25}$$

Through use of Equation 3.24, the CARS signal intensity can be written instead in terms of the product of pump, Stokes and probe intensities:

$$I_{CARS} = \frac{\omega^2_{\mathrm{CARS}}}{n^4c^4\varepsilon_0^2}|\chi^{(3)}_{\mathrm{ijkl}}|^2 I_P I_S I_{Pr} l^2\,\mathrm{sinc}^2(\frac{\Delta kl}{2}) \tag{3.26}$$

From Equation 3.26 the CARS signal intensity is proportional to the square of third order nonlinear susceptibility which encodes the information of temperature and Raman transition of various gases.

For a single isolated spectral line of frequency ω_R, the third order susceptibility at a particular CARS frequency $\omega_P - \omega_S$ may be expressed by [73, 74]:

$$\chi^{(3)} = \frac{2\Delta N_i c^4}{\hbar\omega_{\mathrm{s}}^4}\left(\frac{d\sigma}{d\Omega}\right)\frac{\omega_{\mathrm{R}}}{\omega_{\mathrm{R}}^2-(\omega_{\mathrm{P}}-\omega_{\mathrm{S}})^2-i(\omega_{\mathrm{P}}-\omega_{\mathrm{S}})\Gamma} + \chi_{\mathrm{NR}} \tag{3.27}$$

where χ_{NR} is the non-resonant contribution which arises from background electronic susceptibility contributions and remote Raman resonances. ΔN_i is the molecular population difference between the ground and excited vibrational-rotational states, $d\sigma/d\Omega$ is the differential spontaneous Raman scattering cross-section for a vibrational-rotational transition, and Γ is the Raman linewidth for the corresponding transition. When the frequency difference $\omega_{\mathrm{P}} - \omega_{\mathrm{S}}$ matches with the frequency separation ω_R, the third order susceptibility of CARS signal is significantly increased. Compared with the resonant susceptibility, the contribution of the nonresonant susceptibility to the CARS signal is rather small, especially with a few ps probe delay in the time-resolved fs CARS.

3.2.2 Population distributions

In combustion diagnostics, the primary importance is to find how the molecules are distributed or partitioned over the states. The distribution is a probability distribution related to the state's energy and temperature of the system, which is given by the Boltzmann distribution [11]:

$$N_j = N \frac{g_j \exp(-E_j/kT)}{\sum_j g_j \exp(-E_j/kT)} \tag{3.28}$$

where N_j is the number density of molecules in the jth state. E_j is the energy of state j. N is the total number density. k is the Boltzmann constant. T is the absolute temperature. g_j is the degeneracy of the state, which indicates the number of distinct ways that a certain internal energy level can be occupied in the context of internal energy states of molecules. The distribution shows that the states with lower energy always have a higher probability of being occupied than the states with higher energy. The denominator Q is the canonical partition function:

$$Q = \sum_j g_j \exp(-E_j/kT) \tag{3.29}$$

where the internal molecular energy distribution is the sum of electronic, vibrational and rotational energies:

$$E = E_{el} + E_{vib} + E_{rot} \tag{3.30}$$

Based on Equations 3.29 and 3.30, one can see that the total partition function can be separated and given by the product of a partition function for each internal energy mode. Thus one can consider the molecular population over the electronic energy states, the population distribution over vibrational levels within a given electronic states, and the

population distribution over rotational levels within a given vibrational states. Thus the product of the internal vibrational and rotational partition functions is used to calculate the total internal partition function, which is sensitive to temperature. From the molecular population distributions one can infer the temperature and concentration at the probe volume.

- **Temperature dependence of vibrational populations**

  In the case of a harmonic oscillator, the vibrational energy changes linearly with the vibrational quantum number v. The vibrational partition function can then be expressed as:

$$Q_{vib} = \sum_{v=0}^{\infty} \exp(-vh\nu/kT) \tag{3.31}$$

  where the right hand side of Equation 3.31 is convergent and thus can be simplified to:

$$Q_{vib} = \frac{1}{1 - \exp(-h\nu/kT)} \tag{3.32}$$

  Substituting the Equations 3.32 and 3.29 into Equation 3.28, one can get the vibrational population distribution:

$$N_{vib} = Ne^{-vhc\tilde{\nu}/kT}(1 - e^{-hc\nu/kT}) \tag{3.33}$$

  where $hc/k = 1.44$ K cm.

- **Temperature dependence of rotational populations**

  In the case of an internal rotational mode, the energy states are quantized according to Equation 3.10 with a level degeneracy $(2J + 1)$. The rotational partition function

is thus given by:

$$Q_{rot} = \sum_{J=0}^{\infty} (2J+1) \exp[-hcBJ(J+1)/kT] \tag{3.34}$$

Similar to the vibrational population distribution, the rotational population distribution can be expressed as:

$$N_J = \frac{N}{Q_{rot}} g_I (2J+1) e^{-BJ(J+1)hc/kT} \tag{3.35}$$

where g_I is the nuclear spin degeneracy, which is dependent on J for nonzero nuclear spin. This is related to the symmetry properties of the molecular wave functions. In this thesis, the diatomic molecule N_2 is of great interest. As an example in N_2, the nuclear spin degeneracy g_I is 3, and 1 for O_2 [11].

Considering both vibrational and rotational populations due to the temperature dependence, one can obtain the total molecular population distribution by combining Equations 3.33 and 3.35:

$$N_{vib,J} = \frac{N e^{-vhc\tilde{\nu}/kT}}{Q_{vib} Q_{rot}} g_I (2J+1) e^{-BJ(J+1)hc/kT} \tag{3.36}$$

Based on Equation 3.36 the population distribution can be calculated for a given temperature. In return, the temperature can also be derived from the population distribution. In order to measure the population distribution, one normally measures the dephasing of the initial Raman coherence (see section 3.2.3), which correlates to the CARS signals as a function of the probe delay scan. More details related to the temperature determination can be found in Chapter 4.

3.2.3 Dephasing of initial Raman coherence

In CARS, the molecule is irradiated by two laser pulses (pump and Stokes), leading to a coherent excitation of a vibrational state. This is called Raman coherence. This coherence results in an oscillation between the initial and excited states. However, interactions with the surrounding environment, such as collisions with other molecules or thermal fluctuations, cause the coherence to decay over time. In Raman spectroscopy, dephasing of the initial Raman coherence refers to the loss of coherence between the initial state of the molecule and its excited state, which occurs due to interactions with the environment. The dephasing rate is determined by a variety of factors, such as temperature, pressure and composition of the environment, as well as the properties of the molecule itself.

In broadband fs CARS pump and Stokes beams coherently excite all the accessible transitions. This in-phase Raman coherence achieved by the pump and Stokes dephases due to the frequency spread between the excited transitions of the molecule [37]. The frequency spread dephasing rate of the Raman coherence induced by the fs laser beams is normally used as a measure of gas-phase temperature. Moreover, this dephasing rate of the Raman coherence is independent of molecular collisions and depends only on the frequency spread of the Raman transitions at different temperatures. Thus, one can extract temperatures from a comparison between the theoretical and experimental probe-delay scans of the CARS signal [40]. When the Raman coherence is probed by an additional narrowband (ps) shaped probe beam, this frequency spread dephasing leads to a temporal decay of the CARS signal at a frequency of ω_{CARS}. This decay rate depends on frequency spacings between the excited molecular transitions, the temperature and the probing environments.

3.2.4 Raman cross section

To evaluate the Raman signal strength, Raman cross sections are one of the important factors. The dependence of Raman scattering strength on the differential Raman cross

Table 3.3: Raman tensor invariants for N_2 and O_2. The constants for N_2 and O_2 taken from Lucht [77].

Molecules	$(a')^2$ (C^4m^2/J^2)	$(\gamma')^2$ (C^4m^2/J^2)
N_2	1.515×10^{-59}	2.062×10^{-59}
O_2	1.616×10^{-59}	3.493×10^{-59}

section for the transition is expressed as [11, 75, 76]:

$$(\frac{\partial\sigma}{\partial\Omega})_{zz} = \frac{h(\nu_0 - \nu_k)^4\{(a')^2 + \frac{4}{45}(\gamma')^2\}}{8mc^4\nu_k[1 - e^{-hc\tilde{\nu}/kT}]} \tag{3.37}$$

where $(a')^2$ and $(\gamma')^2$ are the mean and anisotropy invariants of the polarizability tensor. In this thesis the values of $(a')^2$ and $(\gamma')^2$ for N_2 and O_2 used to calculate the transition dipole moments are listed in Table 3.3.

For the zz cross section, the polarizations of the incident and scattered light are perpendicular to the scattering plane. In the case of a small solid angle the radiant intensity can be expressed as $P_{zz}(\theta)/\Omega$. Therefore, the scattered Raman power is given by:

$$P_{scattered} = P_i n(\frac{\partial\sigma}{\partial\Omega})\Omega l\epsilon \tag{3.38}$$

where P_i is the incident laser power. n is the number density of scattering gas species. l is the sampling extent. ϵ is the collection efficiency.

In order to simplify the problem, here we consider only the strongest vibrational transitions with $\Delta v = v' - v = 1$. Then the differential cross section for transition i $\rightarrow$ j is transformed to [78, 79]:

Table 3.4: Molecular parameters for HW factor determination [78].

Molecules	a_1	$(p_2/p_1)_a$	$(p_2/p_1)_\gamma$
N_2	-2.7	0.31	0.57

$$\begin{aligned}(\frac{\partial\sigma}{\partial\Omega}) &= \frac{\pi^2}{\epsilon_0^2}(\tilde{\nu_0}+\tilde{\nu}_{if})^4\frac{\hbar\upsilon}{2m\omega}((a')^2F_a(J)+\frac{4}{45}b(\gamma')^2F_\gamma(J)) \\ &= \frac{\pi^2}{\epsilon_0^2}(\tilde{\nu_0}+\tilde{\nu}_{if})^4M_{if}^2\end{aligned} \tag{3.39}$$

where $F_a(J)$ and $F_\gamma(J)$ are the Hermann-Wallis (HW) factors. b is the Placzek-Teller coefficient, which is related to the rotational transitions. The factor $\frac{4}{45}b \approx 0.022$. M_{if} is the transition dipole moment, which is given by Tejeda et al. [75]. Since $(a')^2$ and $(\gamma')^2$ are normally in the same order of magnitude, the isotropic invariant $F_a(J)$ mainly leads to the variation of the differential cross section. $F_a(J)$ reflects the influence of centrifugal force on the spectral line intensities [78]:

$$F_a(J) = 1-(3(a_1+1)/2-4(p_2/p_1)_{a,\gamma})\gamma^2J(J+1) \tag{3.40}$$

where p_1 and p_2 are the coefficient of isotropic and anisotropic polarizability expansion, respectively. $\gamma = 2B_e/\omega_e$ is the rovibrational coupling.

In this thesis, we mainly focus on the rovibrational peaks of relevant combustion gases (e.g. N_2, O_2). Thus, one can write the spectral intensity $I_{CARS} \propto F_a(J)$. In order to give a rough idea of the variation from the HW factors, we show the typical N_2 molecule as an example. At high temperatures the HW factor $F_a(J) \approx 1.005$, which means that the corresponding CARS signal has 1% variation [78]. For N_2 the HW factor is calculated according to Equation 3.40 using the parameters shown in Table 3.4. The transition dipole moments for N_2 and O_2 are 6.43 $\times$ 10^{-42} $CV^{-1}m^2$ and 6.61 $\times$ 10^{-42} $CV^{-1}m^2$ [77], respectively.

3.2.5 Simulation model of CARS

In the model the CARS signal is expressed in time domain in terms of the time-delay probe pulse with Raman resonant and nonresonant components of polarization [3, 80]:

$$E_{CARS}(t) = E_{Pr}(t)[P_R + P_{NR}] \tag{3.41}$$

The nonresonant polarization is proportional to the instantaneous amplitudes of the pump and Stokes beams, which is thus given by:

$$P_{NR} = \alpha E_P(t) E_S(t) \tag{3.42}$$

where α is an arbitrary scaling parameter.

The resonant polarization for each Raman transition i increases linearly with the integrated product of the pump and Stokes amplitudes and is proportional to the population difference ΔN_i and the Raman cross section $(\frac{d\sigma}{d\Omega})_i$ as shown in Equation 3.27. The explicit linear contribution to the resonant polarization is expressed as [3, 80, 81]:

$$P_R(t) = \beta[\int_{-\infty}^{t} E_P(t')E_S(t')dt'] \times \sum_i \{\Delta N_i (\frac{d\sigma}{d\Omega})_i (\cos\omega_i t) \exp(-\Gamma_i t)\} \tag{3.43}$$

where β is an arbitrary scaling parameter, which is related to the number density of the medium and excitation efficiency from the pump/Stokes beams.

After coherent excitation by the pump and Stokes beam, the polarization of different Raman transitions oscillates with the angular frequency ω_i and decays due to collisions with a rate constant of Γ_i. As visible from Equation 3.41 and 3.42 the nonresonant FWM background is only present, when pump and probe beam overlap in time. In contrast, the resonant Raman polarization is generated by pump and Stokes (Equation 3.43) and can be probed later. Thus, after a few ps delay, the nonresonant FWM is significantly reduced and the resonant CARS signal is dominant. However, for longer delay time, the CARS signal decays due to the oscillation of Raman coherence at slightly different frequencies. Due to

Boltzmann distribution the excited molecules spread over a wide range of rovibrational levels especially at higher temperatures. At atmospheric condition, the collision linewidth $\Gamma_i/(\pi c)$ (for example N_2) is ~ 0.1 cm^{-1}, which corresponds to a characteristic dephasing collision time of 106 ps [3]. Therefore, the collisional dephasing effects are negligible for a probe delay within a few ps. This holds true even at high perssures up to 50 bar. Then we could simplify the resonant polarization to:

$$P_R(t) \quad \propto \quad \beta \sum_i \Delta N_i (\frac{d\sigma}{d\Omega})_i (\cos \omega_i t) \tag{3.44}$$

Here the phase matching condition is assumed to be satisfied. In doing so nearly pure resonant CARS spectrum can be obtained and the nonresonat FWM signal is negligible compared to the resonant CARS signal for a few ps probe delays. So in this study the probe delay time is chosen between $1 - 2$ ps.

One can apply the Fourier transform of the CARS signal in time domain to obtain the CARS spectrum in frequency domain:

$$S_{CARS} = |\int_{-\infty}^{+\infty} E_{CARS}(t) \exp(-i\omega t) dt|^2 \tag{3.45}$$

As discussed previously, the fs CARS signal decays with probe delay time depending on the temperature. This Raman coherence decay can be used to study the initial dephasing of the oscillations of the rovibrational transitions at various frequency spreads [3]:

$$S(\tau) = \int_{-\infty}^{+\infty} I_{Pr}(t-\tau)[P_R(t) + P_{NR}(t)]^2 dt \tag{3.46}$$

where $S(\tau)$ is the signal strength including resonant and nonresonant FWM, while in the case of a few ps probe delay time (τ) the nonresonant contribution ($P_{NR}(t)$) can be neglected.

3.3 Nonlinear optical effects

Nonlinear optics studies the behavior of light in materials where the optical properties depend nonlinearly on the intensity of the light. This results in a variety of interesting and

useful phenomena that are not observed in linear optics. Nonlinear optics involves the use of high-intensity light to induce nonlinear effects in the material. There are several types of nonlinear effects: e.g. Second Harmonic Generation (SHG), Four-Wave Mixing (FWM) and Self Phase Modulation (SPM). In this section the fundamental nonlinear effects and the corresponding principles will be introduced.

3.3.1 Second harmonic generation SHG

SHG occurs in materials that lack inversion symmetry, such as crystals, where the electric field of the incident light interacts with the crystal lattice in a way that produces a second harmonic wave. In this process two photons with the same frequency interact with the crystal, and the resulting wave has a frequency that is twice the original frequency. This effect is highly dependent on the intensity of the incident light and is therefore a nonlinear process.

SHG has many important applications in the field of laser technology, telecommunications, and spectroscopy. In this thesis, SHG is used to double the frequency of lasers, resulting in higher-energy photons for different applications. The efficiency of SHG depends on various factors such as the crystal structure, polarization, phase matching conditions, and the input intensity of the light.

3.3.2 Four-Wave mixing FWM

In FWM, three waves with frequencies ω_1 and ω_2 and ω_3 interact in a nonlinear medium to produce a fourth wave with frequency ω_4. This interaction depends on the phase and amplitude of the input waves and the properties of the medium. The energy conservation law must be satisfied in this process as shown in Fig. 3.5: $\omega_{FWM} = \omega_P + \omega_{Pr} - \omega_S$.

FWM has important applications in many fields, including telecommunications, spectroscopy, and quantum optics. In spectroscopy, FWM (Fig. 3.5) and CARS like FWM (Fig. 3.3 (d)) is used to probe the properties of molecules and materials, providing information

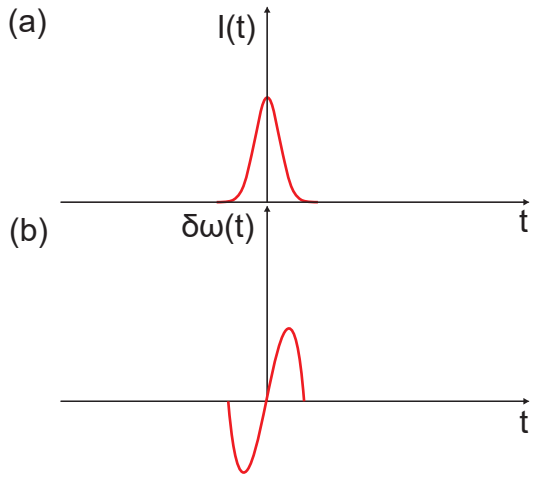


Figure 3.6: Illustration of self-phase modulation. (a) Intensity (b) instantaneous frequency change of a Gaussian pulse during propagation through a medium with positive refractive index.

about their structure and dynamics. The efficiency of FWM depends on various factors such as the input powers and frequencies, the phase matching conditions and the nonlinear properties of the medium.

3.3.3 Self phase modulation SPM

SPM is a nonlinear phenomenon in which an ultrashort pulse propagating through a medium interacts with the medium and induces a phase modulation on itself. This nonlinear phase modulation depends on the intensity profile of the laser pulse and the nonlinear refractive index of the gas. Figure 3.6 shows the instaneous frequency change of a Gaussian pulse during propagation through a medium with a positive refractive index.

3.4 Filamentation physics

In 1962 Askarian first suggested the idea of self-focusing and self-trapping of light beam [82]. Michael Hercher discovered the filamentary damage tracks in glass caused

by Q-switched laser pulses in 1964 [83]. One important feature, frequency broadening in a filament in liquid, was first observed [84]. In 1994, Gérard Mourou and his team first observed the self-focusing and propagation phenomena of filaments induced by femtosecond intense laser pulses in air [85]. Over the last decades, the main features of filamentation have been researched and are now well understood. The propagation of high-power ultrafast laser pulses in air creates the dynamic balance between nonlinear self-focusing effects, diffration and defocusing by the generated strong plasma. Based on the potential applications in gas phase combustion diagnostics, the focus of this section will be on the basic physics of filamentation in air.

Before deriving the mathematical theory of these effects, a simple physical picture of filamentation and spectral broadening will be introduced. In this section three main items self-focusing of ultrafast laser pulses, generation of filaments and the generation of new frequency components under atmospheric conditions will be elucidated.

3.4.1 Filamentation

The Kerr effect is a phenomenon in which the refractive index of a material changes in response to the intensity of the incident light. It is named after John Kerr, who first observed the effect in 1875. Due to the spatial intensity distribution the Kerr effect transforms the material through which the light is propagating into a gradient index lens. As a consequence, the laser light starts to self-focus. The dynamic competition between nonlinear Kerr self-focusing and plasma defocusing leads to the propagation of intense laser pulses for a long distance. This phenomenon is well known as filamentation. The formation of a filament due to the self-focusing effect has important applications in the field of remote sensing and spectroscopy.

Filamentation is generally interpreted as the dynamic balance between the self-focusing effect, diffraction and the defocusing effect by the generated plasma. There are slight differences in the formation of filamentation with nanosecond, picosecond and femtosecond laser pulses. When focusing an intense nanosecond and picosecond laser pulses in air or

condensed matter, optical breakdown is easily observable. Since the mean free time of a free electron is $\sim$1 ps in air, there is not enough time for the free electron to undergo collisions with the surrounding molecules in the femtosecond regime. This section is mainly focused on the physical phenomena and filamention propagation with pulse durations of $\leqslant$1 ps.

- **Self-focusing of laser pulses**

  To achieve self-focusing the transverse spatial intensity distribution of the laser pulses has to be inhomogeneous. In the following, the laser pulse is approximated as a plan-wave pulse and is assumed to be the Gaussian intensity distribution on the transverse cross-section of the pulse as shown in Fig. 3.7. Perpendicular to the propagation direction the laser pulse is sliced, of which the thickness is at least $c\tau$, where c is the speed of light in vacuum and τ is the oscillation period of the laser pulse. Since intensity is generally defined as the Poynting vector averaged over at least a cycle of oscillation of the field τ, the distribution of intensity across each slice is considered here. If the intensity of the central region is high enough and the nonlinear Kerr effect cannot be neglected, the refractive index n at the central region of the slice is

$$n = n_0 + n_2 I \tag{3.47}$$

  where n_0 is the refractive index in air and the refractive index at the edge of the slice. n_2 is the coefficient of the Kerr nonlinear refractive index related to the third order susceptibility χ^3 and I is the laser field intensity. $n_2 I$ is the Kerr nonlinear index.

  Figure 3.7 illustrates the self-focusing of an initial plane wave slice with ultrafast laser pulses in air. The propagation speed of the slice is given by c/n. Due to higher refractive index ($n_0 + n_2 I$) in the case of positive n_2 in the center, the central part of the slice propagates slower than the rest of the slice resulting in a concave wavefront, which is the beginning of self-focusing. The beam diameter reduces. However, this

leads to increased diffraction. Thus, when the peak power reaches a certain point where the self-focusing effect is just balanced by diffraction, the peak power at this point is defined as the critical power for self-focusing P_c, which is given by

$$P_c = \frac{3.77\lambda^2}{8\pi n_2 n_0} \tag{3.48}$$

where λ is the central wavelength of the pulse. The critical power for self-focusing is inversely proportional to the nonlinear refractive index n_2, which is not constant in air. Depending on the pulse duration of the laser pulses, the critical power in air changes from 5 GW to 10 GW [86, 87]. The physical reason is that different responses of the medium to an electromagnetic wave contribute to the change of nonlinear refractive index n_2. If the laser pulse duration is shorter than 100 fs, only an instantaneous electronic response of the media contributes to the polarization, which in turn is responsible for the nonlinear refractive index n_2. While with longer pulse duration both instantaneous and delayed nuclear response contribute to the nonlinearity.

During the propagation of self-focusing laser pulses, the slice is curved into a smaller and smaller area and the center intensity gets higher and higher. Finally, the high intensity in the center area will lead to tunnel ionization of air molecules, which causes the generation of a weak plasma. If the pulse power is far beyond the critical power, a denser plasma is generated due to tunnelling ionization. The generated free electrons have a defocusing effect and thus counteract the Kerr nonlinear self-focusing effect in the center area. The refractive index change of the slice in the plasma is given by

$$\Delta n_p = -\frac{4\pi e^2 N_e(t)}{2m_e\omega_0^2} \tag{3.49}$$

where e, N_e, m_e are the electronic charge, density and mass of electrons, respectively.

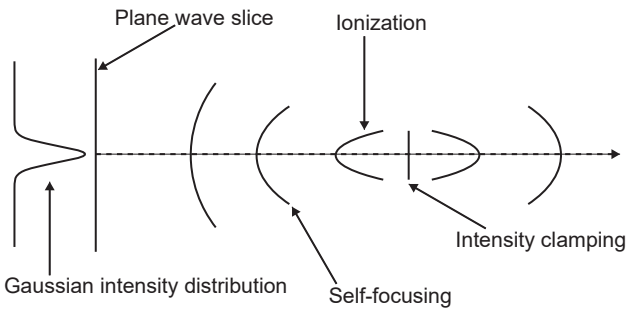


Figure 3.7: Illustration of self-focusing of a slice with Gaussian distribution across the transverse plane. The center area of the initial plane wave has a higher refractive index due to higher Kerr nonlinearity, thus this section travels slower than the rest of the slice. The velocity difference results in the self-focusing and a shape of concave slice front. When the self-focusing becomes stronger, the intensity in the center will be strong enough to realize ionization. The generated plasma starts to defocus the beam, which balances the self-focusing process, where the intensity starts to clamp (maximum intensity point).

ω_0 is the central frequency of the pulse. Then the refractive index of the slice in the center becomes

$$n = n_0 + \Delta n(t) \tag{3.50}$$

$$\Delta n(t) = n_2 I - \frac{4\pi e^2 N_e(t)}{2m_e\omega_0^2} \tag{3.51}$$

The central part propagates faster in speed. Therefore, the defocusing effect of plasma makes the slice begin to flatten. But as long as $\Delta n(t) > 0$, which is the Kerr self-focusing effect is greater than the defocusing effect of plasma, the beam diameter further decreases and consequently the intensity increases. Due to the

high nonlinearity of tunnel ionization, the plasma defocusing effect increases much faster than Kerr self-focusing effect. So when $\Delta n(t) = 0$, Kerr self-focusing effect balances the defocusing effect of free electrons. At this point, intensity clamping occurs. The position where the intensity clamping occurs is given by [88]

$$z_f = \frac{0.367ka^2}{\{[(\frac{P}{P_c})^{1/2} - 0.852]^2 - 0.0219\}^{1/2}} \tag{3.52}$$

where k is the wave number and a_0 is the beam radius. P is the peak power.

However, in the laboratory condition, to control the position of the filaments and stabilize the filaments, an additional focusing lens is mostly used to generate filamentation. In this condition the self-focusing effect is reinforced by the external lens. Thus, the new focusing distance appears before the geometrical focusing position and is given by

$$\frac{1}{z_f^{'}} = \frac{1}{z_f} + \frac{1}{f} \tag{3.53}$$

where $z_f^{'}$ is the new self focusing position and f is the focal length of the external lens.

This dynamic balance as illustrated in Fig. 3.8 could propagate up to kilometer length [89], which could be used for remote sensing applications (e.g. light detection and ranging LIDAR [90]).

- **Single and multiple filamentation**

  If the transverse fluence distribution of the Gaussian pulse is smooth, only one filament occurs if the peak power P is not more than 2-3 times of the critical power P_c [57]. However, when the laser pulse peak power exceeds the critical power P_c by more than an order of magnitude [91, 92], multiple filaments are generated either due to the inhomogenity of energy distribution in the initial beam profile or random noise induced by air turbulence [93].

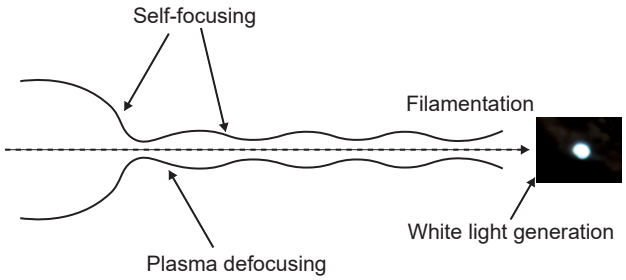


Figure 3.8: Scheme of the evolution of filamentation propagating in an optical medium. The dynamic competition between self-focusing and plasma defocusing leads to the prapagation of intense laser pulses over a long distance. The direction of the propagation is towards the right side. At the end of the propagation, a colorful white light as an example is generated. The white light shown here is generated with a pulse duration of $\sim$1 ps and a pulse energy of 40 mJ.

In this section the formation and propagation of filamentation has been introduced in detail. In addition to the dynamic balance between nonlinear Kerr self-focusing of laser beam and defocusing of the generated plasma for remote sensing, the spectrum after the filamentation is also getting broadened due to the optical nonlinearities.

3.4.2 Spectral broadening

Spectral broadening from self-focusing of a Q-switched laser pulse in liquids was first proposed and explained by Shimizu using self-phase modulation (SPM) [84].

During filamentation of intense laser pulses in gases, the frequency spectrum is expanded towards both the red and blue sides due to the optical nonlinearity (e.g. SPM and self-steepening). Temporal variation of refractive index leads to the SPM in an optical medium. SPM will in turn cause the generation of supercontinuum and white-light emission.

In order to understand how the spectrum is broadened by the optical nonlinearities, the following explanation will be given according to theoretical calculation at the self-focus, where intensity clamping occurs. At this point, the wave front becomes plane as shown

in Fig. 3.7. To simplify the explanation, a plane wave for the self-focused wave front is assumed. So the plane wave front at the self-focus is given by:

$$F(z,t) = exp\{i[\omega_0 t - kz]\} = exp\{i[\omega_0 t - \frac{\omega_0 n}{c} z]\} \tag{3.54}$$

where z is the propagation distance. Inserting Eq. 3.50 into Eq. 3.54, it becomes

$$\begin{aligned} F(z,t) = &\quad exp\{i[\omega_0 t - \frac{\omega_0 n_0}{c} z - \frac{\omega_0 \Delta n(t)}{c} z]\} \\ = &\quad exp\{i[(\omega_0 t - \frac{\omega_0 n_0}{c} z) + \int_0^t \frac{\partial(-\frac{\omega_0 \Delta n(t)}{c} z)}{\partial t} dt]\} \\ = &\quad exp\{i[(\omega_0 t - \frac{\omega_0 n_0}{c} z) + \int_0^t (\Delta\omega) dt]\} \end{aligned} \tag{3.55}$$

where $\Delta\omega$ is the frequency shift and given by

$$\Delta\omega = \frac{\partial(-\frac{\omega_0 \Delta n(t)}{c} z)}{\partial t} = -\frac{\omega_0}{c} z \frac{\partial[\Delta n(t)]}{\partial t} \tag{3.56}$$

The Kerr effect and plasma generation result in the modulation of the phase of the laser pulses due to the self-generated extra phase $-\frac{\omega_0 \Delta n(t)}{c} z$. In general, the front part of the laser pulses always see a neutral gas and then the plasma contribution is negligible. From Equations 3.51 and 3.56, the frequency shift is then given by

$$\Delta\omega = -\frac{\omega_0}{c} z \frac{\partial[\Delta n(t)]}{\partial t} = -\frac{\omega_0 z}{c} n_2 \frac{\partial I_{front}}{\partial t} < 0 \tag{3.57}$$

From the last inequality in Eq. 3.57, the front part of the laser pulses has a positive temporal slope. Therefore, the front part of the laser pulses mainly contributes to a red frequency

shift/broadening. Since the gas is only partially ionized, SPM in the neutral gas in the back part of the laser pulses can also lead to a blue shift/broadening. But this blue shift is smaller compared to the strong blue shift/broadening due to SPM in the plasma together with the SPM due to the steep descent of the back part of the laser pulses (self-steepening).

One can attribute the blue shift/broadening of the frequency to the highly nonlinear dependence on the high intensity inside the self-focal region. In addition to the SPM, the intensity distribution in the back part of the laser pulses becomes very steep and the slop is negative at the end of the propagation. Moreover, the ionization is also negligible at the end of the filamentation. This leads to a large blue frequency shift

$$\Delta\omega = -\frac{\omega_0}{c} z \frac{\partial[\Delta n(t)]}{\partial t} = -\frac{\omega_0 z}{c} n_2 \frac{\partial I_{back}}{\partial t} > 0 \tag{3.58}$$

In summary, the nonlinear effects lead to the generation of red-shifted frequencies (SPM) at the leading edge of the pulse and blue-shifted frequencies (SPM and self-steepening [94]) at the trailing edge of the pulse.

3.4.3 Lasing of N_2^+ during filamentation in air

The generation of the filamentation in air is typically accompanied by two significant features, which include the laser-like emission (so-called air lasing) from nitrogen ions and spectral broadening of the incident pulse. The spectral broadening has been introduced in the previous section. In standard lasers, a resonant cavity composing of optical mirrors is one of the basic elements for laser operations. However, air lasing can be achieved in a cavity-free scheme, in which ultrashort intense laser pulses propagating in air generate a self-seeded laser emission.

Lasing emission was observed in forward direction at ∼391 nm and ∼428 nm either with [95] or without seeding at a probe pulse wavelength of 400 nm [96]. The gain mechanism for the required population inversion in N_2^+ has been discussed to result from

in electron recollision [97] or population distributions in rotation levels of the upper and lower lasing states [98]. The intense fs laser pulses induce the ionization of an electron from (σ_u2s)-or (σ_g2p)-orbital. Thus, it leaves the ion in excited states Σ_u^+ and Σ_g^+, respectively [99]. A recent study proposed a new lasing mechanism without population inversion [100]. Moreover, Li et al. demonstrated the influence of a time-dependent polarization on the 391 nm lasing [101]. N_2^+ lasing is not limited to filamentation, but was also observed when spectrally broad, sub-10 fs pulses lead to plasma formation in the laser focus [102]. Remote sensing based on fs-filamentation CARS enables possible applications including the spectroscopic analysis of the atmosphere [103] or the remote characterization of rotational wave packets [104]. Although backward directed emission is highly beneficial for remote sensing applications, so far it has only been observed for N_2^+ at low pressure [105], and for species such as O_2 [106], N_2 [107, 108], atomic hydrogen [109], and atomic oxygen [110]. In this regard, backward stimunlated Raman scattering was used for detecting atmospheric gases [111].

Chapter 4

CARS based on a reliable ps-laser system with OPA

4.1 Overview

N_2 and O_2 fs CARS are typical means of measuring the gas phase temperatures. In general, the studies related to N_2 CARS thermometry are based on the population difference of the selected resonances of rovibrational transitions in the ground state of N_2 molecules. In air fed reacting environments, there are contributions not only from N_2 but also from other species like CO. Roy et al. [37] investigated the effects of polarization interference between N_2 ($\sim$2330 cm^{-1}) and CO ($\sim$2145 cm^{-1}) on the coherence dephasing signal after impulsive excitation with 80 fs laser pulses. The similar polarization beating in O_2-CO_2 atmospheres with fs-CARS was investigated by Kulatilaka et al. [38]. In this case, one of the major combustion related species CO_2 (Fermi dyads at 1285 cm^{-1} and 1388 cm^{-1}) will be simultaneously excited with O_2 ($\sim$1556 cm^{-1}) due to the broad initial bandwidths of the pump and Stokes laser pulses. Comparing to the diatomic molecule pair N_2-CO system, the three Raman polarizations in O_2-CO_2 even complicate the evaluation of the temperature measurement. Therefore, in order to investigate the characteristics of Raman transitions of various gases (e.g. N_2, O_2, CO_2, CO, CH_4 and H_2) in general, a widely

tunable, narrow spectral bandwidth (pulse duration of $\sim$ 1 ps) laser system providing pump, Stokes and probe beam is beneficial. But in order to detect single vibrational transitions of N_2, one needs a setup with sufficient spectral resolution of $\sim$ 30 cm^{-1} to separate the fundamental (2330 cm^{-1}) and first hot band (2300 cm^{-1}) peaks.

An optical parametric amplifier (OPA) is typically used to provide three beams with different wavelengths. An OPA uses a nonlinear optical crystal with a large second order susceptibility to transfer energy from a fixed frequency pulse to two variable frequencies, lower photon energy output pulses. The fs-OPAs are typically based on Ti:sapphire pump lasers [112–114], which is sensitive to ambient conditions. However, there is a lack of systems for industrial applications, which provide ps output pulses. A prerequisite for this is a ps pulse laser system, typically based on Yb:doped gain media.

In this chapter, a customized OPA in combination with a commercial thin-disk based 1 kHz laser system is shown, providing a pulse energy of $\sim$200 μJ over the full tuning range from 700 to 950 nm with a pulse duration of $\sim$1 ps. Because of the high pulse energy and an almost constant spectral bandwidth around $\sim$18 cm^{-1} across the whole tuning range, this setup is well-suited as a ps-CARS system for combustion diagnostics. We prove the feasibility with N_2 and CO_2 CARS for temperature determinations compared with the simulations.

4.2 Optical parametric amplifier OPA system

A thin-disk regenerative amplifier (Dira-500-10, Trumpf Scientific Lasers GmbH + Co. KG, Germany) is used as pumping source for the OPA, providing a maximum pulse energy of 60 mJ at a repetition rate of 1 kHz and a pulse duration of $\sim$1 ps at 1030 nm. The laser beam is linearly (horizontally) polarized and has a Gaussian beam profile with a diameter of 12.7 mm ($1/e^2$). In the customized OPA system (APE Angewandte Physik & Elektronik GmbH, Germany), the pulse energy of the pump source is set to 8.9 mJ, as shown in Fig. 4.1. In front of the OPA device, a beam splitter (BS1; 50:50) is used to split the pump

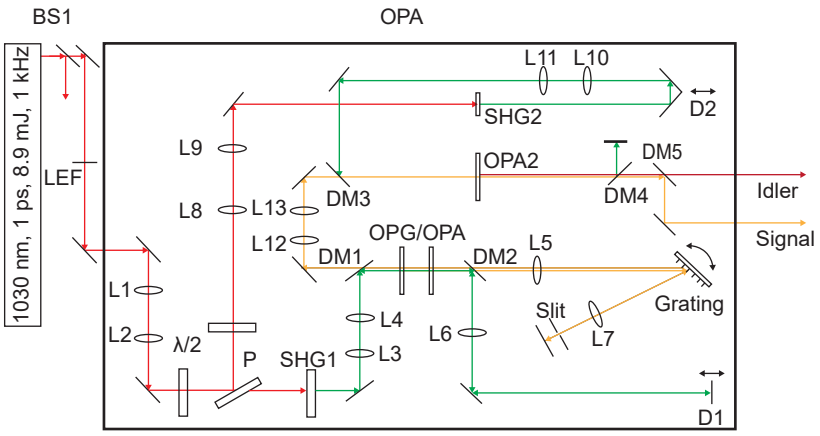


Figure 4.1: Scheme of the optical parametric amplifier system. BS1: Beam splitter with R:T = 50:50. LEF: ultra-steep long-pass edge filter. $\lambda/2$: half-wave plate. P: polarizing beam splitter. SHG1 and SHG2: BBO nonlinear crystals. Telescopes: f_{L1}:f_{L2} = 5:1, f_{L8}:f_{L9} = 1:3.3, f_{L12}:f_{L13} = 1.5:1, f_{L10}:f_{L11} = 5:3. D1-D2: motorized delay state. DM1-DM5: dielectric mirrors.

laser pulses into two branches. The transmitted pulse is used to drive the OPA, while the reflected pulse is used as Stokes beam and generation of probe beam for the CARS experiments (see section 4.3). To obtain comparable spectral widths with the thin-disk pump laser source ($\sim$1 ps), an ultra-steep long-pass edge filter (LEF) is rotated to a certain angle in front of the OPA to cut off roughly half of the initial spectrum and the power. After the LEF filter, $\sim$2.5 mJ of the laser pulse energy at 1030 nm is used to drive the OPA.

Inside of the OPA, the beam size is first reduced by a telescope (L1:L2 = 5:1), before the pulse is split by a combination of half-wave plate and polarizer into two different stages (seed generation stage and main amplification stage). In the seed generation stage, the transmitted pump pulses act as pumping pulses for the subsequent parametric amplification processes after frequency-doubling to a wavelength of $\sim$ 515 nm by passing through a BBO-based second harmonic generation (SHG) stage. The seed spectrum is generated by phase-matched optical parametric generation (OPG) in an OPG/OPA double pass setup.

Between the first and second path, the spectrum is significantly narrowed via a folded 4-f shaper with an adjustable slit aperture in the Fourier plane. The grating of the shaper is rotatable to enable a wide tunability of the transmitted center wavelength. In the main OPA amplification stage (OPA2), the pulses reflected by the polarizer (P) generate the main SHG pump beam to a wavelength of ∼515 nm by a nonlinear BBO crystal (SHG2). The seed pulse and the main SHG pump beam are combined by a dichroic mirror (DM3). After the double path OPG/OPA-stage, the seed pulse energies of μJ levels are amplified in the main OPA stage to above 100 μJ.

4.2.1 OPA performance

The initial spectrum of the thin-disk pumping source and the spectrum after the long-pass edge filter are shown in Fig. 4.2. The spectral widths before and after the edge filter are 1.74 nm and 0.79 nm, and the corresponding powers are 5.14 W and 2.50 W, respectively. We investigate the spatial distribution of the output pulses from the OPA with a CCD camera (Coherent beamviewer). Figure 4.3 (a) and (b) show the beam profiles of the output beam from the OPA at 800 nm and 900 nm signal wavelength, respectively. The distribution of the intensity can be fitted utilizing a Gaussian function. The left and lower side of the images show the cuts through the beam profiles in vertical and horizontal directions with the Gaussian intensity fits. For the beam profile at 800 nm, the length of the major axis is measured to be ∼2.83 mm und the length of the minor axis is ∼2.27 mm. The similar phenomenon of the beam profile has been reported in the far field. This indicates some astigmatism, probably due to crystal orientation and different M^2 of the pump beam in the horizontal and vertical directions [115, 116].

Furthermore, we measured the pulse durations of the thin-disk pumping source and the OPA output signal with a SHG-autocorrelator (Pulse check, APE Angewandte Physik & Elektronik GmbH, Germany). Figure 4.4 (a) shows the measured pulse durations for the full tuning range, which indicates a pulse duration ∼1 ps of the OPA output nearly independent of the wavelength. Assuming a sech^2 pulse shape, a small fraction of the

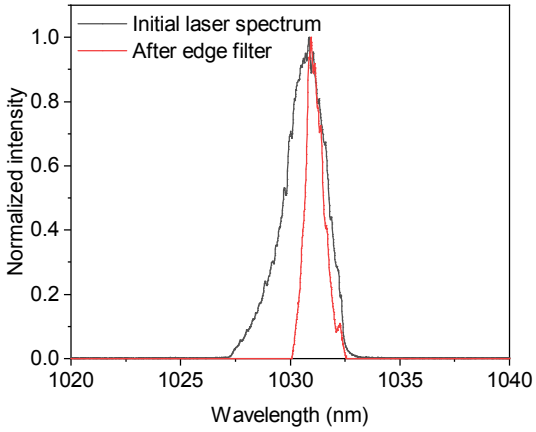


Figure 4.2: Spectra before and after the long-pass edge filter. One ultra-steep long-pass edge filter is tilted to a certain angle which cuts off roughly half of the initial pump spectrum to narrow the OPA input spectrum and elongate the input pulse duration.

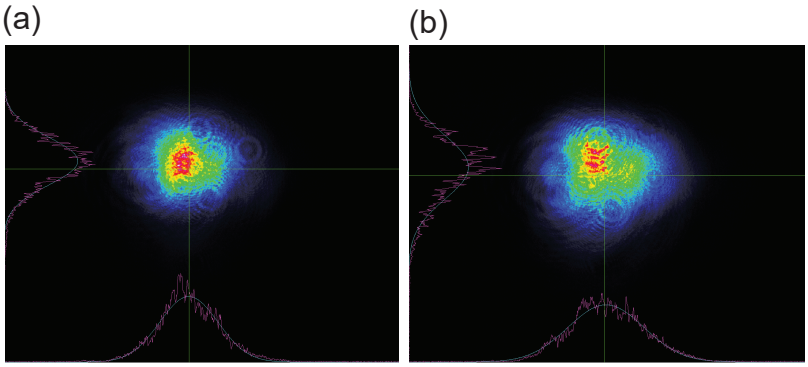


Figure 4.3: The collimated OPA output beam profiles. The corresponding near-field beam profiles (a) at 800 nm and (b) 900 nm are slightly deformed with respect to a fundmental Gaussian mode due to phase distortions, crystal orientation and different M^2 of the pump beam in the horizontal and vertical directions.

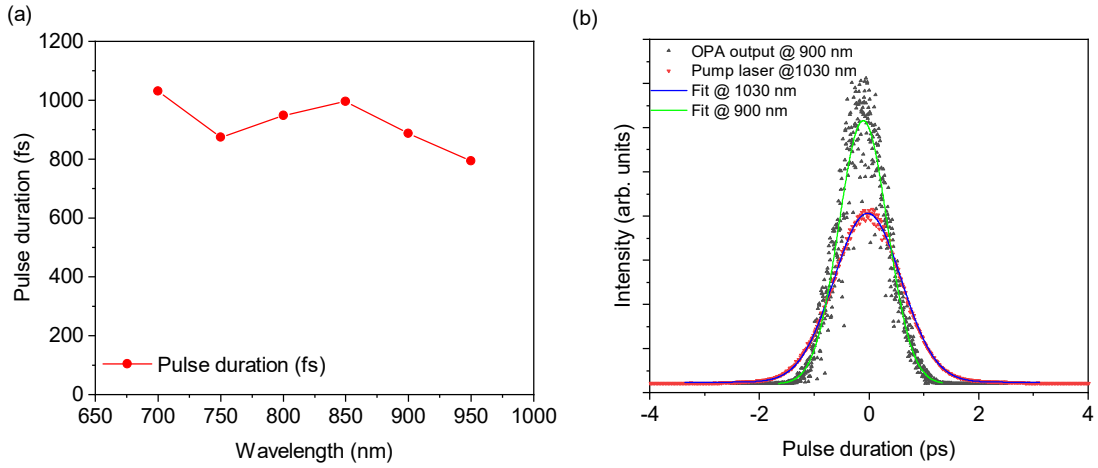


Figure 4.4: Autocorrelation measurement of the OPA output and the thin-disk pump laser. (a) The measured pulse duration corresponding to the tuning range. (b) Auto-correlation at 1030 nm and 900 nm. Assuming a sech^2 pulse shape, the pulse duration of the pumping source is 1020 fs and 885 fs for the OPA at 900 nm as an example.

OPA pump beam and the OPA ouput at 900 nm as an example are taken, yielding pulse durations of 1020 fs and 885 fs (Fig. 4.4 (b)), respectively.

Next, we investigate the spectral width of the OPA output. To get comparable spectral width with the initial laser spectrum (1.74 nm / 17 cm^{-1}), the edge filter (LEF) described above is used. Here, the OPA output at 900 nm as an example is taken, yielding spectral width of 1.44 nm / 18 cm^{-1} as shown in Fig. 4.5. Due to the combination of the robust seed generation via OPG together with an adjustable narrow-band spectral shaper, the signal output spectrum of the OPA system is tunable over a wide range from 700 to 950 nm with an almost constant spectral bandwidth of 17 cm^{-1} (1.6 nm) to 20 cm^{-1} (1.0 nm) as shown in Fig. 4.6, which is comparable to the spectral width of the initial laser spectrum. Over the full tuning range of the OPA from 700 nm to 950 nm, the OPA output energy is 140 - 290 μJ at 1 kHz, as presented in Fig. 4.7. We measured the power stability (RMS) of the thin-disk pump source and the OPA at 900 nm for 1 hour at 1 kHz, which is 0.5 % and 1.1%, respectively.

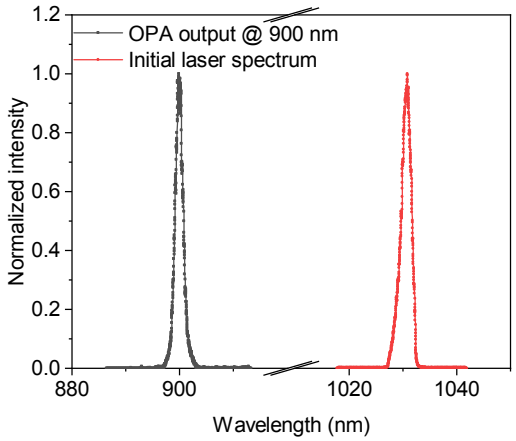


Figure 4.5: Spectral width of the OPA output at 900 nm and the initial laser spectrum. The spectral width of the OPA output at 900 nm as an example and the initial laser spectrum are 1.44 nm and 1.74 nm, respectively.

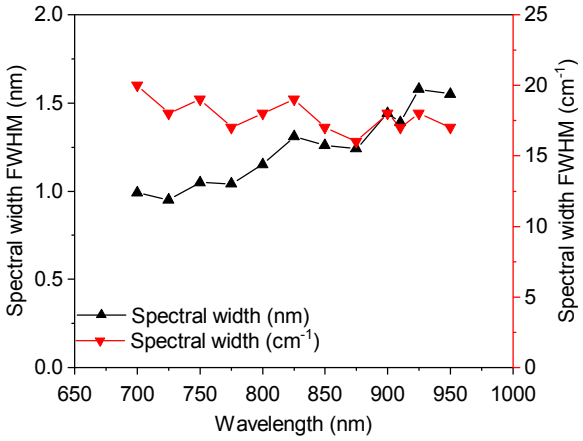


Figure 4.6: Spectral width of the signal output of the OPA over the tuning range. The signal of the OPA system is tunable from 700 nm to 950 nm with an almost constant spectral width between 17 to 20 cm^{-1}.

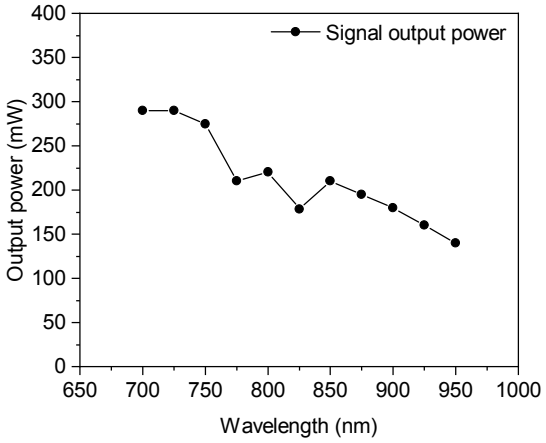


Figure 4.7: Signal output power of OPA over the entire tuning range from 700 nm to 950 nm.

4.3 The ps-CARS setup

As described in section 3.2, the phase matching condition can fulfilled in gases when all three beams are collinear aligned. In the CARS process as shown in Fig. 4.8 (a), we use the signal of OPA as pump, the fundamental pulses of the thin-disk laser at 1030 nm as Stokes and the SHG at ∼515 nm as probe. Figure 4.8 (b) depicts the collinear ps-CARS setup. We use a 50/50 beam splitters (BS2) to split the beam into two branches. To adapt the beam size to the size of the signal beam of the OPA, the beam size of these two branches is reduced to one third (4.2 mm) by a telescope (T;3:1). The transmitted beam from BS2 acts as Stokes beam and the reflected beam acts as probe after frequency doubling to a wavelength of ∼515 nm by passing through a 1.5 mm BBO crystal. A short-pass filter (10SWF-1000-C, Newport) is used to filter out the remaining fundamental wavelength. A combination of a half-wave plate and a polarizing beam splitter is used individually to control the pulse energy for Stokes and probe pulses, which are kept at ∼100 μJ and ∼30 μJ, respectively. A long-pass dichroic mirror DM6 (R:400-633 nm; T: 685-1600 nm) is used to spatially overlap the pump and probe beams. The spatial overlap with the Stokes is achieved by an additional dichroic mirror DM7. Furthermore, the temporal overlap

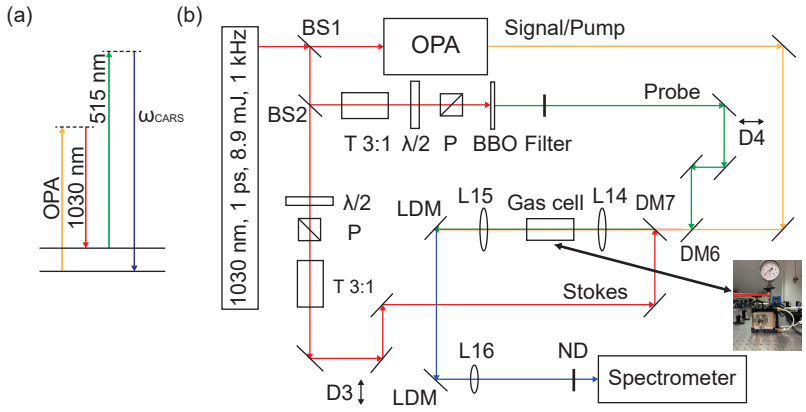


Figure 4.8: Sketch of collinear CARS setup. (a) CARS process with the signal of the OPA acting as pump, the fundamental wavelength of the thin-disk laser at 1030 nm as Stokes and the second harmonic at 515 nm as probe pulses. (b) Collinear CARS setup with the signal of OPA as pump pulse. BS1 and BS2: beam-splitter with split ratio of 50:50. $\lambda/2$: half-wave plate. P: cubic polarizing beam-splitter. L14-16: focusing lens with f = 150 mm, 200 mm and 300 mm, respectively.

between the three beams is adjusted with two motorized delay stages (D3 and D4) in the Stokes and probe beam paths. Finally, all the three beams are focused inside the center of a heated gas chamber (inset of Fig. 4.8 (b), GS05850, Specac Limited, Orpington, UK) by an f = 150 mm focusing lens (L14) and collimated by a subsequent focusing lens (L15: f = 200 mm). The cell chamber volume is ~ 80 ml and the chamber path length is 30 mm with a clear aperture of 11 mm in diameter. The cell chamber windows and cell body can be heated and controlled up to 240 °C. However, the maximum temperature can reach up to 800 °C for the sample itself. The generated CARS signals are filtered out by two long-pass dichroic mirrors (LDM) and coupled into a spectrometer (Shamrock 500i with Marana CMOS camera, Oxford Instruments plc, UK). The acquisition time of the recorded signal is 100 ms.

With this collinear ps-CARS setup, N_2 and CO_2 CARS thermometry will be our focus. With an almost constant spectral width between 17 to 20 cm^{-1}, it is able to resolve the fundamental (2330 cm^{-1}) and first hot band (2300 cm^{-1}) peaks of N_2 and Fermi dyads at

1285 cm^{-1} and 1388 cm^{-1} of CO_2.

4.4 N_2 and CO_2 thermometry

At room temperature, the fundamental peak of N_2 at a Raman shift of 2330 cm^{-1} ($v' = 1 \rightarrow v'' = 0$) is dominant compared to the first hot band at a Raman shift of 2300 cm^{-1} ($v' = 2 \rightarrow v'' = 1$). However, with elevated temperature the decrease of the signal amplitude for the fundamental peak, due to the changes in ro-vibrational population distribution, can be observed. The first hot band typically appears at a temperature of $\sim$ 1000 K [40, 117].

4.4.1 N_2 CARS signals

- **CARS signal of N_2 at atmospheric condition**

  To detect the fundamental peak of N_2, at a Raman shift of 2330 cm^{-1}, the OPA wavelength is tuned to 831.1 nm. Figure 4.9 shows the fundamental peak ($v' = 1 \rightarrow v'' = 0$) with a width of 19 cm^{-1} (FWHM). The energy splitting between the fundamental and the first hot band of N_2 is $\sim$30 cm^{-1}. Thus, it is possible to resolve the first hot band of N_2 at elevated temperatures with the current OPA spectral resolution ($\sim$20 cm^{-1}).

- **The first hot band of N_2 at high temperatures**

  To detect the CARS signal of the first hot band, we tune the OPA wavelength to 833.2 nm. The first hot band can hardly be observed at atmospheric condition. Thus, we increase the pressure of N_2 to 5 bar in the gas chamber to increase the molecular density. Furthermore, the gas chamber is heated up to elevated temperatures. When the gas chamber is heated up to 600 °C, we start to detect the peak of the first hot band ($v' = 2 \rightarrow v'' = 1$) as shown in Fig. 4.10. We note that in this condition,

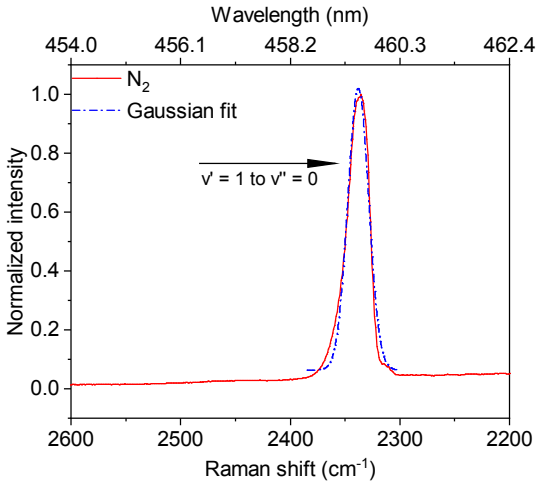


Figure 4.9: The Raman spectrum of N_2 fundamental peak at room temperature. The CARS signal of the fundamental peak is recorded at a probe delay of ∼10 ps.

the fundamental peak is relatively strong comparing with the first hot band. To obtain a sharp and separated spectrum, the output of the OPA and the delay time are optimized. When the gas chamber is heated to the maximum temperature of 720 °C, we could clearly detect the first hot band of N_2 after optimizing the OPA wavelength and the probe delay time (∼1 ps), as shown in Fig. 4.11. From Fig. 4.10 and Fig. 4.11 one can see that there is also the fundamental peak when recording the first hot band peak. At a slightly lower temperature of 600 °C, the fundamental peak is strong compared to that at the temperature of 720 °C. This further proves that at higher temperatures the distribution of molecules across different vibrational states become more spread out.

4.4.2 Temperature determination model

A common approach to determine the temperature from the obtained N_2 CARS signal spectra is to utilize the intensity ratio of the fundamental and the first hot band [118]. In this approach, one uses the integrated signal intensity of fundamental and first hot band.

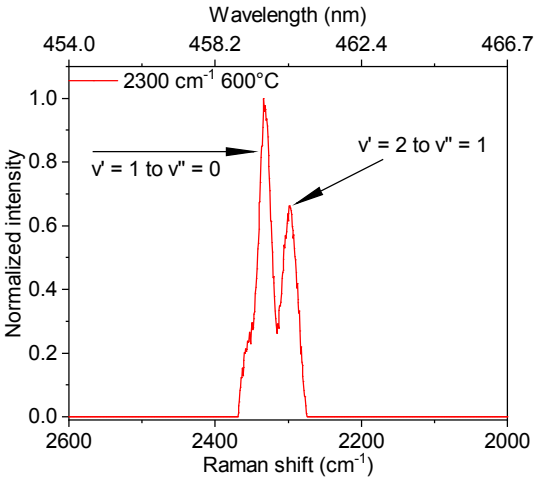


Figure 4.10: The CARS signal of the first hot band of N_2 at a temperature of 600 °C at a pressure of 5 bar. The first hot band N_2 peak is recorded at a probe delay of ∼1 ps.

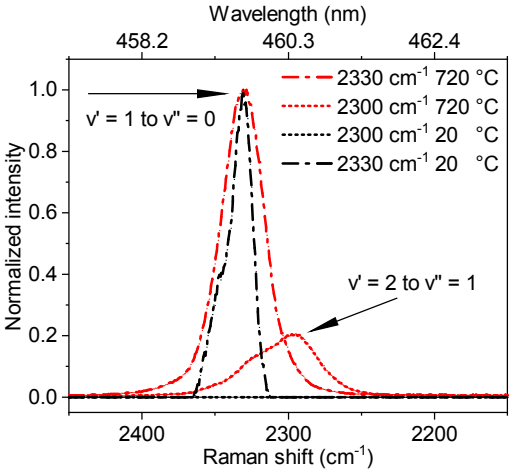


Figure 4.11: The vibrational Raman spectrum of N_2 at various temperatures. The probe delay time is set at ∼1 ps. The gas chamber was filled with N_2 at a pressure of 5 bar.

Another approach is to compare the measured dephasing rate of the fundamental and first hot band of N_2 with the calculated dephasing rate as described in subsection 3.2.5. This dephasing rate depends on frequency spacings between the excited molecular transitions, the temperature and the probing environments. Thus, the temperature information can be extracted from a comparison between the calculated and the experimental probe delay scans of the CARS signal. The simulation is implemented in MATLAB and we assume the probe pulse has no temporal chirp and the pulse duration is 1 ps. The wavelength of the probe pulse is 515.1 nm. The zero delay can be determined by the position where the CARS signal is maximal. In the simulation, the CARS signal at different probe delay time can be calculated according to Equation 3.46. The step size of the temporal delay scan is 100 fs. Then one can get the dephasing rate at a certain temperature from the integrated CARS signals over the spectral range for each separately resolved N_2 CARS peaks. The experimental CARS signals are recorded at different probe delays. Then the experimental dephasing rate can be obtained from the corresponding integrated CARS signals. In order to determine how good the fit, average standard deviation is utilized between the experimental N_2 dephasing curves and the simulated data.

- **Intensity ratio of N_2 peaks**

  Figure 4.11 depicts the CARS signals of the fundamental and the first hot band of N_2 at a probe delay of $\sim$1 ps at 20 °C (black lines) and 720 °C (red lines). The dash dotted line and the dotted line are the recorded CARS signals of the fundamental ($v' = 1 \rightarrow v'' = 0$) and the first hot band ($v' = 2 \rightarrow v'' = 1$), respectively. At higher temperatures, molecules have higher kinetic energy, leading to increased vibrational and rotational motion. This increased motion results in a broader distribution of rovibrational states, meaning that a greater range of energy levels is populated. Thus, the distribution of molecules across different vibrational states become more spread out, leading to a broader and more pronounced spectral peak as shown in Fig. 4.11.

  A typical approach to derive the temperature from the spectra is to determine the

intensity ratio of the fundamental and the first hot band. In Fig. 4.11, the intensity ratio of the first hot band and fundamental peak is ~ 0.2, which is in good agreement with a recent literature value at $\sim$ 1000 K ($\sim$ 727 °C) [118].

- **Dephasing rate of the fundamental peak**

As an alternative option for intensity ratio of N_2 peaks, CARS signal decay due to the dephasing of the initial Raman coherence is also utilized to extract the temperature information as described in subsection 3.2.3. In this study, the CARS spectra at each delay scan are recorded. Then the intensities of the CARS signals are integrated over the spectral range for each separately resolved N_2 CARS peak. The step size of the temporal delay scan is 100 fs. The temperature step size is 1 °C. The temperature is extracted by fitting the experimental integrated CARS signals over the spectral range of $\sim$ 2300 - 2370 cm^{-1} at different delays with the calculated signals from Equation 3.46. Figure 4.12 summarizes experimental initial depahsing rates of the fundamental peak of N_2 measured at various temperatures. In order to determine how good the fit for the experimental and simulated dephasing rates, one can calculate the deviation of the simulated (lines) and the experimental (dots) CARS signal intensity of the fundamental peak of N_2 across different delay points. The best-fit simulated probe-delay scans with smallest deviation are used to extract temperatures from experimental scans. At room temperature, 240 °C, 600 °C and 720 °C, the average standard deviation are 4 %, 1 %, 2 % and 2 %, respectively. However, higher temperature is of great interest in the combustion diagnostics. With increasing temperature up to 720 °C , the accuracy of temperature determination is within 4 % (720 °C vs 747 °C).

- **Dephasing rate of the first hot band peak**

Within this study, we also recorded the time resolved CARS signals of the first hot

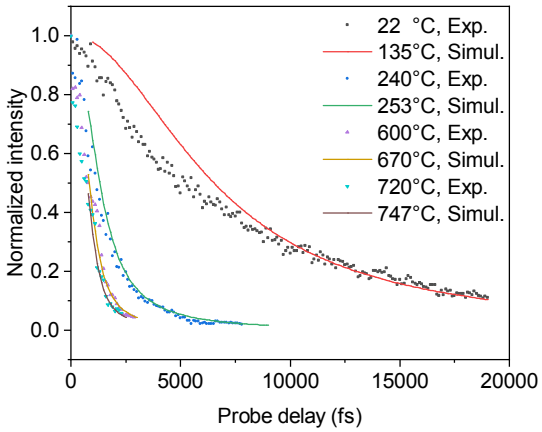


Figure 4.12: The initial dephasing rate of N_2 at a Raman shift of 2330 cm^{-1} at various temperatures with the best fitting curves.

band at temperatures of 600 °C and 720 °C at different delay times. The temperature is extracted by fitting the experimental integrated CARS signals over the spectral range of $\sim$ 2270 - 2315 cm^{-1} at different delays with the calculated signals, as shown in Fig. 4.13. The CARS signal intensities are normalized with the peak point at each temperature. Figure 4.13 shows that within $\sim$ 1 ps the CARS signal intensity of the first hot band at temperatures of 600 °C and 720 °C decreases fast, which may be the contribution of nonresonant background. From a delay time of 1 to 2 ps the experimental depahsing rate is in good agreement with the simulated data. Thus in this study, a probe pulse delay of $\sim$1 - 2 ps is chosen to avoid contributions from the nonresonant background. At higher temperature of 720 °C, the accuracy of determined temperature is $\sim$ 2 % (720 °C vs 737 °C), while the accuracy is $\sim$7% at a temperature of 600 °C (600 °C vs 640 °C).

In this section three ways (intensity ratio of N_2 peaks and the dephasing rate of the fundamental and first hot band peaks) are used to determine the gas temperature. Kiefer et. al. [118] illustrate the calibration plot of the extracted temperatures as a function of the intensity ratio of the N_2 peaks. When using the intensity ratio of the N_2 peaks to extract

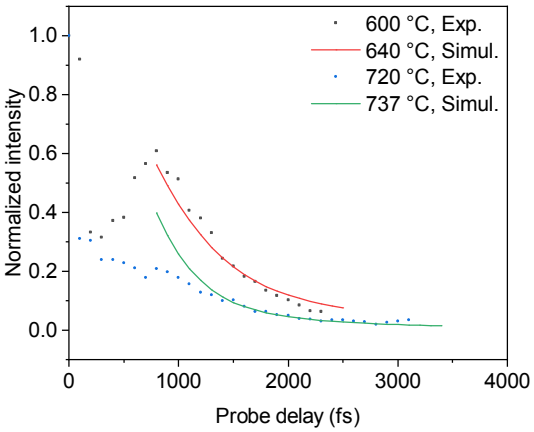


Figure 4.13: Experimental and the best-fit time-resolved CARS signals of the first hot band at various temperatures.

the temperature, it is in good agreement with the values (0.2) of the above study. For the dephasing rate of N_2 peaks, the temperature determination accuracy with the first hot band is better ($\sim 2\ \%$ vs $\sim 4\ \%$ for the fundamental peak) compared to that of the fundamental peak at higher temperature of 720 °C.

4.4.3 CO_2 thermometry

CO_2 CARS is much more complicated than that of diatomic molecules [119, 120]. Since CO_2 is a linear symmetric triatomic molecule, it has four vibrational modes: the symmetric stretching mode (quantum number v_1), the doubly degenerate bending mode (v_2) and the antisymmetric stretching mode (v_3). In the doubly degenerate bending mode v_2, one needs an extra angular momentum quantum number l to specify the quantum state. The unperturbed vibrational frequency $v_1 \approx 2v_2$ leads to the so-called Fermi-resonance effects. The perturbed levels are normally named Fermi polyads. Fermi resonance yields mainly four vibrational transitions (1388 cm^{-1} and 1285 cm^{-1} for the first Fermi polyads, 1409 cm^{-1} and 1265 cm^{-1} for the second Fermi polayads). When the temperature increases, the peak intensities for the second Fermi polyads increase compared to the first Fermi polyads due to

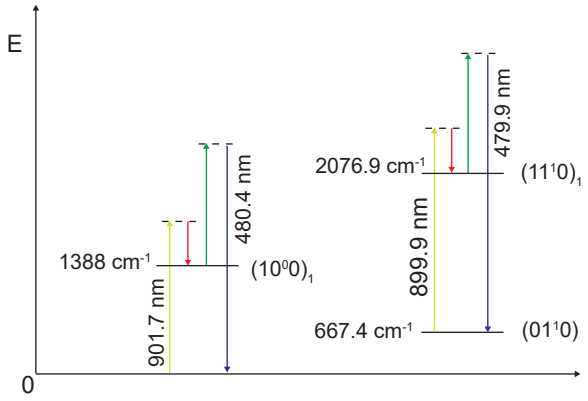


Figure 4.14: Sketch of four-wave mixing process for the fundamental and first hot band transitions of CO_2.

the molecular population change. Therefore, one can rely on either 1388 cm^{-1}/1409 cm^{-1} or 1285 cm^{-1}/1265 cm^{-1} peak ratios to extract the temperature. However, in this study the vibrational transitions of CO_2 with Raman shifts of 1388 cm^{-1} and 1409 cm^{-1} are mainly considered for gas phase temperature measurements due to the stronger signal strength for low temperatures (e.g. 295 K).

Due to the relative low energy of the first excited bending mode (0,1^1,0) as shown in Fig. 4.14, it is already populated at room temperature, which enables measurements of lower temperatures compared to N_2. Figure 4.14 shows the vibrational energy level diagram of CO_2 in the CARS. Here, I take the energy level of 1388 cm^{-1} as an example to show how the CARS works. To generate the CARS signal for energy level of 1388 cm^{-1}, the OPA signal was tuned to wavelength of 901.7 nm as pump (in yellow), the fundamental pulses at 1030 nm as Stokes (in red), and the SHG at 515 nm as probe (in green). The generated CARS signal is detected at wavelength of 480.4 nm (in blue).

To generate the corresponding CARS signals of CO_2 at Raman shifts of 1388 cm^{-1} and 1409 cm^{-1}, we tune the OPA signal to wavelengths of 901.7 nm and 899.9 nm, respectively. To avoid nonresonant contributions, the optimized spectra are recorded at a probe delay time of 2 ps. The CARS signals of these two peaks are recorded at room temperature,

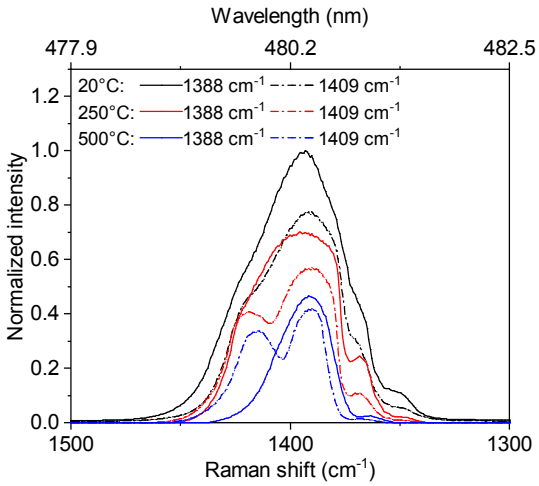


Figure 4.15: CARS signals of CO_2 with a pressure of 3 bar at different temperatures. Measured CARS signals of CO_2 at Raman shifts of 1388 cm^{-1} and 1409 cm^{-1} at temperatures of 20 °C, 200 °C and 500 °C are shown.

250 °C and 500 °C with a pressure of 3 bar in the cell chamber as shown in Fig. 4.15. At room temperature we can hardly observe the peak for the Raman shift at 1409 cm^{-1} due to the strong signal strength at the Raman shift of 1388 cm^{-1}. With increasing temperature the small peak of the CARS signal at 1409 cm^{-1} becomes stronger due to the higher population of the first excited bending mode $(0,1^1,0)$ [121]. At a temperature of 500 °C, the intensity ratio between the two peaks is ∼0.7 (blue lines in Fig. 4.15), whereas we measured ∼0.6 in a previous study, using ultrabroadband excitation and a slightly larger probe pulse duration of ∼1.5 ps ([8]). We attribute this discrepancy to the large overlap of the CARS-peaks at 1388 and 1409 cm^{-1}, whereas the peaks are clearly separated for N_2 (Fig. 4.11). Yet, a recent study on self-phase modulation (SPM) induced by 60 fs pulses shows that this effect is considerably larger for CO_2 than for N_2 [122], but longer pulse durations should reduce this effect [123, 124]. Thus, our results clearly show that the choice of the pulse duration around 1 ps is crucial and further experimental and numerical investigations are required on the influence of the pulse energy, pulse duration and focusing conditions on the CARS spectrum, especially for CO_2.

4.5 Conclusion

In summary, a customized ps-OPA system is pumped by a commercial thin-disk based 1 kHz laser, which provides a pulse duration of $\sim$ 1 ps across the full tuning range 700 - 950 nm. As of our knowledge, for the first time we demonstrated the $\sim$ 1 ps CARS setup with a tunable $\sim$ 1 ps OPA system. With the output of the OPA as pump, the fundamental wavelength 1030 nm as Stokes and the second harmonic 515 nm as probe, we detected the CARS signals of N_2 and CO_2 at high temperatures. The ps-CARS setup provides sufficient spectral resolution (17 to 20 cm^{-1}) to distinguish the fundamental and the first hot band of N_2 peaks. In N_2 ps-CARS for temperature determination, three different ways have been used in this study for thermometry. For the dephasing rate of N_2 peaks, the temperature determination accuracy with the first hot band is better ($\sim$ 2 $\%$ vs $\sim$ 4 $\%$ for the fundamental peak) at higher temperatures of 720 °C. The intensity ratio between the CO_2 peaks deviates from our previous study (0.7 vs 0.6 [8]). We attribute this deviation to the large spectral overlap of the CO_2 CARS signals at 1388 cm^{-1} and 1409 cm^{-1}. In order to optimize the CARS signals of CO_2, one needs to enhance the signal strength by increasing the molecular density and minimize the SPM effects by using lower pulse energies.

Chapter 5

CARS based on ps filamentation

5.1 Overview

In this chapter, we aim to study the spectral broadening in IR filamentation in air induced by $\sim$ 1 ps pulses. We investigate this in dependence of pulse energies up to 60 mJ with different focal lengths up to 4 m. Ultimately, the spectral broadening in the filament is used as pump/Stokes beams in a CARS setup to not only detect N_2 and O_2 in air but also molecules with larger Raman shifts such as CH_4. In order to determine the concentration of N_2 and O_2 in air, we simulated and measured the CARS signal peak ratio at different probe delay time at room temperature. Finally, the influence of the insertion of optical windows on the CARS signals in air is also investigated, which is of great relevance for the industrial applications.

5.2 Experimental setup

A thin-disk regenerative amplifier (Dira 500-10, Trumpf Scientific Lasers GmbH + Co. KG, Germany) is used as the pump source, providing a pulse duration of $\sim$ 1 ps at a central wavelength of 1030 nm.

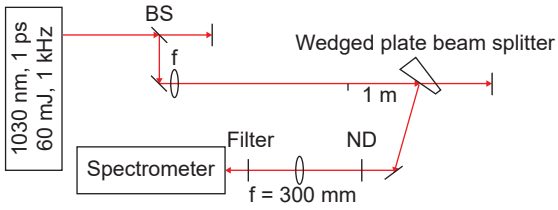


Figure 5.1: Scheme of the setup to measure the broadened spectra after a focusing lens. BS: Beam splitter with a reflectivity (R): transmission (T) = 90:10. ND: neutral density filter. The position of the wedged plate beam splitter is at ∼1 m after the filament in the beam propagation direction. Filter: two types of short-pass filters to block the central wavelength at 1030 nm.

5.2.1 Spectral broadening investigation setup

A scheme of the experimental setup for investigating the broadened spectrum is shown in Fig. 5.1. The laser beam has a linear polarization and a Gaussian beam diameter of ∼12.7 mm ($1/e^2$). The laser source can provide a maximum pulse energy of 60 mJ at a repetition rate of 1 kHz. 90% of the laser pulses are reflected by a beam splitter BS (R:T = 90:10) and then focused with focal lengths ranging from 2 to 4 m to generate filamentation. The remaining 10% of the laser pulses transmits the BS and is used to generate second harmonic at ∼515 nm as the probe beam in the CARS configuration. ∼1 m downstream from the filament the beam is attenuated by a wedged plate, a neutral density (ND) filter and two short-pass filters before being coupled into a spectrometer (Shamrock 500i with Marana CMOS camera, Oxford Instruments plc, UK) where the signal is acquired over 100 ms (∼ 100 laser pulses). In order to block the central wavelength of the pump beam ($\lambda = 1030$ nm), a short-pass filter (10SWF-1000-C, Newport) to detect the spectral range from 800 nm to 980 nm and a long-pass filter (1050 nm, high performance long-pass filter, OD 4.0, Edmund Optics) to detect the spectral range from 1080 to 1200 nm are used.

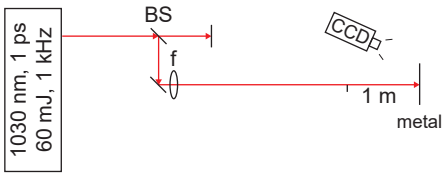


Figure 5.2: Scheme of the setup to measure the number of filaments with a CCD camera. The exposure time of the CCD is set at 1/1250 s to ensure the single shot acquisition.

5.2.2 Single shot filaments setup

In addition to the broadened spectra induced by filamentation, we further investigated the number of filaments induced in a single shot. To evaluate the number of filaments, the beam is recorded with a CCD camera on an alternative metal plate, which is positioned ∼4 m behind the focusing lens (shown in Fig. 5.2). The exposure time is 1/1250 s to allow single shot acquisition. The maximum peak power in this study is 60 GW, which is far beyond the critical power 5 GW in air.

5.2.3 Filamentation-based CARS setup

To investigate the CARS signals in air, the broadened spectrum induced by the filamentation is utilized as pump and Stokes and the second harmonic at ∼515 nm as the probe beam. The optical layout for the pump-probe CARS setup is shown in Fig. 5.3. The filament is generated by focusing 90% of the laser pulses into the atmospheric air with a focusing lens. The inset in Fig. 5.3 shows the estimation for the length of the filament, which is ∼80 cm at a pulse energy of 34 mJ with an f = 3 m focusing lens. To adapt the beam size to the size of the BBO crystal (6*6*1.5 mm), the probe beam size is reduced with a telescope (3:1). In order to control the power of the probe beam, a half-wave plate and a cubic polarizing beam splitter are used in front of a 1.5 mm BBO crystal.

Furthermore, the probe beam passes through a short-pass filter, filtering out the remaining beam at a wavelength of 1030 nm and is delayed by a motorized translation stage. The

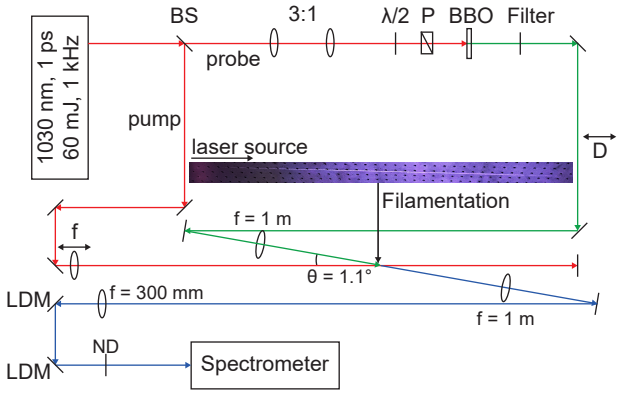


Figure 5.3: Optical layout of filament-based CARS. Pump: 90% of the laser source focused by a focusing lens to achieve filamentation. Probe: 10% of the laser beam after frequency doubling to a wavelength of ∼515 nm. λ/2: half-wave plate. P: cubic polarizing beam splitter. BBO: 6*6*1.5 mm. Filter: short-pass filter. D: motorized delay stage. LDM: long-pass dichroic mirror. The inset shows a photograph of the filament.

pulse energy of the probe pulse is kept at ∼300 μJ. To fulfill phase matching with a nearly collinear CARS setup, the probe beam is focused using an f = 1 m focusing lens at a small angle ($\theta = 1.1°$) with respect to the pump pulse. To optimize the spatial overlap of the pump and probe pulses, the 3 m focusing lens is placed on a 20 cm long translation stage. After the collimating lens with a focal length of f = 1 m, the generated CARS signals are reflected by two long-pass dichroic mirrors (DMLP490, Thorlabs), before being coupled into the spectrometer with an f = 300 mm cylindrical lens.

5.3 Spectral properties during filamentation

- **Initial spectra**

  The initial spectra of pump (red line) and probe (blue line) pulses with Gaussian fits (dashed lines) are shown in Fig. 5.4. The spectral widths of the pump and probe beams are 1.8 nm (∼ 17 cm^{-1}) and 1.3 nm (∼ 49 cm^{-1}), and the corresponding center wavelength are 1030.7 nm and 515.1 nm, respectively. The probe spectrum is

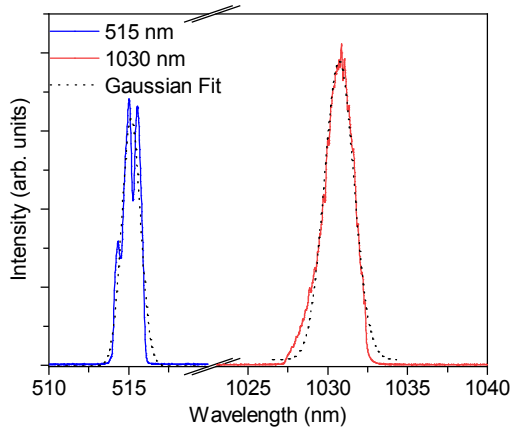


Figure 5.4: Initial spectra of the pump and probe pulses. The Gaussian fits (dashed lines) of the pump (red line) and probe (blue line) are centered at 1030.7 nm and 515.1 nm, respectively.

fractioned after passing through the BBO crystal, which is primarily due to nonlinear optical processes such as phase matching. Phase matching can lead to efficient frequency conversion at specific wavelengths, fractioning the probe spectrum. The influence of the spectrum shape on the experimental results will be discussed in the CARS spectrum section.

- **Broadened spectra**

  To systematically investigate the broadened spectra after the filament, different focusing conditions and pulse energies are considered in this study. For an f = 2 m focusing lens, the spectrum induced by filamentation is getting more broadened with the increasing laser pulse energy E_{pulse} up to 50 mJ. For an f = 3 m focusing lens, the broadened spectra for different pulse energies are shown in Fig. 5.5. The largest spectral width of ∼280 nm with visible spectral intensities between 850 nm (spectral intensity of -21 dB) to 1130 nm (spectral intensity of -22 dB) occurs at a pulse energy of 34 mJ, corresponding to a Raman shift of ∼2900 cm^{-1}. This should be broad enough to excite the ro-vibrational Raman transitions in air and potentially even CH_4 (∼2917 cm^{-1}), which contradicts the first results of Houard et

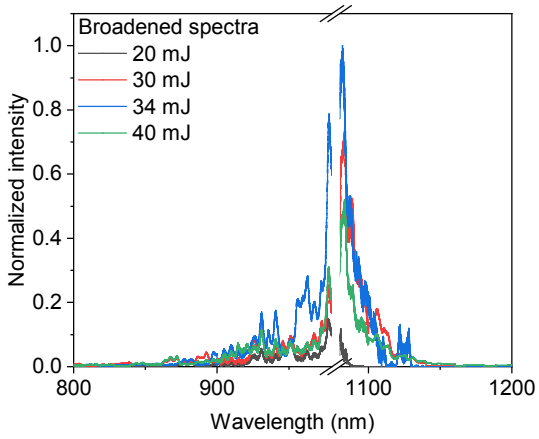


Figure 5.5: Filament-induced spectra with an f = 3 m focusing lens for different pulse energies. The spectral width peaks at a pulse energy of 34 mJ. The spectra are normalized with the peak point at a pulse energy of 34 mJ.

al. [50] with only ∼25 nm (spectral intensity of -20 dB) due to less efficient spectral broadening after filamentation. With even higher pulse energies than 34 mJ, the recorded broadened spectrum is narrower. So in the current focusing condition, the broadened spectrum peaks at a pulse energy of 34 mJ. Similarly, these spectral widths are determined for an f = 2 m and f = 4 m lens. Figure 5.6 displays the spectra at different pulse energies for an f = 4 m focusing lens. The spectra are normalized with the peak point at a pulse energy of 34 mJ. One can notice that the largest broadened spectrum is also recorded at a pulse energy of 34 mJ. Compared with the largest broadened spectra at different optimized focusing conditions (Fig. 5.7), the spectral broadening is negligible for f = 2 m even for the maximum pulse energy of 50 mJ. For f = 3 m and f = 4 m, the spectral broadening peaks at E_{pulse} = 34 mJ and is significantly larger for f = 4 m. This can be understood according to Equation 3.53. With longer focusing lens f = 4 m, the nonlinear propagation length is increased. Thus, the spectral broadening is stronger according to Equation 3.56.

- **Number of filaments**

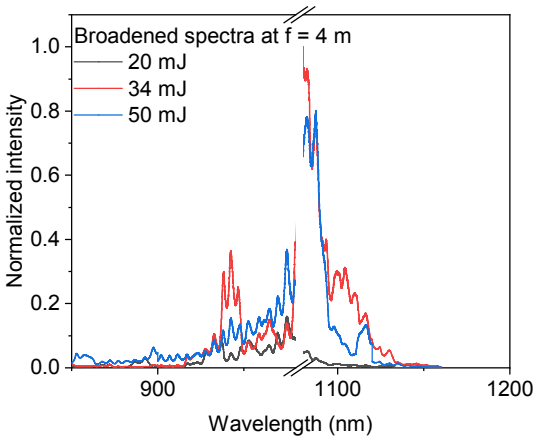


Figure 5.6: Broadened spectra for f = 4 m focusing lens at different pulse energies. The spectral width peaks at a pulse energy of 34 mJ.

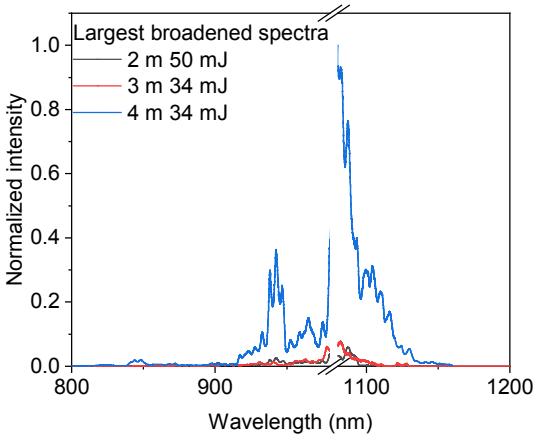


Figure 5.7: Most broadened spectra for f = 2 m, 3 m, 4 m. The spectra are normalized with the peak point at a pulse energy of 34 mJ for f = 4 m focusing lens. The spectral broadening is negligible for f = 2 m compared to the focal length of 3 and 4 m.

The generation of single and multiple filamentation has been discussed in section 3.4.1. Multi-filamentation is caused by inhomogenities of the initial beam profile, especially if the laser power is far above the critical power for self-focusing. The critical power in air for self-focusing is calculated with the Equation 3.48, which is ∼5 - 10 GW in our case [86, 87, 125, 126]. In this study, the number of the filaments is investigated on a metal surface, which is positioned at ∼1 m behind the filamentation. The maximum laser peak power used in this study is 60 GW, which is about one order of magnitude above the P_{cr}. Figure 5.8 depicts single-shot images of white-light from the filament. With increasing pulse energies for f = 2 m (Fig. 5.8 a, b), only a single filament is observed. For f = 3 m, at low (E_{pulse} = 20 mJ, Fig. 5.8 c) and high (E_{pulse} = 40 mJ, 50 mJ, Fig. 5.8 f, g) pulse energies, a single filament is observed, while ∼3 filaments occur at pulse energies of 30-34 mJ (Fig. 5.8 d, e). In contrast, with an f = 4 m focusing lens, at low (E_{pulse} = 20 mJ, Fig. 5.8 h) and high (E_{pulse} = 40 mJ, Fig. 5.8 k) pulse energies, 2 filaments are observed. The amount of the filaments peaks at a pulse energy of 30-34 mJ, which is 3 filaments.

The broadened spectra under the conditions of different focusing lens (f = 2, 3 and 4 m) are obtained by the experimental setup Fig. 5.1. The results illustrated here indicate that focusing with longer focal length (f = 4 m) will further broaden the spectrum and improve the CARS signal. However, the spatial requirements can be challenging in a laboratory frame. Thus, in a proof-of-principle experiment, a focal length of 3 m is chosen due to sufficient spectral broadening for Raman excitation in air. Therefore, the CARS signals beyond f = 3 m are not investigated here and are the subject for future investigations.

Figure 5.9 shows the broadened spectra generated by filamentation with a 3 m focusing lens at a pulse energy of 60 mJ. One can also see that the two spectra fluctuate, which will also lead to strong fluctuations of the CARS signals.

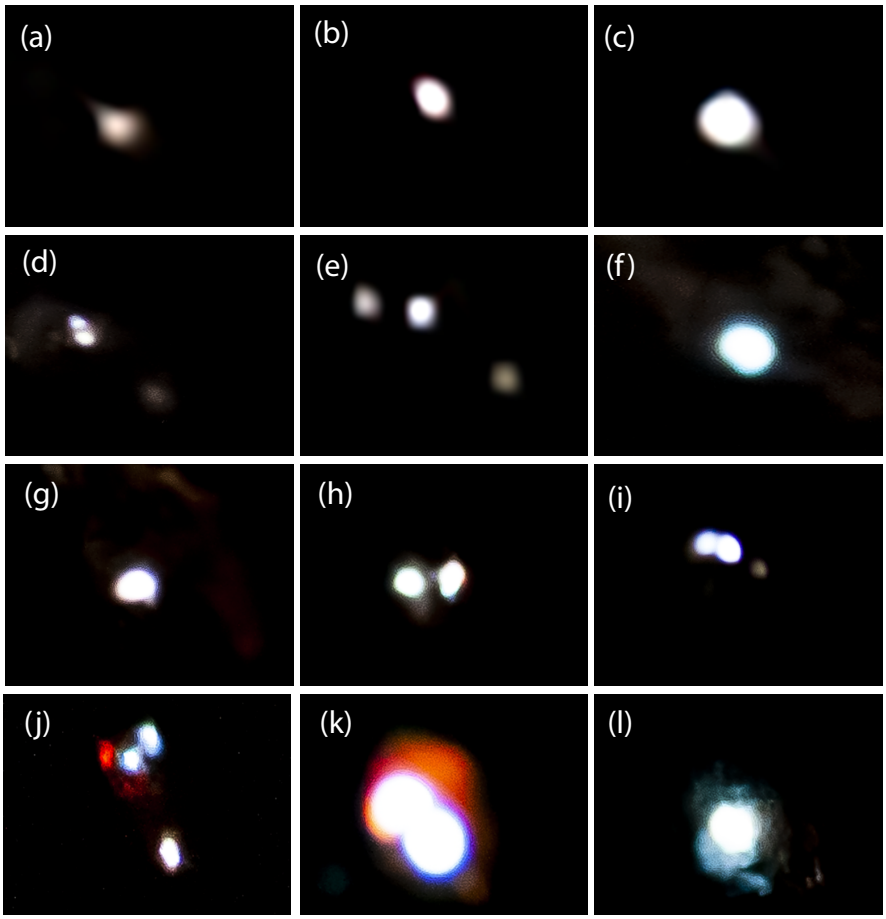


Figure 5.8: Images of single shot filaments on a metal plate at various energies using different focal lengths. f = 2 m, E_{pulse}: (a) 20 mJ, (b) 50 mJ. f = 3 m, E_{pulse}: (c) 20 mJ, (d) 30 mJ, (e) 34 mJ, (f) 40 mJ, (g) 50 mJ. f = 4 m, E_{pulse}: (h) 20 mJ, (i) 30 mJ, (j) 34 mJ, (k) 40 mJ, (l) 50 mJ

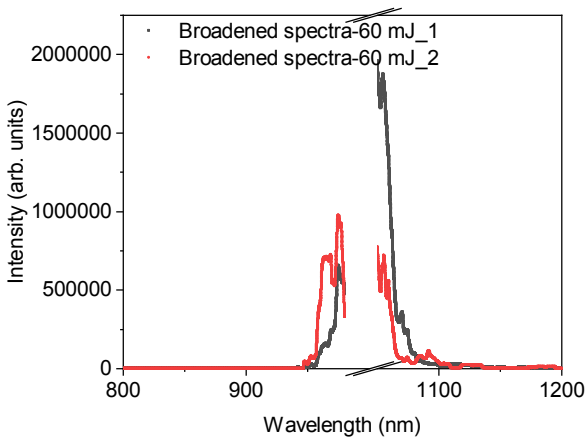


Figure 5.9: Fluctuation of the broadened spectra at a pulse energy of 60 mJ. The acquisition time of the recorded spectra is 100 ms.

5.4 CARS signals and concentration determination

5.4.1 CARS signals of N_2 and O_2

To perform ps-filamentation based CARS, the broadened spectrum after the filament has to cover the range of both the pump and the Stokes beam. Here, with a focal length of 3 m, the filamentation based CARS signals of air for different pulse energies are investigated. For this we gradually increase the laser pulse energy E_{pulse} while the probe pulse at 515 nm is kept at 300 μJ.

In order to avoid the non-resonant background, the probe delay time is set at $\sim$1.5 ps to detect the CARS signals in air. At a pulse energy of 26 mJ the CARS signal of O_2 is first detected due to the smaller Raman shift ($\sim$1556 cm^{-1}) compared to N_2 ($\sim$2330 cm^{-1}). Increasing the pulse energy further (E_{pulse} = 27 mJ), the CARS signal of N_2 is also visible. Subsequent increasing of the pulse energy increases the respective intensity of N_2 and O_2 CARS signals as shown in Fig. 5.10. The CARS signals in Fig. 5.10 are normalized with the peak point of the O_2 CARS signal at a pulse energy of 34 mJ. In correspondence to the spectral broadening investigations in Fig. 5.5, the CARS signals of N_2 and O_2 reach

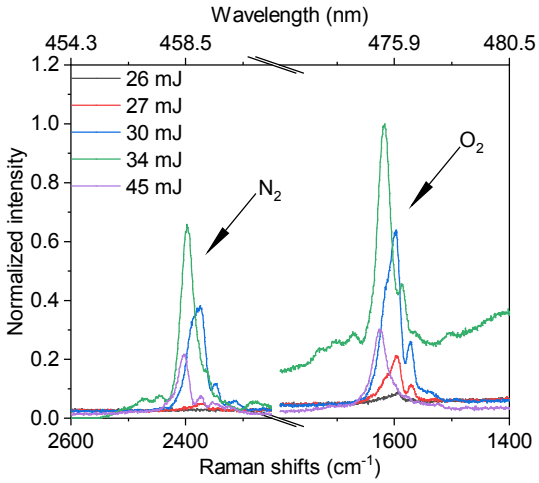


Figure 5.10: CARS spectrum in air for different pulse energies with an f = 3 m focusing lens. The CARS signals in air peak at a pulse energy of 34 mJ.

a maximum at $E_{pulse} = 34$ mJ. With an even higher pulse energy (e.g. 45 mJ) the CARS signals of N_2 and O_2 simultaneously decrease, while both signals are blue shifted. The blue shift may be caused by amplified stimulated emission (ASE) and post-pulses [127–130], but a systematic analysis of this effect is beyond the scope of this study. The singal-to-noise ratio for N_2 is ~ 30, which is determined by the ratio of the peak intensity and the average noise at a negative probe pulse delay.

5.4.2 Concentration determination

In this section the focus will be directed to the model of concentration determination. Lucht et al. [3] have already shown that the gas phase temperature and concentration information can be extracted from the magnitude and delay of the initial Raman coherence using time-resolved fs CARS.

One problem here is that the broadened spectrum is highly depending on the initial conditions and is thus fluctuating as shown in Fig. 5.9. Therefore, we will analyze the dependence of the relative signals for N_2 and O_2 on the delay between pump/Stokes and the probe beam. The probe intensity $I_{Pr}(t-\tau)$ is assumed to have a Gaussian pulse shape.

The zero delay can be determined by the position where the CARS signal is maximal.

First, we start to simulate the peak ratio in air. In the simulation, the Raman cross sections (4.922E-35 m^2/sr for N_2 and 6.079E-35 m^2/sr for O_2 [77]) and atmospheric concentrations for $N_2 : O_2$ (80 : 20) are used. The pulse duration of the probe pulse is 1 ps. More details related to the CARS signal calculation can be found in section 3.2.5. As we do not know the corresponding laser intensities for the pump and Stokes beams, we consider them at first to be constant. Figure 5.11 (a) shows the simulated CARS signals of N_2 and O_2 at a zero probe delay. Here, the peak ratio of N_2/O_2, $\sim$19:1, is consistent with the published ratio of $\sim$17:1 [46]. However, it is obvious from Fig. 5.10 that the experimental ratio is completely different, which is due to a different excitation efficiency.

Figure 5.11 (b) shows the simulated time dependence of the normalized CARS signals for N_2 and O_2. We compared the CARS signal delay scan to 10 ps with the literature [3, 46], which matches well. The relative peak ratio between N_2 and O_2 for different delay times is shown in Fig. 5.12. It slightly increases with the time delay. This increase could be observed from Fig. 5.11 (b). The CARS signal of N_2 decreases slower than O_2, which can be attributed to differences of the dephasing of the Raman coherence. Additionally, variations in the excitation efficiency and Raman cross sections for N_2 and O_2 might contribute to this trend.

In order to compare the temporal evolution to the experimental values, for each time delay point five spectra are recorded, background corrected and averaged to get the average peak ratio as shown in Fig. 5.13. The error bar shows the standard deviation of the peak ratio across different delay points, which is quite high due to strong intensity variations in the broadened spectrum. The average standard deviation amounts to 54 $\%$. Despite the significantly lower peak ratio than expected, the general trend as a function of delay is similar. However, one can see that there is still large fluctuations in the experiment (in red). From the simulation one expects no oscillation because we assumed the uniform excitation efficiency and stable broadened spectra. The average peak ratio of N_2 and O_2 tends to increase with the delay despite fluctuations. The average value of peak ratio N_2/O_2 for

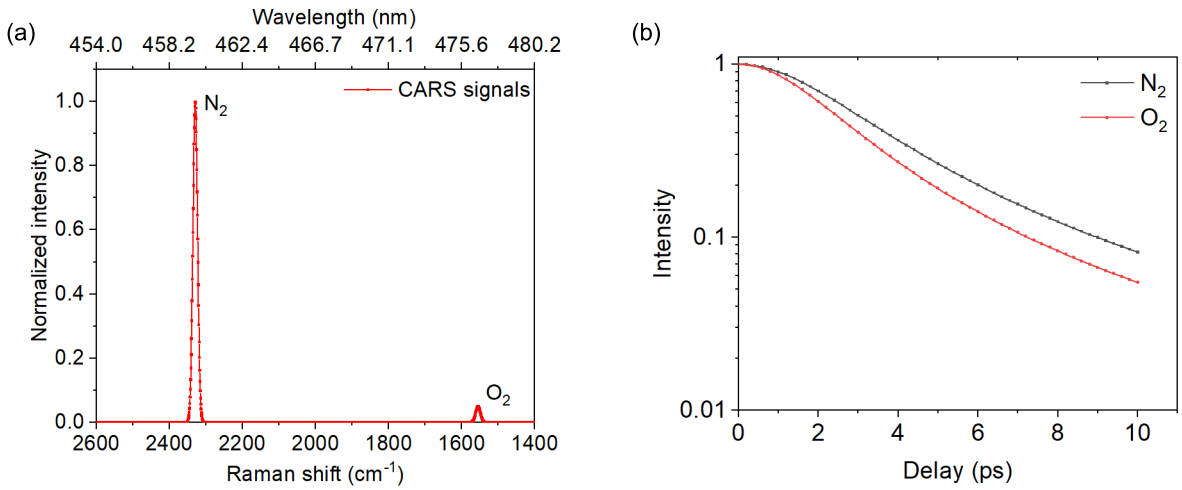


Figure 5.11: Simulated CARS spectra and the delay scan of N_2 and O_2 signals. (a) The simulated CARS signals of N_2 and O_2 at a zero probe delay. (b) The delay scan of the CARS signals for N_2 and O_2 at room temperature.

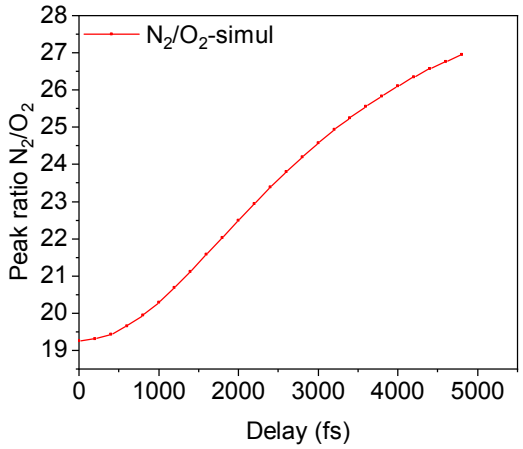


Figure 5.12: Simulated peak ratio of N_2 and O_2 CARS signals at different probe delay time. The peak ratio N_2/O_2 slightly increases with the time delay.

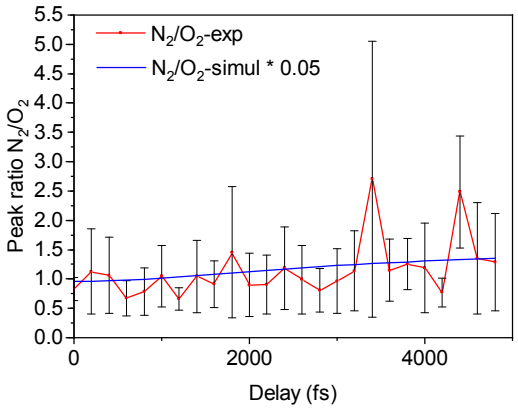


Figure 5.13: The experimental average peak ratio of N_2 and O_2. The average value of peak ratio N_2/O_2 for experiment/simulation is 0.05.

experiment/simulation is 0.05 evaluated with the Fig. 5.12 and Fig. 5.13. After applying the appropriate coefficient (0.05) for the simulation, the simulated data (in blue) fits well with the experimental data. In order to determine how good the fit of the experimental data to the simulation in Fig. 5.13 is, one can calculate the deviation of the simulated and experimental peak ratio across different delay points. The average standard deviation for the simulated and experimental delay scan fit amounts to 14 %. Thus, with this limited quality of delay scan fit (14 %), we could determine concentrations taking this measurement as a reference.

So far we assumed equal excitation efficiencies. Here, we need to evaluate the experimental excitation efficiency and the gas concentration. Based on the Equations of 3.26 and 3.27, the peak ratio of N_2 and O_2 is proportional to the square of the ratio of concentration, Raman cross section and excitation efficiency as shown below [11]:

$$Peak\ ratio \propto (\frac{C_{N_2} * \sigma_{N_2} * \eta_{N_2}}{C_{O_2} * \sigma_{O_2} * \eta_{O_2}})^2 \tag{5.1}$$

From the simulated and experimental peak ratio of N_2 and O_2, one can estimate the experimental excitation efficiency:

$$\frac{\eta_{N_2}}{\eta_{O_2}} = \sqrt{\frac{(peak\ ratio)_{ex}}{(peak\ ratio)_{simul}}} \tag{5.2}$$

Thus, one can calculate the excitation efficiency for each delay point with the corresponding peak ratio and the average value of $\frac{(peak\ ratio)_{ex}}{(peak\ ratio)_{simul}} = 0.05$. So the average experimental excitation efficiency $\frac{\eta_{N_2}}{\eta_{O_2}} = 0.22$, which includes the information for the laser intensities for the pump and Stokes beams. With this average experimental excitation efficiency we could evaluate other gas concentrations.

Despite the high average standard deviation of the measured data of 54 $\%$ the fit to the delay scan showed an improved error in the range of only 14 $\%$. As described above, the concentration ratio is proportional to the peak ratio, thus, this will lead to an error of 7 $\%$ in the concentration determination. Nevertheless, this requires measuring also the delay scan. To improve the accuracy further, one has to tackle the problem of the strong fluctuations of the filament spectrum. Recently, we used referencing of the resonant signal in pure argon to improve the accuracy [131], however, this will require to expose the argon to the same spectrum and will fail if the shot to shot fluctuations are high. One alternative might be the simultaneous recording of the filamentation spectra and the CARS signals, which may provide a more reliable method for analysis. However, this will also put additional constraints to remote sensing. Therefore, further experiments are required to stabilize the CARS signals and mitigate the spectral fluctuation caused by filamentation.

5.4.3 CARS signal of CH_4

To further investigate the limit of the broadened spectrum after filamentation, CARS signals of other molecules with even higher Raman shifts (especially CH_4 $\sim$2917 cm^{-1} since CH_4 is an important species in many combustion scenarios) are tested. The normal vibrational modes of methane include four modes: v_1 mode (2917 cm^{-1}), v_2 mode (1533 cm^{-1}), v_3 mode (3019 cm^{-1}), v_4 mode (1311 cm^{-1}). The normal frequency of the stretch modes is roughly double than the bending modes ($v_1 \approx v_3 \approx 2\ v_2 \approx 2\ v_4$). To avoid laser-induced damage, the beam was focused into a cell without side windows. The beam focus within the gas cell was set close to the gas inlet for the maximum CARS signal. The CH_4 flow was at an average flow rate of $\sim$1.6 ml/s. Using the most broadened spectrum at a pulse energy

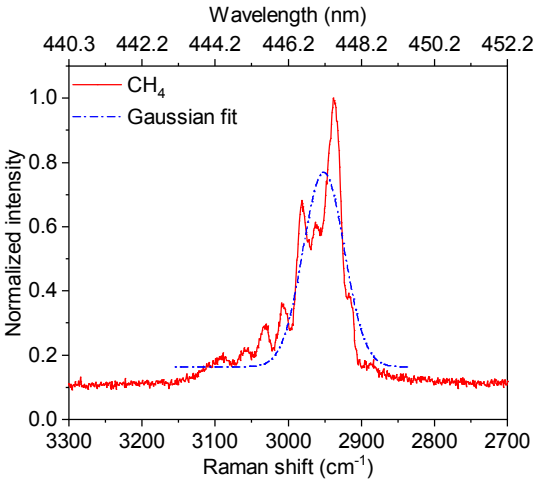


Figure 5.14: CARS signal of CH_4 at a pulse energy of 34 mJ. At the largest broadened spectrum, the CARS signal of CH_4 is detected at 447.2 nm.

of 34 mJ for Raman excitation, a strong CARS signal of CH_4 at ∼447.2 nm is detected as shown in Figure 5.14. The spectral width of CH_4 ($\sim$ 56 cm^{-1}) is rather broad compared to N_2 (∼32 cm^{-1}). Due to the larger Raman cross section (3.677E-35 m^2/sr for CH_4 [77]) and its stretching vibrational modes (v_1 and v_3), CH_4 generally exhibits a larger CARS response compared to molecules like N_2 and O_2. In a recent study, Mazza et al. [132] showed similar phenomenon on the ro-vibrational v_2 mode spectrum at the Raman shift of 1533 cm^{-1}. The signal of ro-vibrational O_2 (1556 cm^{-1}) may also contribute to this broad signal strength. Another reason in our study may be the initial fractionated probe spectrum and the lower signal-to-noise ratio of CH_4 compared to N_2 and O_2. And the Raman shift of CH_4 is at the edge of the broadended excitation spectrum (2900 cm^{-1}, Fig. 5.5). The Gaussian fit is centered at a Raman shift of 2951 cm^{-1}, which is blue shifted by 34 cm^{-1}. As already mentioned above, this blue shift might be due to amplified stimulated emission (ASE) and post-pulses [127–130], but a systematic analysis of this effect is beyond the scope of this study.

5.4.4 Dispersion effects of optical windows on CARS signals

As mentioned above, with the longer initial pulse duration of ∼1 ps at ∼1 μm, one does not expect significant dispersion effects on the pulse duration with optical windows in the beam path. This is of great importance for the industrial applications in combustion and gasification diagnostics in a gas chamber or an oven.

In many combustion applications, the laser beams pass through dispersive media (e.g. optical windows). In order to investigate the influence of dispersion effects from optical windows on the CARS signals, two typical optical windows are tested, which are made of fused silica and BK7. These windows have an anti-reflection coating in the spectral range of 650-1050 nm (B-coating) with different thicknesses of 1 mm, 6 mm and 12 mm, respectively. The optical windows are positioned directly behind the 3 m focusing lens to avoid damage.

Due to the different optical windows, the optical beam paths of pump and probe pulses change slightly, which influences especially the temporal overlap of the two pulses. For each thickness of optical windows, one needs to adjust the probe delay time to optimize the CARS signals in air. The CARS signals of N_2 and O_2 without windows (black lines, Fig. 5.15 a, b) and with fused silica (Fig. 5.15 a) or BK7 (Fig. 5.15 b) windows at zero probe delay time are detected, using the maximum pulse energy of 60 mJ. The intensity is normalized with the peak point of the N_2 signal in the condition of without windows. One can see that the intensity of the CARS signals in air are slightly decreased by the insertion of the fused silica optical windows (red line: 1 mm, green line: 6 mm, blue line: 12 mm in Fig. 5.15 a). The insertion of BK7 optical windows (green line: 1 mm, blue line: 6 mm, red line: 12 mm in Fig. 5.15 b) leads to a stronger CARS signal intensity decrease. However, despite the decrease, the signal-to-noise ratio is still high, even for the thickest window (12 mm). With insertion of optical windows, the critical power P_c is significantly reduced according to Equation 3.48, as the refractive index n_2 of the glass is orders of magnitude larger than for gases. Therefore, according to Equations 3.52 and 3.53 the focusing distance is shorter and the beam is focusing tighter. Thus, the filamentation is

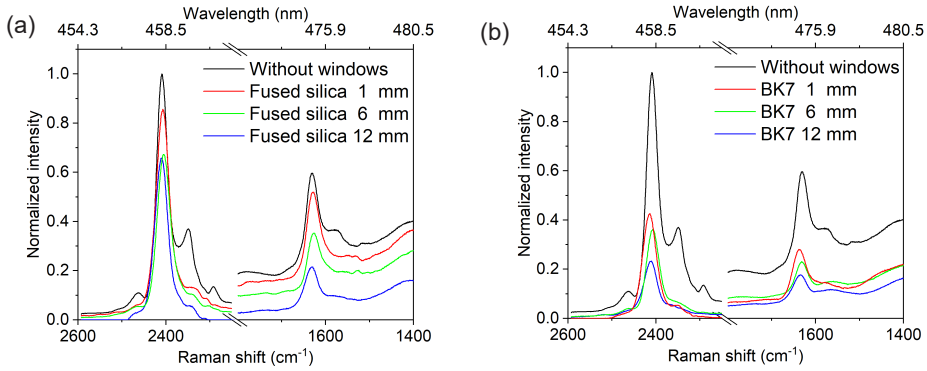


Figure 5.15: Dispersion effects from optical windows. Without windows: black line. Thicknesses: 1 mm (red line), 6 mm (green line), 12 mm (blue line) (a) With fused silica. (b) With BK7.

getting shorter and the broadened spectra are narrower. So the CARS signals are weaker as shown in Fig. 5.15. One can also notice that the background of the CARS signals also reduces.

5.5 Conclusion

In summary, we have systematically investigated the spectral properties of filamentation induced by focusing $\sim$ 1 ps laser pulses at a central wavelength of $\sim$ 1 μm in air. In this study the significant finding is that the spectral broadening spans from 850 nm to 1130 nm with a focusing lens f = 3 m at a pulse energy of 34 mJ. This spectral span corresponds to a Raman shift of $\sim$2900 cm^{-1}, which allowed the detection of the CARS signals of N_2, O_2 and even CH_4. By measuring a delay scan and comparing to simulations, an accuracy of 7 % could be demonstrated for the concentration determination of N_2 and O_2, despite strong fluctuations of the broadened spectrum. Reference measurements could improve the accuracy further. Inserting various thicknesses of optical windows we are still able to detect strong CARS signals of N_2 and O_2. The insertion of thick optical windows has only slight influences on the intensity of the CARS signal in air, providing further proof of the practicality of ps laser induced filamentation in the combustion diagnostics.

Chapter 6

Remote CARS based on fs filamentation

6.1 Overview

In the previous chapter the spectral properties of ps laser induced filamentation in air using an ultrafast thin-disk based amplifier at a central wavelength of 1030 nm at different focusing conditions are investigated. It shows that the spectrum induced by filamentation in air is sufficiently broad to simultaneously excite ro-vibrational Raman transitions in N_2, O_2 and even CH_4. With the SHG as a probe the CARS signals of the relevant gases are detected.

In the filamentation based CARS, SHG as a probe is a typical means to measure the CARS signals of various gases. However, in harsh environments e.g., in hazardous areas or in combustion devices, it is difficult to achieve a defined overlap for pump and probe pulses at long distances especially when one has limited access in the large-scale environments. Therefore, it is hard to achieve the temporal and spatial alignment under these conditions.

Recent discovery of air lasing in fs-filamentation opens exciting perspectives for remote sensing [95, 96, 99, 102, 133]. In this chapter, fs-filamentation enabling remote sensing with CARS is investigated. We show that the laser-like emission of excited N_2^+-ions accompanied by fs-filamentation could be used as a probe in remote CARS. The characteristics of

air lasing (e.g. narrow bandwidth, good directionality) make the single beam CARS for remote sensing promising, as the temporal and spatial alignment of the probe beam and the filament is intrinsically provided.

6.2 Experimental setup

Figure 6.1 (a) shows the energy diagram of N_2^+. First, the intense fs laser pulses induce the ionization from the (σ_u2s)-or (σ_g2p)-orbital. Thus, it leaves the ion in the states BΣ_u^+ or XΣ_g^+, respectively [99]. Fig. 6.1 (a) shows the lasing emissions from N_2^+ at wavelengths of 391 nm, 428 nm and 358.2 nm. In particular, the coherent emission from N_2^+ at ∼391 nm ($B^2\ \Sigma_u^+, \upsilon'' = 0 \rightarrow X^2\ \Sigma_g^+, \upsilon' = 0$) and ∼428 nm ($B^2\ \Sigma_u^+, \upsilon'' = 0 \rightarrow X^2\ \Sigma_g^+, \upsilon' = 1$) are close to the SHG (400 nm) of Ti:sapphire lasers, which is frequently used as a probe pulse. The bandwidths (FWHM) of the two lasing pulses are 0.24 nm (391 nm) and 0.28 nm (428 nm), which corresponds to the Fourier-transform-limited pulse durations of 0.93 and 0.96 ps, respectively [104, 134]. In this study, the stronger lasing signal, the lasing emission at ∼391 nm, will be used as probe in the single beam CARS. The detected lasing emission signals will be shown and discussed in the result section.

Fs-filamentation provides a new choice of ultrabroadband excitation laser for CARS, as the spectral broadening of the ultrashort pulses always accompanies the filamentation. Thus, the generated broadened spectra can be utilized as a perfect broadband light source in CARS. Odhner et al. [46] demonstrated the use of a Ti:sapphire based laser system with a pulse duration of 45 fs to generate a filament and realize a broad spectral range up to ∼4155 cm^{-1}. Figure 6.1 (b) shows the use of lasing emission from N_2^+ at 391 nm as probe to detect the CARS signal of N_2. Based on the energy difference of the emission lines, one can calculate the vibrational CARS signal of N_2, which should be centered at 358.7 nm.

In addition, we consider CO_2, which is a linear symmetric triatomic molecule as described in subsection 4.4.3, whose Raman spectrum shows the so-called Fermi dyads with Raman shift at Δv ∼1285 cm^{-1} and Δv ∼ 1388 cm^{-1} (Fig. 6.2). Based on the energy differ-

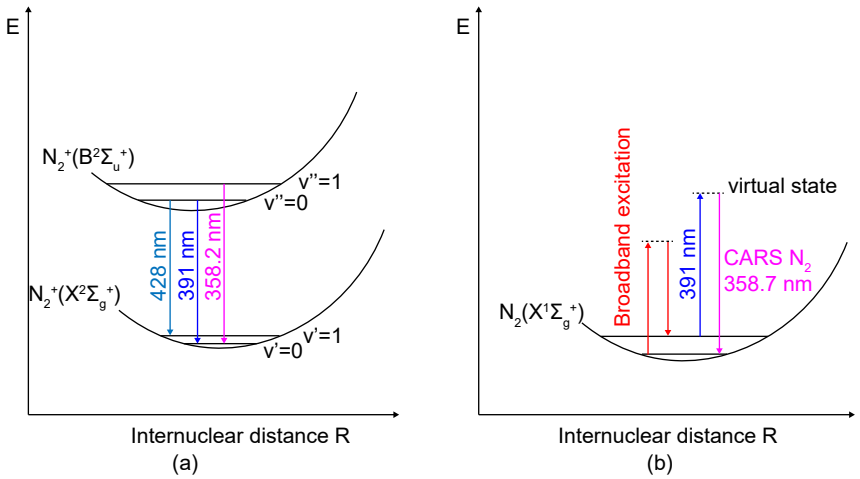


Figure 6.1: Potential curves of N_2 and N_2^+. (a) Lasing emission of N_2^+ at 358.2 nm ($B^2\,\Sigma_u^+, v'' = 1 \rightarrow X^2\,\Sigma_g^+, v' = 0$), 391 nm ($B^2\,\Sigma_u^+, v'' = 0 \rightarrow X^2\,\Sigma_g^+, v' = 0$) and 428 nm ($B^2\,\Sigma_u^+, v'' = 0 \rightarrow X^2\,\Sigma_g^+, v' = 1$). (b) Lasing emission at ~391 nm probes Raman levels of N_2 after broadband excitation to observe the CARS signal at 358.7 nm.

ence between the emission lines, the CARS signals of these peaks should be detected at 371.27 nm and 372.69 nm, respectively.

To further investigate the limit of the broadened spectrum after fs-filamentation and test the single beam CARS capability, CARS signals of other molecules with higher Raman shifts (especially CH_4 ~2917 cm^{-1} as an important species in many combustion scenarios) are tested. One does expect that the CARS signal of CH_4 peaks at 351.27 nm based on the energy difference of the emission lines.

A scheme of the experiment setup is shown in Fig. 6.3. A Ti:sapphire chirped pulse amplifier (Spitfire ACE, Newport) with a pulse duration of 35 fs and a repetition rate of 1 kHz was used. The pulse energy is adjusted by a half-wave plate and a polarizing beam splitter, providing a maximum pulse energy of E_{pulse} = 5.1 mJ with linear polarization and a beam diameter of ~10 mm $(1/e^2)$. The experiment is conducted in air and in a flow of CO_2 or CH_4 at an average rate of ~1.6 ml/s.

To avoid laser-induced damage, the beam was focused into a cell without side windows. The beam focus within the gas cell was set close to the gas inlet (Fig. 6.3) for the maximum

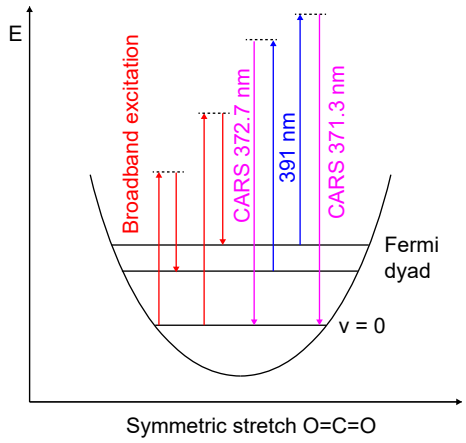


Figure 6.2: Scheme of generation of CARS signal of CO_2 with lasing emission at ∼391 nm as a probe. Lasing emission at ∼391 nm probes Raman levels of CO_2 after broadband excitation into the Fermi dyad with Raman shifts of Δv ∼1285 cm^{-1} and Δv ∼ 1388 cm^{-1}.

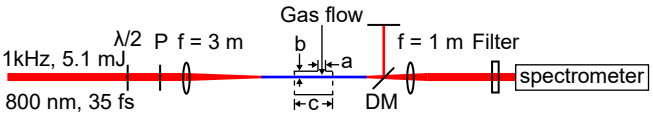


Figure 6.3: Scheme of the experimental setup for remote CARS. $\lambda/2$: half-wave plate. DM: dielectric mirror. P: polarizing beam splitter. a = 8 mm. b = ∼15 mm. c = 100 mm. The position of the generated filament is shown in blue line, which aligns closely to the gas inlet for the maximum CARS signal.

CARS signal. Downstream from the filament, a dielectric mirror (UM10 − 45 A, Thorlabs) filtered out the fundamental component at 800 nm. This mirror shows a transmission of ∼80% below 400 nm and ⩾ 99% above 400 nm. Subsequently, the laser beam was collimated by a lens (f = 1 m). After the collimator, the lasing pulse at 391 nm and the CARS signals passed through bandpass filters and neutral density (ND) filters, before they were coupled into a spectrometer (Shamrock 500i with a Newton 940 CCD, Andor Technology). The acquisition time was 50 ms, and 50 acquisitions were accumulated for each spectrum. The N_2^+ signal at 391 nm was maximized by adjusting the compressor gratings of the laser amplifier.

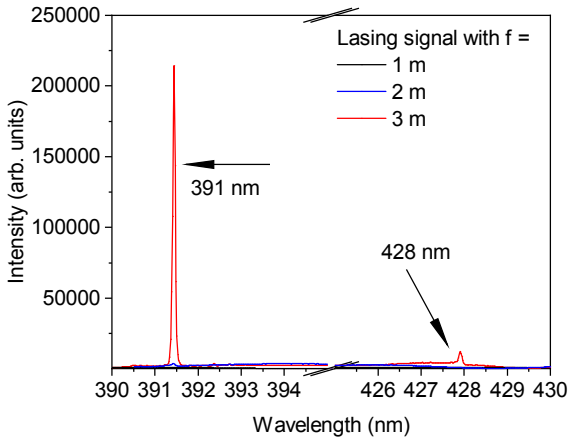


Figure 6.4: Lasing emission of N_2^+ at different focusing conditions. It shows the lasing peak at 391 nm and 428 nm using a focusing lens with f = 1 m (black line), f = 2 m (blue line), and f = 3 m (red line).

6.3 Fs filamentation enabling remote CARS

- **Generation of air lasing at 391 nm**

  Figure 6.4 shows the air lasing at 391.45 nm and 428 nm, using three different focusing lenses. The strongest air lasing was observed with an f = 3 m lens. No lasing was observed with f = 1 m, and with f = 2 m the lasing and CARS signal were weak. This is opposite to the observations of Jing et al. [135], who report an increasing lasing intensity for shorter focal lengths. In their work, after increasing the beam diameter with a telescope, the maximum lasing intensity occurred at an effective focal length of 2 m. The smaller initial beam diameter used in that study ($\sim$8 mm vs. $\sim$10 mm in this study) may be the reason for this behavior, but a more detailed study of this phenomenon is beyond the scope of this study. With the f = 3 m lens, the length of the filament was $\sim$30 cm, estimated from the visible plasma emission. Moreover, lasing emission at $\sim$428 nm was observed with lower intensity than at $\sim$391 nm. We therefore focused our investigations on remote CARS with respect to the 391 nm peak.

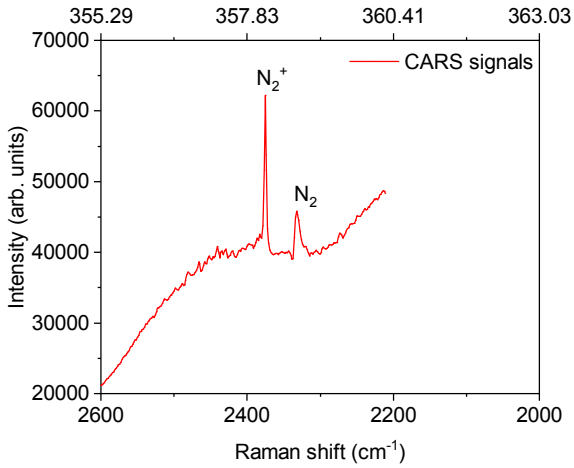


Figure 6.5: CARS signal of N_2 and the lasing emission of N_2^+. The CARS signal of N_2 in air.

- **CARS signals of N_2**

  To generate a ro-vibrational CARS signal of N_2, the white-light continuum must cover the Raman shift of $\Delta\nu$ 2330 cm^{-1}. Then the lasing pulse at ~391 nm probes this excitation, resulting in a CARS peak at 358.70 nm. This CARS signal is shown in Fig. 6.5. In additon, a peak at 358.2 nm appears, which fits to the transition $B^2\ \Sigma_u^+, \upsilon'' = 1 \rightarrow X^2\ \Sigma_g^+, \upsilon' = 0$ of N_2^+ and could also arise from CARS, when the (excited) $B^2\ \Sigma_u^+$ level of N_2^+ is probed at ~391 nm. However, the peak is higher than that of neutral N_2 and, as we did not observe any CARS from the ground level of N_2^+ (Fig. 6.6), which has a Raman shift of 2175 cm^{-1} (Table 6.1), we instead attribute the signal at 358.2 nm to the lasing of N_2^+. The polarization of the lasing and CARS signals was verified by means of a polarizing beam splitter in front of the spectrometer. The CARS signals have the same polarization as the filamentary beam and the lasing signal.

- **CARS signal of CO_2**

  With the 391 nm as probe in CARS, the CARS signals of CO_2 are detected at 371.27 nm and 372.69 nm as shown in Fig. 6.6. The measurement is conducted in a

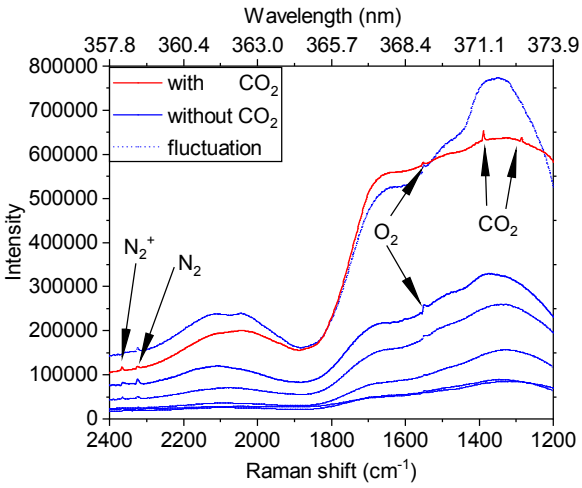


Figure 6.6: CARS spectrum of N_2, O_2, and CO_2 and lasing emission of N_2^+. The dashed lines show fluctuations of the white-light continuum for five spectra without CO_2. The CO_2 gas was continuously flowing into the gas cell while measuring the CARS signal of CO_2.

flow of CO_2 at an average rate of $\sim$1.6 ml/s. The white-light background is strong, but both peaks can be clearly identified when comparing the spectra with (red) and without (blue) CO_2. The fluctuations of the white-light continuum are also shown in Fig. 6.6. Even though the strong fluorescence signal and fluctuations of the spectra, the spectral spikes are distinguishable. Due to the missing cell windows, the CARS peaks of N_2 and O_2 were observed with and without CO_2, respectively.

- **CARS signal of CH_4**

  The CH_4 gas was continuously flowing into the gas cell with an average flow rate of $\sim$1.6 ml/s while measuring the CARS signal of CH_4. The CARS signal of CH_4 is detected at 351.27 nm as shown in Fig. 6.7. The pulse energy of the pump E_{pulse} is $\sim$ 5.1 mJ.

Table 6.1 summarizes the measured signals and the literature values for the Raman shifts, which slightly depend on temperature and concentration. As the concentration of CO_2 and CH_4 whthin the cell is presumably small, we chose the zero density limit for the literature Raman shifts for these molecules. Taking the resolution of the spectrometer of 0.06 nm

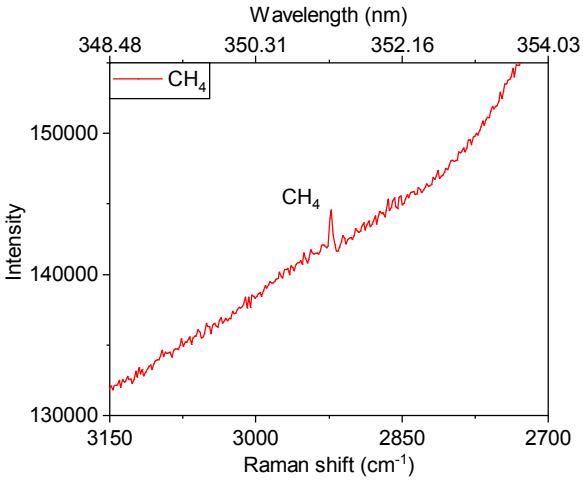


Figure 6.7: CARS signal of CH_4. The CH_4 peak is centered at 351. 27 nm.

into acccount, there is very good agreement between the measured data and literature values. It is noteworthy that we did not observe any CARS signal from the ground state of N_2^+ ($X^2\ \Sigma_g^+$), which would explain well the necessary population inversion for the 391 nm lasing ($B^2\ \Sigma_u^+, \upsilon'' = 0 \rightarrow X^2\ \Sigma_g^+, \upsilon' = 0$), but which is in contrast to our previous observations using sub-10 fs pulses as excitation, where the CARS peak from the ($X^2\ \Sigma_g^+$) state was the strongest signal from N_2^+ [136]. Further investigations on the Raman cross sections of the states involved are necessary for a quantitative analysis of this observation.

The remote CARS technique shown in this chapter may be applied for both thermometry and concentration measurements. Thermometry relies on the fact that the characteristic collision time for gas molecules is a few tens of picoseconds, e.g. $\sim$100 ps for N_2 at ambient conditions [3], and therefore can be neglected for fs laser pulses. Then the temperature may be determined from the rotational lines [43], the population of vibrational levels [40, 121], or the decay of the Raman coherence [3, 76]. As the probe delay time in this technique is fixed, thermometry may be derived from a single CARS spectra [8, 40, 43, 76, 121]. For reliable measurements, further knowledge about the delay between the excitation and the lasing pulse is necessary. This is since the resonant Raman signal shows a characteristic decay for the molecule under investigation; e.g., the signal of N_2 decays within a few picoseconds at ambient conditions [3], whereas no decay is observed for CO_2

Table 6.1: Comparison of measured and theoretical data. The Raman shifts of the different gases N_2, N_2^+ are taken from [a] Lofthus et al. [63], O_2 from [b] Krupenie et al. [64], CO_2 from [c] Wright et al. [137], CH_4 from [d] Shang et al. [138].

Gas	Measured signal (nm)	Literature Raman shift (cm^{-1})	Measured Raman shift (cm^{-1})
N_2	358.70±0.03	2330[a]	2332±4
N_2^+	358.17±0.03	2374[a]	2375±4
N_2^+	-	2175[a]	-
O_2	369.00±0.03	1556[b]	1554±4
CO_2	371.27±0.03	1389[c]	1389±4
CO_2	372.69±0.03	1287[c]	1286±4
CH_4	351.27±0.03	2917[d]	2922±4

at pressures up to 10 bar [38]. Thus, uncertainty about the actual probe pulse delay may induce considerable errors. The delay of the lasing signal depends on the pressure and may reach up to ∼10 ps for a few millibars; for high pressures (⩽20 mbar), it drops to ∼1 ps [139, 140]. The delay may be determined by cross-correlational experiments [139], which is beyond the scope of this study.

Furthermore, concentration measurements using broadband excitation is the current state of research, even when the broadband pulse is provided the laser. Bohlin et al. suggest using the nonresonant signal for the correction of spectral instabilities [6]. Using sub-10 fs pulses, we recently determined concentrations for N_2, CO_2 and CO, but the determination failed for molecules with larger Raman shifts (H_2) [8]. Figure 6.7 suggests that measurements using filamentation are even more challenging; e.g., the 800 nm component and the 3rd harmonic [52] possibly contribute to a larger extend to the excitation than the other spectral components. A rough analysis of the peak ratio without CO_2 yields $N_2/O_2 \sim 0.45$, although one expects $N_2/O_2 > 1$ from the natureal composition in air [5]. Using filamentation and a separate probe, Odhner et al. measured a ratio close to the expected one, but they also suggest considering the pulse characteristics for a deeper analysis [46]. Moreover, the

sensitivity of the current setup is poor. Assuming a length of ∼30 cm and a diameter of ∼100 μm [141], a rather small O_2 peak (Fig. 6.6) arises from $\sim 10^{16}$ O_2 molecules within the filament. In addition, the donut shape of the lasing beam may be responsible for a limited spatial overlap, and thus lower sensitivity [133].

On the other hand, our setup ($E_{pulse} \sim 5$ mJ) is at the lower limit for filamentation in air. Stable white-light generation occurs at $E_{pulse} \sim 3$ mJ under similar experimental conditions [140]. The CARS signal could therefore be optimized by the length of the filament, that is, by the focusing conditions. In this way, the measurement range may be adapted from centimeters (in this study) to a few hundreds of meters [142]. Further studies on the efficient generation of the white light, lasing, and CARS signal are required to evaluate possible, real-scale spectroscopic applications.

6.4 Conclusion

For the first time, we are able to employ a single beam for remote CARS based on fs-filamentation. In this study, we have observed air lasing emission lines from N_2^+ in intense 800 nm fs laser fields. With the lasing emission at ∼391 nm acting as a probe in CARS, the CARS signals of N_2, O_2, CO_2 and CH_4 were observed. Our findings may be applied to remote sensing applications, for which it is essential to overcome diffraction for both the pump and probe pulse.

Chapter 7

Summary and outlook

Summary The aim of this work was to investigate and extend the capability of the CARS technique for temperature and concentration measurements in harsh environments (e.g. combustion and gasification diagnotics). N_2, O_2 and CO_2 CARS are typical means of measuring the gas phase temperature and concentration. From the magnitude and delay of the initial Raman coherence induced by the pump and Stokes beams in various gases one can determine the gas phase temperature and relative concentration. In this thesis we mainly used the relative peak ratio of N_2 and O_2 CARS signals to evaluate the relative concentration and N_2 vibrational CARS to determine the temperature.

Two types of laser systems are used: a thin-disk based ps laser system and a Ti:sapphire based fs laser system. The thin-disk laser system is based on a stable and reliable fiber oscillator and can provide $\sim$ 1 ps pulses. The main CARS techniques investigated are highlighted below:

- **CARS based on a reliable ps-laser system with OPA**
  In the first approach, a customized ps-OPA (APE, Germany) pumped with a commercial thin-disk based 1 kHz laser system was set up and characterized. This ps-OPA can provide a pulse energy of $\sim$ 200 μJ and a pulse duration of $\sim$ 1 ps across the whole tuning range 700 - 950 nm.

For the first time, we demonstrated the $\sim$ 1 ps CARS setup with a tunable $\sim$ 1 ps OPA system. With the output of the OPA as pump, the thin-disk laser pulses at 1030 nm as Stokes, and the second harmonic (515 nm) as probe, we investigated the CARS signals of N_2 and CO_2 at high temperatures in a gas cell. The ps-CARS setup can provide sufficient spectral resolution (20 cm^{-1}) to distinguish the fundamental and the first hot band of N_2. In N_2 ps CARS for temperature determination, three different ways have been used: intensity ratio of N_2 peaks, dephasing rate of the fundamental peak and the first hot band of N_2. In the first method, the intensity ratio of the first hot band and the fundamental peak is $\sim$ 0.2 at the maximum temperature of 720 °C, which fits well the literature value at $\sim$ 1000 K ($\sim$ 727 °C) [118]. For the depahsing rate of N_2 peaks, the temperature determination accuracy with the first hot band is better (2 % vs 4 % for the fundamental peak) at higher temperature of 720 °C.

For CO_2 CARS, we mainly considered the vibrational transitions corresponding to Raman shifts of 1388 cm^{-1} and 1409 cm^{-1} for temperature determination. We measured the two peaks at temperatures of 20 °C, 250 °C and 500 °C at a pressure of 3 bar in the gas cell. With increasing temperature to 500 °C, we could clearly see the relative signal strength at Raman shift of 1409 cm^{-1} getting stronger due to higher molecular population. At a temperature of 500 °C, the intensity ratio between the CO_2 peaks is 0.7, which deviates from our previous study (0.6 [8]). We attribute this deviation to the large spectral overlap of the CO_2 CARS signals at 1388 cm^{-1} and 1409 cm^{-1}.

With this high temporal ($\sim$ 1 ps) and spectral (20 cm^{-1}) resolution CARS setup, one can have a higher signal-to-noise ratio and investigate the characteristics of each Raman transition precisely. These advantages contribute to the sensitivity, flexibility and efficiency of the CARS experiment, making it a valuable tool for gas analysis in harsh environments.

- **CARS based on ps-filamentation**

We have systematically investigated the spectral properties induced by ps-filamentation in air with maximum pulse energy of 60 mJ under different focusing conditions (f = 2 m, 3 m and 4 m). In this study the significant finding is that the spectral broadening spans from 850 nm to 1130 nm with a focusing lens f = 3 m at a pulse energy of 34 mJ, in contrast to the spanning range (1010 nm to 1050 nm) in the results of Houard et al. [50]. The spectral span in this study corresponds to a Raman shift of $\sim$2900 cm^{-1}, which allowed the detection of the CARS signals of N_2, O_2 and even CH_4 with such a ps-based approach for the first time. One drawback is the large fluctuations in the filamentation spectra, leading to an average standard deviation of 54 $\%$ for the peak ratios of N_2 and O_2. However, measuring the dependence of the ratio as a function of the delay, we could reduce the error to 14 $\%$, allowing the concentration detection with an accuracy of 7 $\%$. Further improvements will require in-situ measuring and referencing of the broadened filamentation spectra.

Furthermore, we studied the effect of insertion of optical windows on the CARS signals with ps-filamentation. In this study, two typical optical windows with different thicknesses were tested, which are made of fused silica and BK7. The insertion of optical windows do not suppress CARS signal generation, which provides further proof of the practicality of ps-filamentation in combustion diagnostics.

- **Remote CARS based on fs-filamentation**

  In the previous two approaches two or three beams ps-CARS are used for gas analysis. However, in large scale device measurements, it is difficult to achieve a defined overlap for pump and probe beams at long distances especially when one has limited access in harsh environments. Therefore, it is hard to achieve the temporal and spatial alignment under these conditions.

  For the first time, we are able to employ the single beam for remote CARS based on fs-filamentation. In this study, we have observed air lasing $\sim$391 nm from N_2^+ in intense 800 nm fs laser fields. With the lasing emission at $\sim$391 nm acting as a probe in CARS, the CARS signals of N_2, O_2, CO_2 and CH_4 were observed. Our

findings may be applied to remote sensing applications, for which it is essential to overcome diffraction for both the pump and probe pulse. This can also pave the way for single beam ps-filamentation based CARS in harsh environment.

Outlook

In a recent study, our group has already investigated the carbon gasification in a CO_2 atmosphere using ultrabroadband CARS. Due to the low concentration of CO in the reaction process, the modulation dips of the CO CARS signal are used to determine the concentration [143]. In the future, we are planing to use the customized ps-CARS setup with high spectral resolution, wide tunability and high power for the minor species (e.g. CO) at extremely low concentration and other species (e.g. CH_4, H_2O and H_2) for gas analysis in harsh environments. Implementing two-beam or three-beam CARS in harsh industrial environments has been limited by the requirement to maintain spatial and temporal overlap between multiple laser beams under high pressure and high temperature turbulent conditions. In this regard, single beam filamentation based CARS could be promising for industrial applications. In this thesis, we showed that fs-filamentation can enable the remote CARS with the air lasing at 391 nm as probe in CARS process. However, the self-seeded air lasing beam in the forward or backward direction is still not yet reported at a central wavelength of 1030 nm with $\sim$ 1 ps thin-disk laser systems. So, achieving the single beam ps-filamentation based CARS for gas analysis in harsh environments will be our next step.

Bibliography

[1] S. Roy, J. R. Gord, and A. K. Patnaik, "Recent advances in coherent anti-stokes raman scattering spectroscopy: Fundamental developments and applications in reacting flows," Prog. Energ. Combust. **36**, 280–306 (2010).

[2] C. Brackmann, J. Bood, M. Afzelius, and P.-E. Bengtsson, "Thermometry in internal combustion engines via dual-broadband rotational coherent anti-stokes raman spectroscopy," Meas. Sci. Technol. **15**, R13–R25 (2004).

[3] R. P. Lucht, S. Roy, T. R. Meyer, and J. R. Gord, "Femtosecond coherent anti-stokes raman scattering measurement of gas temperatures from frequency-spread dephasing of the raman coherence," Appl. Phys. Lett. **89**, 251112 (2006).

[4] F. Mazza, A. Stutvoet, L. Castellanos, D. Kliukin, and A. Bohlin, "Coherent raman spectroscopy on hydrogen with in-situ generation, in-situ use, and in-situ referencing of the ultrabroadband excitation," Opt. Express **30**, 35232 (2022).

[5] G. Matthäus, S. Demmler, M. Lebugle, F. Küster, J. Limpert, A. Tünnermann, S. Nolte, and R. Ackermann, "Ultra-broadband two beam CARS using femtosecond laser pulses," Vib. Spectrosc. **85**, 128–133 (2016).

[6] A. Bohlin and C. J. Kliewer, "Two-beam ultrabroadband coherent anti-stokes raman spectroscopy for high resolution gas-phase multiplex imaging," Appl. Phys. Lett. **104**, 031107 (2014).

[7] D. R. Richardson, H. U. Stauffer, S. Roy, and J. R. Gord, "Comparison of chirped-probe-pulse and hybrid femtosecond/picosecond coherent anti-stokes raman scattering for combustion thermometry," Appl. Opt. **56**, E37 (2017).

[8] Y. Ran, M. Junghanns, A. Boden, S. Nolte, A. Tünnermann, and R. Ackermann, "Temperature and gas concentration measurements with vibrational ultra-broadband two-beam femtosecond/picosecond coherent anti-stokes raman scattering and spontaneous raman scattering," J. Raman Spectrosc. **50**, 1268–1275 (2019).

[9] C. Herkommer, P. Krötz, R. Jung, S. Klingebiel, C. Wandt, R. Bessing, P. Walch, T. Produit, K. Michel, D. Bauer, R. Kienberger, and T. Metzger, "Ultrafast thin-disk multipass amplifier with 720 mJ operating at kilohertz repetition rate for applications in atmospheric research," Opt. Express **28**, 30164 (2020).

[10] P. R. REGNIER, F. MOYA, and J. P. E. TARAN, "Gas concentration measurement by coherent raman anti-stokes scattering," AIAA Journal **12**, 826–831 (1974).

[11] A. C. Eckbreth, *Laser diagnostics for combustion temperature and species.*, vol. 3 (CRC press, 1996).

[12] S. Roy, W. D. Kulatilaka, R. P. Lucht, N. G. Glumac, and T. Hu, "Temperature profile measurements in the near-substrate region of low-pressure diamond-forming flames," Combust. Flame **130**, 261–276 (2002).

[13] R. P. Lucht, "Three-laser coherent anti-stokes raman scattering measurements of two species," Opt. Lett. **12**, 78 (1987).

[14] A. C. Eckbreth and T. J. Anderson, "Dual broadband CARS for simultaneous, multiple species measurements," Appl. Opt. **24**, 2731 (1985).

[15] W. Clauss, V. Fabelinsky, D. Kozlov, V. Smirnov, O. Stelmakh, and K. Vereschagin, "Dual-broadband CARS temperature measurements in hydrogen-oxygen atmospheric pressure flames," Appl. Phys. B: Lasers Opt. **70**, 127–131 (2000).

[16] R. D. Hancock, K. E. Bertagnolli, and R. P. Lucht, "Nitrogen and hydrogen CARS temperature measurements in a hydrogen/air flame using a near-adiabatic flat-flame burner," Combust. Flame **109**, 323–331 (1997).

[17] M. A. Woodmansee, R. P. Lucht, and J. C. Dutton, "Stark broadening and stimulated raman pumping in high-resolution n coherent anti-stokes raman scattering spectra," AIAA Journal **40**, 1078–1086 (2002).

[18] C. F. Kaminski and P. Ewart, "Multiplex H_2 coherent anti-stokes raman scattering thermometry with a modeless laser," Appl. Opt. **36**, 731 (1997).

[19] M. Aldén, P.-E. Bengtsson, and H. Edner, "Rotational CARS generation through a multiple four-color interaction," Appl. Opt. **25**, 4493 (1986).

[20] F. Vestin, M. Afzelius, and P.-E. Bengtsson, "Improved species concentration measurements using a species-specific weighting procedure on rotational CARS spectra," J. Raman Spectrosc. **36**, 95–101 (2005).

[21] M. Schenk, A. Thumann, T. Seeger, and A. Leipertz, "Pure rotational coherent anti-stokes raman scattering: comparison of evaluation techniques for determining single-shot simultaneous temperature and relative N_2-O_2 concentration," Appl. Opt. **37**, 5659 (1998).

[22] M. Schenk, T. Seeger, and A. Leipertz, "Time-resolved CO_2 thermometry for pressures as great as 5 MPa by use of pure rotational coherent anti-stokes raman scattering," Appl. Opt. **44**, 6526 (2005).

[23] Y. Gao, M. C. Weikl, T. Seeger, A. Leipertz, P. Joubert, and J. Bonamy, "Evaluation of temperature and concentration in H_2 spectra using the keilson and storer three-dimensional model for H_2 Q-branch," J. Raman Spectrosc. **40**, 781–787 (2009).

[24] S. Roy, T. R. Meyer, R. P. Lucht, V. M. Belovich, E. Corporan, and J. R. Gord, "Temperature and CO_2 concentration measurements in the exhaust stream of a liquid-

fueled combustor using dual-pump coherent anti-stokes raman scattering (CARS) spectroscopy," Combust. Flame **138**, 273–284 (2004).

[25] S. O. Konorov, M. W. Blades, and R. F. B. Turner, "Lorentzian amplitude and phase pulse shaping for nonresonant background suppression and enhanced spectral resolution in coherent anti-stokes raman scattering spectroscopy and microscopy," Appl. Spectrosc. **64**, 767–774 (2010).

[26] S. O. Konorov, M. W. Blades, and R. F. B. Turner, "Non-resonant background suppression by destructive interference in coherent anti-stokes raman scattering spectroscopy," Opt. Express **19**, 25925 (2011).

[27] D. R. Richardson, D. Bangar, and R. P. Lucht, "Polarization suppression of the nonresonant background in femtosecond coherent anti-stokes raman scattering for flame thermometry at 5 khz," Opt. Express **20**, 21495 (2012).

[28] F. M. Kamga and M. G. Sceats, "Pulse-sequenced coherent anti-stokes raman scattering spectroscopy: a method for suppression of the nonresonant background," Opt. Lett. **5**, 126 (1980).

[29] T. R. Meyer, S. Roy, and J. R. Gord, "Improving signal-to-interference ratio in rich hydrocarbon-air flames using picosecond coherent anti-stokes raman scattering," Appl. Spectrosc. **61**, 1135–1140 (2007).

[30] T. Seeger, J. Kiefer, A. Leipertz, B. D. Patterson, C. J. Kliewer, and T. B. Settersten, "Picosecond time-resolved pure-rotational coherent anti-stokes raman spectroscopy for N_2 thermometry," Opt. Lett. **34**, 3755 (2009).

[31] D. Richardson, R. Lucht, S. Roy, and J. Gord, "Single-pulse femtosecond coherent anti-stokes raman scattering (CARS) spectroscopy for temperature measurements at data rates of 1 kHz," (2009).

[32] A. Bohlin and C. J. Kliewer, "Communication: Two-dimensional gas-phase coherent anti-stokes raman spectroscopy (2d-cars): Simultaneous planar imaging and multiplex spectroscopy in a single laser shot," J. Chem. Phys. **138** (2013).

[33] N. Dudovich, D. Oron, and Y. Silberberg, "Single-pulse coherently controlled nonlinear raman spectroscopy and microscopy," Nature **418**, 512–514 (2002).

[34] T. Lang, K.-L. Kompa, and M. Motzkus, "Femtosecond CARS on H_2," Chem. Phys. Lett. **310**, 65–72 (1999).

[35] G. Knopp, P. Beaud, P. Radi, M. Tulej, B. Bougie, D. Cannavo, and T. Gerber, "Pressure-dependent N_2 Q-branch fs-CARS measurements," J. Raman Spectrosc. **33**, 861–865 (2002).

[36] P. Beaud, H.-M. Frey, T. Lang, and M. Motzkus, "Flame thermometry by femtosecond CARS," Chem. Phys. Lett. **344**, 407–412 (2001).

[37] S. Roy, D. Richardson, P. J. Kinnius, R. P. Lucht, and J. R. Gord, "Effects of N_2–CO polarization beating on femtosecond coherent anti-stokes raman scattering spectroscopy of N_2," Appl. Phys. Lett. **94**, 144101 (2009).

[38] W. D. Kulatilaka, J. R. Gord, and S. Roy, "Effects of O_2-CO_2 polarization beating on femtosecond coherent anti-stokes raman scattering (fs-CARS) spectroscopy of O_2," Appl. Phys. B **102**, 141–147 (2010).

[39] D. Pestov, M. Zhi, Z.-E. Sariyanni, N. G. Kalugin, A. Kolomenskii, R. Murawski, Y. V. Rostovtsev, V. A. Sautenkov, A. V. Sokolov, and M. O. Scully, "Femtosecond CARS of methanol-water mixtures," J. Raman Spectrosc. **37**, 392–396 (2006).

[40] S. Roy, P. J. Kinnius, R. P. Lucht, and J. R. Gord, "Temperature measurements in reacting flows by time-resolved femtosecond coherent anti-stokes raman scattering (fs-CARS) spectroscopy," Opt. Commun. **281**, 319–325 (2008).

[41] T. Y. Chen, C. J. Kliewer, B. M. Goldberg, E. Kolemen, and Y. Ju, "Time-domain modelling and thermometry of the CH_4 Q-branch using hybrid femtosecond/picosecond coherent anti-stokes raman scattering," Combust. Flame **224**, 183–195 (2021).

[42] J. D. Miller, M. N. Slipchenko, T. R. Meyer, H. U. Stauffer, and J. R. Gord, "Hybrid femtosecond/picosecond coherent anti-stokes raman scattering for high-speed gas-phase thermometry," Opt. Lett. **35**, 2430 (2010).

[43] J. D. Miller, S. Roy, M. N. Slipchenko, J. R. Gord, and T. R. Meyer, "Single-shot gas-phase thermometry using pure-rotational hybrid femtosecond/picosecond coherent anti-stokes raman scattering," Opt. Express **19**, 15627 (2011).

[44] S. A. Steinmetz and C. J. Kliewer, "Gas detection sensitivity of hybrid fs/ps and fs/ns CARS," Opt. Lett. **47**, 1470 (2022).

[45] M. Scherman, M. Nafa, T. Schmid, A. Godard, A. Bresson, B. Attal-Tretout, and P. Joubert, "Rovibrational hybrid fs/ps CARS using a volume bragg grating for N_2 thermometry," Opt. Lett. **41**, 488 (2016).

[46] J. H. Odhner, D. A. Romanov, and R. J. Levis, "Rovibrational wave-packet dispersion during femtosecond laser filamentation in air," Phys. Rev. Lett. **103**, 075005 (2009).

[47] F. Mazza, N. Griffioen, L. Castellanos, D. Kliukin, and A. Bohlin, "High-temperature rotational-vibrational O_2-CO_2 coherent raman spectroscopy with ultra-broadband femtosecond laser excitation generated in-situ," Combust. Flame **237**, 111738 (2022).

[48] Z. Tian, H. Zhao, Y. Gao, H. Wei, Y. Tan, and Y. Li, "Filamentation-based, two-beam, 1-kHz, and single-shot N vibrational CARS thermometry in high-temperature flames," Appl. Phys. Lett. **121**, 081102 (2022).

[49] X. Zhao, S. Nolte, and R. Ackermann, "Lasing of N_2^+ induced by filamentation in air as a probe for femtosecond coherent anti-stokes raman scattering," Opt. Lett. **45**, 3661 (2020).

[50] A. Houard, V. Jukna, G. Point, Y.-B. André, S. Klingebiel, M. Schultze, K. Michel, T. Metzger, and A. Mysyrowicz, "Study of filamentation with a high power high repetition rate ps laser at 1.03 μm," Opt. Express **24**, 7437 (2016).

[51] T. Produit, P. Walch, G. Schimmel, B. Mahieu, C. Herkommer, R. Jung, T. Metzger, K. Michel, Y.-B. André, A. Mysyrowicz, A. Houard, J. Kasparian, and J.-P. Wolf, "HV discharges triggered by dual- and triple-frequency laser filaments," Opt. Express **27**, 11339 (2019).

[52] F. Théberge, W. Liu, Q. Luo, and S. Chin, "Ultrabroadband continuum generated in air (down to 230 nm) using ultrashort and intense laser pulses," Appl. Phys. B **80**, 221–225 (2005).

[53] F. Théberge, M. Châteauneuf, V. Ross, P. Mathieu, and J. Dubois, "Ultrabroadband conical emission generated from the ultraviolet up to the far-infrared during the optical filamentation in air," Opt. Lett. **33**, 2515 (2008).

[54] T. Produit, P. Walch, C. Herkommer, A. Mostajabi, M. Moret, U. Andral, A. Sunjerga, M. Azadifar, Y.-B. André, B. Mahieu, W. Haas, B. Esmiller, G. Fournier, P. Krötz, T. Metzger, K. Michel, A. Mysyrowicz, M. Rubinstein, F. Rachidi, J. Kasparian, J.-P. Wolf, and A. Houard, "The laser lightning rod project," EPJ Appl. Phys. **93**, 10504 (2021).

[55] H. Zhang and Q. Gong, "Triggering and guiding of lightning by ultrafast lasers," Proc. SPIE, 2019 International Conference on Optical Instruments and Technology: Advanced Laser Technology and Applications **11437**, 114370O (2020).

[56] P. Atkins and J. de Paula, *Atkins' Physical Chemistry* (Oxford University Press, 2014).

[57] S. L. Chin, *Femtosecond Laser Filamentation* (Springer New York, 2010).

[58] Y. R. Shen and G.-Z. Yang, *Theory of Self-Phase Modulation and Spectral Broadening* (Springer New York, 2016).

[59] C.-P. S. Ingolf V. Hertel, *Atoms, Molecules and Optical Physics 1* (Springer Berlin Heidelberg, 2015).

[60] R. R. Laher and F. R. Gilmore, "Improved fits for the vibrational and rotational constants of many states of nitrogen and oxygen," J. Phys. Chem. Ref. Data **20**, 685–712 (1991).

[61] L. Rothman, R. Hawkins, R. Wattson, and R. Gamache, "Energy levels, intensities, and linewidths of atmospheric carbon dioxide bands," J. Quant. Spectrosc. Radiat. Transf. **48**, 537–566 (1992).

[62] P. Richet, Y. Bottinga, and M. Javoy, "A review of Hydrogen, Carbon, Nitrogen, Oxygen, Sulphur, and Chlorine stable isotope fractionation among gaseous molecules," Annu. Rev. Earth Planet. Sci. **5**, 65–110 (1977).

[63] A. Lofthus and P. H. Krupenie, "The spectrum of molecular nitrogen," J. Phys. Chem. Ref. Data **6**, 113–307 (1977).

[64] P. H. Krupenie, "The spectrum of molecular oxygen," J. Phys. Chem. Ref. Data **1**, 423–534 (1972).

[65] L. Gray and J. E. Selvidge, "Relative intensity calculations for carbon dioxide," J. Quant. Spectrosc. Radiat.Transf. **5**, 291–301 (1965).

[66] Y. Yu, K. Lin, X. Zhou, H. Wang, S. Liu, and X. Ma, "Precise measurement of the depolarization ratio from photoacoustic raman spectroscopy," J. Raman Spectrosc. **38**, 1206–1211 (2007).

[67] A. C. Eckbreth, "BOXCARS: Crossed-beam phase-matched CARS generation in gases," Applied Physics Letters **32**, 421–423 (1978).

[68] D. A. Greenhalgh, "Comments on the use of BOXCARS for gas-phase CARS spectroscopy," Journal of Raman Spectroscopy **14**, 150–153 (1983).

[69] C. M. Valensise, A. Giuseppi, F. Vernuccio, A. D. la Cadena, G. Cerullo, and D. Polli, "Removing non-resonant background from CARS spectra via deep learning," APL Photonics **5**, 061305 (2020).

[70] S. Takizawa, K. Hiramatsu, and K. Goda, "Compressed time-domain coherent raman spectroscopy with real-time random sampling," Vib. Spectrosc. **107**, 103042 (2020).

[71] M. Cui, M. Joffre, J. Skodack, and J. P. Ogilvie, "Interferometric fourier transform coherent anti-stokes raman scattering," Opt. Express **14**, 8448 (2006).

[72] R. W. Boyd, *Nonlinear Optics* (Academic Press, 2008).

[73] J. Laane and W. Kiefer, "Interference effects in the high resolution CARS spectra of gases," J Raman Spectrosc **9**, 353–360 (1980).

[74] M. Yuratich and D. Hanna, "Coherent anti-stokes raman spectroscopy (CARS)," Mol. Phys. **33**, 671–682 (1977).

[75] G. Tejeda, B. Maté, and S. Montero, "Overtone raman spectrum and molecular polarizability surface of CO_2," J. Chem. Phys. **103**, 568–576 (1995).

[76] D. R. Richardson, R. P. Lucht, W. D. Kulatilaka, S. Roy, and J. R. Gord, "Theoretical modeling of single-laser-shot, chirped-probe-pulse femtosecond coherent anti-stokes raman scattering thermometry," Appl. Phys. B **104**, 699–714 (2011).

[77] R. P. Lucht, "Me 687: Laser diagnostics for reacting flows class notes," Purdue University (2018).

[78] M. Marrocco, "Comparative analysis of herman-wallis factors for uses in coherent anti-stokes raman spectra of light molecules," J. Raman Spectrosc. **40**, 741–747 (2009).

[79] M. Marrocco, "Herman–wallis factor to improve thermometric accuracy of vibrational coherent anti-stokes raman spectra of H_2," Proc. Combust. Inst. **32**, 863–870 (2009).

[80] D. R. Richardson, R. P. Lucht, S. Roy, W. D. Kulatilaka, and J. R. Gord, "Single-laser-shot femtosecond coherent anti-stokes raman scattering thermometry at 1000 Hz in unsteady flames," Proc. Combust. Inst. **33**, 839–845 (2011).

[81] G. O. Ariunbold and N. Altangerel, "Coherent anti-stokes raman spectroscopy: Understanding the essentials," Coherent Opt. Phenom. **3** (2016).

[82] G. Askaryan, "Effects of the gradient of a strong electromagnetic beam on electrons and atoms," Soviet. Phys. JETP **15**, 1088–1090 (1962).

[83] C. R. Giuliano, "Laser-induced damage to transparent dielectric Materials," Appl. Phys. Lett. **5**, 137–139 (1964).

[84] F. Shimizu, "Frequency broadening in liquids by a short light pulse," Phys. Rev. Lett. **19**, 1097–1100 (1967).

[85] A. Braun, G. Korn, X. Liu, D. Du, J. Squier, and G. Mourou, "Self-channeling of high-peak-power femtosecond laser pulses in air," Opt. Lett. **20**, 73 (1995).

[86] W. Liu and S. L. Chin, "Direct measurement of the critical power of femtosecond ti:sapphire laser pulse in air," Opt. Express **13**, 5750 (2005).

[87] S. L. Chin, T. J. Wang, C. Marceau, J. Wu, J. S. Liu, O. Kosareva, N. Panov, Y. P. Chen, J. F. Daigle, S. Yuan, A. Azarm, W. W. Liu, T. Seideman, H. P. Zeng, M. Richardson, R. Li, and Z. Z. Xu, "Advances in intense femtosecond laser filamentation in air," Laser Phys. **22**, 1–53 (2011).

[88] J. H. Marburger, "Self-focusing: theory," Prog. Quantum Electron. **4**, 35–110 (1975).

[89] A. COUAIRON and A. MYSYROWICZ, "Femtosecond filamentation in transparent media," Phys. Rep. **441**, 47–189 (2007).

[90] L. Wöste, S. Frey, and J.-P. Wolf, "LIDAR-monitoring of the air with femtosecond plasma channels," Adv. At. Mol. Opt. **53**, 413–441 (2006).

[91] L. Bergé, S. Skupin, R. Nuter, J. Kasparian, and J.-P. Wolf, "Ultrashort filaments of light in weakly ionized, optically transparent media," Rep. Progr. Phys. **70**, 1633–1713 (2007).

[92] V. P. Kandidov, S. A. Shlenov, and O. G. Kosareva, "Filamentation of high-power femtosecond laser radiation," Quantum Electron. **39**, 205–228 (2009).

[93] J. Liu, Z. Zhang, B. Shang, C. Chu, L. Sun, N. Zhang, L. Lin, and W. Liu, "Enhancement of multi-filament generation and filament-induced fluorescence by turbulence," Opt. Commun. **517**, 128290 (2022).

[94] A. L. Gaeta, "Catastrophic collapse of ultrashort pulses," Phys. Rev. Lett. **84**, 3582–3585 (2000).

[95] P. Wang, C. Wu, M. Lei, B. Dai, H. Yang, H. Jiang, and Q. Gong, "Population dynamics of molecular nitrogen initiated by intense femtosecond laser pulses," Phys. Rev. A **92**, 063412 (2015).

[96] Y. Liu, Y. Brelet, G. Point, A. Houard, and A. Mysyrowicz, "Self-seeded lasing in ionized air pumped by 800 nm femtosecond laser pulses," Opt. Express **21**, 22791 (2013).

[97] M. Britton, P. Laferriére, D. H. Ko, Z. Li, F. Kong, G. Brown, A. Naumov, C. Zhang, L. Arissian, and P. Corkum, "Testing the role of recollision in N_2^+ air lasing," Phys. Rev. Lett. **120**, 133208 (2018).

[98] M. Lei, C. Wu, A. Zhang, Q. Gong, and H. Jiang, "Population inversion in the rotational levels of the superradiant N_2^+ pumped by femtosecond laser pulses," Optics Express **25**, 4535 (2017).

[99] J. Yao, B. Zeng, H. Xu, G. Li, W. Chu, J. Ni, H. Zhang, S. L. Chin, Y. Cheng, and Z. Xu, "High-brightness switchable multiwavelength remote laser in air," Physical Review A **84**, 051802 (2011).

[100] A. Mysyrowicz, R. Danylo, A. Houard, V. Tikhonchuk, X. Zhang, Z. Fan, Q. Liang, S. Zhuang, L. Yuan, and Y. Liu, "Lasing without population inversion in N_2^+," APL Photonics **4** (2019).

[101] H. Li, M. Hou, H. Zang, Y. Fu, E. LÃ¶tstedt, T. Ando, A. Iwasaki, K. Yamanouchi, and H. Xu, "Significant enhancement of O_2 lasing by polarization-modulated ultrashort laser pulses," Phys. Rev. Lett. **122**, 013202 (2019).

[102] H. Xu, E. Lötstedt, A. Iwasaki, and K. Yamanouchi, "Sub-10-fs population inversion in N_2^+ in air lasing through multiple state coupling," Nature Communications **6** (2015).

[103] J. Ni, W. Chu, H. Zhang, B. Zeng, J. Yao, L. Qiao, G. Li, C. Jing, H. Xie, H. Xu, Y. Cheng, and Z. Xu, "Impulsive rotational raman scattering of N_2 by a remote air laser in femtosecond laser filament," Opt. Lett. **39**, 2250 (2014).

[104] H. Zhang, C. Jing, J. Yao, G. Li, B. Zeng, W. Chu, J. Ni, H. Xie, H. Xu, S. L. Chin, K. Yamanouchi, Y. Cheng, and Z. Xu, "Rotational coherence encoded in an air-laser spectrum of nitrogen molecular ions in an intense laser field," Phys. Rev. X **3**, 041009 (2013).

[105] X. Zhang, R. Danylo, Z. Fan, P. Ding, C. Kou, Q. Liang, A. Houard, V. Tikhonchuk, A. Mysyrowicz, and Y. Liu, "Backward lasing of singly ionized nitrogen ions pumped by femtosecond laser pulses," Appl. Phys. B **126** (2020).

[106] A. Dogariu, J. B. Michael, M. O. Scully, and R. B. Miles, "High-gain backward lasing in air," Science **331**, 442–445 (2011).

[107] D. Kartashov, S. Alisauskas, G. Andriukaitis, A. Pugzlys, M. Shneider, A. Zheltikov, S. L. Chin, and A. Baltuska, "Free-space nitrogen gas laser driven by a femtosecond filament," Phys. Rev. A **86**, 033831 (2012).

[108] P. Ding, S. Mitryukovskiy, A. Houard, E. Oliva, A. Couairon, A. Mysyrowicz, and Y. Liu, "Backward lasing of air plasma pumped by circularly polarized femtosecond pulses for the sake of remote sensing (black)," Opt. Express **22**, 29964 (2014).

[109] M. Ruchkina, P. Ding, A. Ehn, M. Alden, and J. Bood, "Single-shot, spatially-resolved stand-off detection of atomic hydrogen via backward lasing in flames," Proc. Combust. Inst. **37**, 1281–1288 (2019).

[110] P. Ding, M. Ruchkina, D. D. Cont-Bernard, A. Ehn, D. A. Lacoste, and J. Bood, "Detection of atomic oxygen in a plasma-assisted flame via a backward lasing technique," Opt. Lett. **44**, 5477 (2019).

[111] P. N. Malevich, D. Kartashov, Z. Pu, S. Alisauskas, A. Pugzlys, A. Baltuska, L. Giniunas, R. Danielius, A. A. Lanin, A. M. Zheltikov, M. Marangoni, and G. Cerullo, "Ultrafast-laser-induced backward stimulated raman scattering for tracing atmospheric gases," Opt. Express **20**, 18784 (2012).

[112] D. E. Spence, P. N. Kean, and W. Sibbett, "60-fsec pulse generation from a self-mode-locked Ti:sapphire laser," Opt. Lett. **16**, 42 (1991).

[113] M. T. Asaki, C.-P. Huang, D. Garvey, J. Zhou, H. C. Kapteyn, and M. M. Murnane, "Generation of 11-fs pulses from a self-mode-locked Ti:sapphire laser," Opt. Lett. **18**, 977 (1993).

[114] A. Y. Naumov, D. M. Villeneuve, and H. Niikura, "High conversion efficiency of an optical parametric amplifier pumped by 1 kHz Ti:sapphire laser pulses for tunable high-harmonic generation," Opt. Express **28**, 4088 (2020).

[115] D. K. Lauriola, P. S. Hsu, N. Jiang, M. N. Slipchenko, T. R. Meyer, and S. Roy, "Burst-mode 100 kHz N_2 ps-CARS flame thermometry with concurrent nonresonant background referencing," Opt. Lett. **46**, 5489 (2021).

[116] J. Felver, M. N. Slipchenko, E. L. Braun, T. R. Meyer, and S. Roy, "High-energy laser pulses for extended duration megahertz-rate flow diagnostics," Opt. Lett. **45**, 4583 (2020).

[117] S. Roy, W. D. Kulatilaka, D. R. Richardson, R. P. Lucht, and J. R. Gord, "Gas-phase single-shot thermometry at 1 kHz using fs-CARS spectroscopy," Opt. Lett. **34**, 3857 (2009).

[118] J. Kiefer, M. F. B. Stodt, and U. Fritsching, "Thermometry by vibrational raman spectroscopy of nitrogen: Identification and impact of spatial averaging effects," J. Raman Spectrosc. **52**, 1582–1588 (2021).

[119] V. G. Arakcheev, V. V. Kireev, V. B. Morozov, A. N. Olenin, V. G. Tunkin, A. A. Valeev, and D. V. Yakovlev, "Collisionally induced dephasing and rotational energy transfer in the CO_2 fermi dyad 'red' Q-branch 1285 cm^{-1}," J. Raman Spectrosc. **38**, 1038–1045 (2007).

[120] V. G. Arakcheev, V. V. Kireev, V. B. Morozov, A. N. Olenin, V. G. Tunkin, A. A. Valeev, and D. V. Yakovlev, "Collisionally induced dephasing and rotational energy transfer in the CO_2 fermi dyad 'blue' Q-branch 1388 cm^{-1}," J. Raman Spectrosc. **38**, 1046–1051 (2007).

[121] M. Kerstan, I. Makos, S. Nolte, A. Tünnermann, and R. Ackermann, "Two-beam femtosecond coherent anti-stokes raman scattering for thermometry on CO_2," Appl. Phys. Lett. **110**, 021116 (2017).

[122] M. Gu, A. Satija, and R. P. Lucht, "Effects of self-phase modulation (SPM) on femtosecond coherent anti-stokes raman scattering spectroscopy," Opt. Express **27**, 33954 (2019).

[123] D. Langevin, J. M. Brown, M. B. Gaarde, and A. Couairon, "Determination of molecular contributions to the nonlinear refractive index of air for mid-infrared femtosecond laser-pulse excitation," Phys. Rev. A **99**, 063418 (2019).

[124] J. K. Wahlstrand, Y.-H. Cheng, and H. M. Milchberg, "Absolute measurement of the transient optical nonlinearity in N_2, O_2, N_2O, and Ar," Phys. Rev. A **85**, 043820 (2012).

[125] S. A. Hosseini, Q. Luo, B. Ferland, W. Liu, S. L. Chin, O. G. Kosareva, N. A. Panov, N. Aközbek, and V. P. Kandidov, "Competition of multiple filaments during the propagation of intense femtosecond laser pulses," Phys. Rev. A **70**, 033802 (2004).

[126] L. Bergé, S. Skupin, F. Lederer, G. Méjean, J. Yu, J. Kasparian, E. Salmon, J. P. Wolf, M. Rodriguez, L. Wöste, R. Bourayou, and R. Sauerbrey, "Multiple filamentation of terawatt laser pulses in air," Phys. Rev. Lett. **92**, 225002 (2004).

[127] T. A. Labutin, V. N. Lednev, A. A. Ilyin, and A. M. Popov, "Femtosecond laser-induced breakdown spectroscopy," J. Anal. At. Spectrom. **31**, 90–118 (2016).

[128] A. A. Ilyin, S. S. Golik, K. A. Shmirko, A. Y. Mayor, D. Y. Proschenko, and Y. N. Kulchin, "Broadening and shift of emission lines in a plasma of filaments generated by a tightly focused femtosecond laser pulse in air," Quantum Electron. **48**, 149–156 (2018).

[129] Y. É. Geints, A. A. Zemlyanov, A. A. Ionin, S. I. Kudryashov, L. V. Seleznev, D. V. Sinitsyn, and E. S. Sunchugasheva, "Peculiarities of filamentation of sharply focused ultrashort laser pulses in air," J. Experiment. Theoret. Phys. **111**, 724–730 (2010).

[130] H. Zhang, Y. Zhang, S. Lin, Y. Zhang, A. Chen, Y. Jiang, S. Li, and M. Jin, "Influence of pressure on spectral broadening of femtosecond laser pulses in air," Phys. Plasmas **28**, 043302 (2021).

[131] Y. Ran, A. Boden, A. Richter, S. Guhl, S. Nolte, and R. Ackermann, "Nonresonant signal assisted high-pressure multi-species gas concentration measurements using ultrabroadband CARS," OSA Continuum **3**, 2036 (2020).

[132] F. Mazza, O. Thornquist, L. Castellanos, T. Butterworth, C. Richard, V. Boudon, and A. Bohlin, "The ro-vibrational v_2 mode spectrum of methane investigated by ultrabroadband coherent raman spectroscopy," J. Chem. Phys. **158** (2023).

[133] G. Point, Y. Liu, Y. Brelet, S. Mitryukovskiy, P. Ding, A. Houard, and A. Mysyrowicz, "Lasing of ambient air with microjoule pulse energy pumped by a multi-terawatt infrared femtosecond laser," Optics Letters **39**, 1725 (2014).

[134] T.-J. Wang, J.-F. Daigle, J. Ju, S. Yuan, R. Li, and S. L. Chin, "Forward lasing action at multiple wavelengths seeded by white light from a femtosecond laser filament in air," Phys. Rev. A **88**, 053429 (2013).

[135] C. Jing, H. Zhang, W. Chu, H. Xie, J. Ni, B. Zeng, G. Li, J. Yao, H. Xu, Y. Cheng, and Z. Xu, "Generation of an air laser at extended distances by femtosecond laser filamentation with telescope optics," Optics Express **22**, 3151 (2014).

[136] R. Ackermann, I. Makos, M. Kerstan, R. Kammel, S. Nolte, and A. Tünnermann, "Analysis of laser induced plasma in air using broadband femtosecond coherent anti-stokes raman scattering," Conference on Lasers and Electro-Optics, OSA Technical Digest (2016).

[137] R. B. Wright and C. H. Wang, "Density effect on the fermi resonance in gaseous CO_2 by raman scattering," J. Chem. Phys. **58**, 2893–2895 (1973).

[138] L. Shang, I. Chou, R. C. Burruss, R. Hu, and X. Bi, "Raman spectroscopic characterization of CH_4 density over a wide range of temperature and pressure," J Raman Spectrosc **45**, 696–702 (2014).

[139] G. Li, C. Jing, B. Zeng, H. Xie, J. Yao, W. Chu, J. Ni, H. Zhang, H. Xu, Y. Cheng, and Z. Xu, "Signature of superradiance from a nitrogen-gas plasma channel produced by strong-field ionization," Phys. Rev. A **89**, 033833 (2014).

[140] Y. Liu, P. Ding, A. Houard, and A. Mysyrowicz, *The Role of Electron Collisions in Lasing in Neutral and Singly Ionized Molecular Nitrogen* (Springer International Publishing, 2017).

[141] J. Kasparian, M. Rodriguez, G. Méjean, J. Yu, E. Salmon, H. Wille, R. Bourayou, S. Frey, Y.-B. André, A. Mysyrowicz, R. Sauerbrey, J.-P. Wolf, and L. Woöste, "White-light filaments for atmospheric analysis," Science **301**, 61–64 (2003).

[142] G. Méchain, G. Méjean, R. Ackermann, P. Rohwetter, Y.-B. André, J. Kasparian, B. Prade, K. Stelmaszczyk, J. Yu, E. Salmon, W. Winn, L. A. (Vern) Schlie, A. Mysyrowicz, R. Sauerbrey, L. Wöste, and J.-P. Wolf, "Propagation of fs TW laser filaments in adverse atmospheric conditions," Appl. Phys. B **80**, 785–789 (2005).

[143] Y. Ran, A. Boden, F. Küster, F. An, A. Richter, S. Guhl, S. Nolte, and R. Ackermann, "In situ investigation of carbon gasification using ultrabroadband coherent anti-Stokes Raman scattering," Appl. Phys. Lett. **119** (2021).

Zusammenfassung

Ziel dieser Arbeit war es, die Einsatzmöglichkeiten der CARS-Technik für Temperatur- und Konzentrationsmessungen in rauen Umgebungen (z. B. in der Verbrennungs- und Vergasungsdiagnostik) mit drei verschiedenen Konzepten zu untersuchen und zu erweitern: CARS auf der Grundlage eines zuverlässigen ps-Lasersystems mit OPA, CARS auf der Grundlage von ps-Filamentierung und Remote CARS auf der Grundlage von fs-filamentierung.

Im ersten Ansatz wurde ein kundenspezifischer ps-OPA (APE, Deutschland) aufgebaut und characterisiert, der mit einem kommerziellen 1-kHz Scheibenlasersystem gepumpt wurde. Dieser ps-OPA kann eine Pulsenergie von $\sim$ 200 μJ und eine Pulsdauer von $\sim$ 1 ps über den gesamten Abstimmbereich von 700 - 950 nm liefern. Mit dem Ausgang des OPA als Pumpe, den Laserpulsen bei 1030 nm als Stokes und der zweiten Harmonischen (515 nm) als Probe haben wir die CARS-Signale von N_2 und CO_2 bei hohen Temperaturen in einer Gaszelle untersucht. Der ps-CARS-Aufbau bietet eine ausreichende spektrale Auflösung (20 cm^{-1}), um die Grundschwingung und das erste heiße Band von N_2 zu unterscheiden. Zudem kann das polarisierende Interferenzmuster vermieden werden, das bei fs-CARS auftritt. Die Temperaturbestimmung gelang mit diesem System in guter Übereinstimmung mit Literaturwerten und Simulationen. Mit diesem CARS-Aufbau mit h–oher zeitlicher ($\sim$ 1 ps) und spektraler (20 cm^{-1}) Auflösung kann man ein höheres Signal-Rausch-Verhältnis erzielen und die Eigenschaften jedes Raman-Übergangs genau untersuchen. Diese Vorteile tragen zur Empfindlichkeit, Flexibilität und Effizienz des CARS-Experiments bei und machen es zu einem wertvollen Instrument für die Gasanalyse in rauen Umgebungen.

Im zweiten Ansatz haben wir systematisch die spektralen Eigenschaften untersucht, die durch ps-Filamentierung in Luft mit einer maximalen Pulsenergie von 60 mJ unter verschiedenen Fokussierungsbedingungen induziert werden. Mit einer spektralen Verbreiterung von 850 nm bis 1130 nm konnten Literaturwerte deutlich übertroffen werden. Die spektrale Spanne entspricht einer Raman-Verschiebung von 2900 cm^{-1}, was den Nachweis der CARS-Signale von N_2, O_2 und sogar CH_4 ermöglicht. Mit $\sim$ 1 ps filamentationsbasiertem CARS sind wir unseres Wissens nach die ersten, die gleichzeitig die CARS-Signale von N_2 und O_2 in Luft gemessen haben. Ein Nachteil sind die großen Schwankungen in den Filamentationsspektren, die zu einer durchschnittlichen Standardabweichung von 54 % für die Verhältnisse der Peaks von N_2 und O_2 führen. Durch Messung der Abhängigkeit des Verhältnisses als Funktion der Verzögerung konnten wir den Fehler jedoch auf 14 % reduzieren, was eine Konzentrationsbestimmung mit einer Genauigkeit von 7 % ermöglicht. Weitere Verbesserungen erfordern eine In-situ-Messung und Referenzierung der verbreiterten Filamentationsspektren.

Im dritten Ansatz konnten wir erstmals Remote-CARS auf der Grundlage von fs-Filamentierung mit einem einzelnen Strahl demonstrieren. Dabei wurde Laseremission 391 nm von N_2^+ in intensiven 800 nm fs-Filamenten beobachtet. Mit der Laseremission bei 391 nm, die als CARS Probestrahl dient, wurden die CARS-Signale von N_2, O_2, CO_2 und CH_4 beobachtet. Unsere Ergebnisse können für Fernerkundungsanwendungen genutzt werden, für die es wichtig ist, die Beugung sowohl für den Pump- als auch für den Probepuls zu überwinden.

Erklärung

Declaration of Academic Integrity

I hereby certify:

1. that I am familiar with the current Examination Regulations;
2. that this doctoral thesis is my own work and I have not copied any text passages from third parties or my own dissertations without referencing them accordingly and acknowledging any aids, personal correspondences and sources used in my work;
3. that I have not received any assistance from commercial agents offering dissertation services and that no third party has either directly or indirectly received any financial benefits for producing work in connection with this doctoral thesis;
4. that this doctoral thesis has not yet been submitted as part of a state examination or other scientific examination;
5. that a similar or in significant parts similar doctoral thesis has not been submitted to any other institution of higher education.

Jena, 24. July 2024 Xiaodong Zhao

List of publications and conference contributions

Publications in peer-reviewed journals

- X. Zhao, A. Boden, S. Nolte, and R. Ackermann, "Spectral properties of IR-filamentation in air induced by 1 ps pulses for coherent anti-Stokes Raman scattering", Opt. Continuum 2, 720-726 (2023)

- X. Zhao, M. Baudisch, M. Beutler, T. Gabler, S. Nolte, and R. Ackermann, "Tunable picosecond optical parametric amplifier pumped by 1 ps pulses at 1 μm for coherent anti-Stokes Raman scattering", Opt. Express 30, 33850-33859 (2022).

- X. Zhao, S. Nolte, and R. Ackermann, "Lasing of N_2^+ induced by filamentation in air as a probe for femtosecond coherent anti-Stokes Raman scattering", Opt. Lett. 45, 3661-3664 (2020).

Conference contributions

- X. Zhao, S. Nolte and R. Ackermann, "Spectral broadening in IR-filamentation induced by 1 ps pulses for Coherent Anti-Stokes Raman Scattering", 20th European Conference on Non-linear Optical Spectroscopy (ECONOS), Kiruna, Sweden (2022).

- X. Zhao, S. Nolte and R. Ackermann, "Thermometry by picosecond optical parametric amplifier for Coherent Anti-Stokes Raman Scattering", 20th European Conference on Non-linear Optical Spectroscopy (ECONOS), Kiruna, Sweden (2022).

- X. Zhao, A. Boden, S. Nolte, and R. Ackermann, "Spectral broadening of IR filamentation for coherent anti-Stokes Raman scattering", International Conference on Ultrafast Phenomena, Montreal Quebec, Canada (2022).

- X. Zhao, M. Baudisch, M. Beutler, T. Gabler, S. Nolte and R. Ackermann, "Picosecond optical parametric amplifier pumped by a thin-disk laser at 1 μm for Coherent anti-Stokes Raman scattering", 19th European Conference on Non-linear Optical Spectroscopy (ECONOS), Karlsruhe, Germany (2020/2021).

- X. Zhao, M. Baudisch, M. Beutler, T. Gabler, S. Nolte and R. Ackermann, "Tunable femtosecond optical parametric amplifier pumped by 1 kHz ultrafast thin-disk laser pulses for coherent anti-Stokes Raman scattering", Conference on Lasers and Electro-Optics/Europe, Munich, Germany (2021).

- X. Zhao, S. Nolte, and R. Ackermann, "N_2^+-lasing induced by filamentation in air for femtosecond coherent anti-Stokes Raman spectroscopy", CLEO: Conference on Lasers and Electro-Optics, San Jose, California, USA (2020).

- X. Zhao, S. Nolte, and R. Ackermann, "N_2^+-lasing induced by filamentation in air for femtosecond coherent anti-Stokes Raman scattering", 714. WE-Heraeus- Seminar, Physikzentrum Bad Honnef, Germany (2020).

Acknowledgment

Many people have supported me in different ways to the success of this work. I would like to express my deepest appreciation to those who supported and motivated me during the study of my PhD in Jena.

First of all, I am extremely grateful to my supervisor Prof. Stefan Nolte for offering the opportunity to work with him in the Ultrafast Optics Group and for his time of mentoring, valuable guidance and helpful suggestions I could always rely on. Thus, I am able to learn much more beyond this thesis. In addition, I would like to extend my sincere thanks to my supervisor Dr. Roland Ackermann for his consistent patience and valuable discussions and suggestions, which support my doctoral study. I also could not have undertaken this journey without my defense committee, who generously provide knowledge and expertise. Furthermore, this endeavor could would not have been possible without the project support (Optical in-situ investigation and modeling of high temperature conversion processes "OPTICON"), which is funded by Federal Ministry of Education and Research.

I am also thankful to my colleagues from our subgroup spectroscopy, Yang Ran, André Boden, Thomas Gabler, Marcus Junghanns und Timea Koch who supported me in my research and life. Thank you for all the advice and suggestions. Many thanks to the other colleagues in our Ultrafast Optics group, Alessandro Alberucci, Sebastian Beer, Markus Blothe, Maxime Chambonneau, Thorsten Goebel, Jisha Chandroth Pannian, Timothy Imogore, Ria Krämer, Kim Lammers, Qingfeng Li, Gobor Matthäus, Christian Matzdorf, Daniel Richter, Lisa Matthäus, Brian Seyfarth, Malte Siems, Tobias Ullsperger, Burak Yürekli. It is a pleasure to work with you!

Special thanks to Bodo Martin for taking care of the gas supply and management.

Here I would like to express my special thanks to my wife Yanyan Liu for supporting and understanding me all the time, for spending most of the time taking care of our lovely little girl Youyi Zhao and boy Roy Zhao. I am grateful to my parents Jushan Zhao and Xiru Gao, who support me making every big decision, going abroad and studying in Germany. I have so many thanks and gratitude that I do not know how to express. But one word is thank you for being with me all the way.